

Dissertation

submitted to the

Combined Faculties of the Natural Sciences and
Mathematics

of the

Ruperto-Carola-University of Heidelberg, Germany

for the degree of

Doctor of Natural Sciences

Put forward by

Moritz Simon Maria Kiehn

born in: Menden (Sauerland), Germany

Oral examination: 03.02.2016

Pixel Sensor Evaluation and Track Fitting for the Mu3e Experiment

Referees:

Prof. Dr. André Schöning

Prof. Dr. Stephanie Hansmann-Menzemer

ABSTRACT

Mu3e is a proposed new experiment that searches for the lepton flavour changing muon decay $\mu^+ \rightarrow e^+ e^- e^+$ with a projected sensitivity of 1 in 10^{16} decays. This decay is extremely suppressed in the Standard Model and an observation would be a clear sign of new physics. The muons are stopped on a target and decay electrons are measured in a magnetic spectrometer with a pixel detector. A low material budget and special algorithms are required to reconstruct the low momentum, strongly curved tracks with high precision at high rates.

In this work, I present the first systematic performance evaluation of the Mu3e high voltage monolithic active pixel sensor prototypes using test beam measurements at DESY. I showed that this novel technology allows sensor efficiencies above 99%.

In addition, I characterized a new track fit based on hit triplets. This fast fit is optimized to reconstruct multiple scattering dominated tracks and is suitable for Mu3e online tracking. For a precise offline reconstruction, I adapted the advanced general broken lines fit. It allows an increase in momentum resolution of up to 20% compared to the best fast algorithm.

The systematic pixel sensor and track fit evaluation with the corresponding software development is a cornerstone for Mu3e tracking.

ZUSAMMENFASSUNG

Das Mu3e Experiment ist ein neues Experiment zur Suche nach dem Lepton-Flavour-Quantenzahl verletzenden Myonenzerfall $\mu^+ \rightarrow e^+e^-e^+$ mit einer angestrebten Sensitivität von 1 in 10^{16} Zerfällen. Dieser Zerfall ist im Standardmodell so stark unterdrückt dass eine Beobachtung ein eindeutiger Hinweis für Physik jenseits des Standardmodells ist. Die Myonen werden durch ein Target gestoppt und die resultierenden Zerfallselektronen in einem magnetischen Spektrometer mit einem Pixeldetektor vermessen. Hierfür sind ein minimales Materialbudget and optimierte Algorithmen notwendig, um die niederenergetischen, stark gekrümmten Spuren mit hoher Rate zu rekonstruieren.

In dieser Arbeit wird die erste systematische Untersuchung eines mit Hochspannung betriebenen, monolithischen, aktiven Pixelsensor-Prototypen für das Mu3e Experiment beschrieben. In Teststrahlungsmessungen am DESY konnten Nachweiseffizienzen für Elektronen von besser als 99 % erreicht werden.

Außerdem wurde ein neuer Spurfit basierend auf Hit-Triplets charakterisiert. Dieser schnelle Algorithmus ist zur Rekonstruktion von Spuren mit dominierender Vielfachstreuung optimiert und für die Onlinerekonstruktion des Mu3e Experiments geeignet. Für eine präzise Offlinerekonstruktion wurde der General Broken Lines Algorithmus adaptiert. Er erlaubt eine Verbesserung der Impulsauflösung von bis zu 20 % im Vergleich zum besten schnellen Algorithmus.

Diese systematische Untersuchung der Pixelsensoren und Fit-algorithmen in Kombination mit der Entwicklung der zugehörigen Software ist eine der Grundlagen für die Mu3e Spurrekonstruktion.

TABLE OF CONTENTS

ABSTRACT	v
ZUSAMMENFASSUNG	vii
TABLE OF CONTENTS	ix
1 INTRODUCTION	1
2 LEPTON FLAVOUR VIOLATION	5
2.1 Lepton Flavour in the Standard Model	5
2.2 Beyond the Standard Model	6
3 THE MU3E EXPERIMENT	9
3.1 Signal & Backgrounds	9
3.2 Detector Concept	13
3.3 Tracking Requirements	17
I PIXEL SENSOR TESTBEAM MEASUREMENTS	
4 PIXEL SENSOR PROTOTYPES	25
4.1 Semiconductor Sensors	25
4.2 High-Voltage Monolithic Active Pixel Sensors	28
4.3 MuPix Prototypes	30
5 TESTBEAM SETUP AND ANALYSIS STRATEGY	35
5.1 Testbeam Setup	35
5.2 Analysis Procedure	39
5.3 Beam Telescope Performance	41
6 PROTOTYPE PERFORMANCE	45
6.1 The Strixel Feature	45
6.2 Clustering	47
6.3 Track Matching and Resolution	48
6.4 Efficiency	50
6.5 Summary	54
II TRACK FITTING WITH MULTIPLE SCATTERING	
7 TRACK MODELS AND UNCERTAINTIES	59
7.1 Analytic Helix Propagation	60
7.2 Track Parameters	61
7.3 Propagation of Uncertainties	63
7.4 Sources of Uncertainties	64
8 TRACK FITS	69

8.1	Method of Least Squares	69
8.2	Single Helix Fit	71
8.3	Single Triplet Fit	73
8.4	Triplets Fit	78
8.5	General Broken Lines Fit	80
8.6	Other Methods	83
8.7	Implementation	84
9	GENERAL COMPARISON	87
9.1	Simulation Setup	87
9.2	Reconstruction Setup	90
9.3	Triplets Fit	91
9.4	General Broken Lines Fit Reference Trajectory	94
9.5	Resolution	96
9.6	Bias and Pulls	98
9.7	Summary	101
10	PERFORMANCE FOR THE MU3E EXPERIMENT	103
10.1	Simulation Setup	103
10.2	Short Tracks	104
10.3	Long Tracks	108
10.4	Conclusions	116
11	SUMMARY, CONCLUSION, AND OUTLOOK	119
11.1	Pixel Sensor Prototypes	119
11.2	Track Fitting with Multiple Scattering	121
11.3	Conclusion	123
III APPENDIX		
A	ANALYTIC TRACK PROPAGATION	127
A.1	Equations of Motion	127
A.2	Helix Trajectory	128
A.3	Propagation	131
A.4	Solutions of the Propagation Equations	137
B	THE WATSON TRACKING LIBRARY	141
B.1	Motivation and Prior Art	141
B.2	Functionality	142
B.3	Additional Features	143
C	TRACK FITTING SUPPORTING FIGURES	145
	PUBLICATIONS	151
	REFERENCES	153
	DANKSAGUNG	163

INTRODUCTION

The Standard Model of particle physics describes all currently known elementary particles and their interactions. It has been very successful in describing many experimental observations, with the exception of neutrino flavour oscillations that were the subject of the 2015 Nobel price [89]. Although the Standard Model is theoretically self-consistent, it does not incorporate all fundamental interactions. It lacks e.g. a quantum theory of gravitation and fails to describe dark matter or dark energy. Consequently, the Standard Model cannot yet be the complete ‘theory of everything’.

The search for new physics beyond the standard model takes many different forms. Direct searches, as performed with the Large Hadron Collider, look for new particles or processes at previously unreachd high energy. Indirect measurements, on the other hand, pursue rare processes or perform measurements of known quantities with high statistics, usually at lower energies. Examples are precision measurements of the muon magnetic moment and its gyromagnetic ratio or (heavy) flavour spectroscopy at specialized storage rings.

Maybe we have already seen hints of new physics? Neutrinos are massless elementary particles in the original formulation of the Standard Model and lepton flavour is a conserved quantity. However, neutrino flavour oscillations were proposed early on [9, 10, 12], but not validated until in 1998 the disappearance of atmospheric muon neutrinos was discovered by the Super Kamiokande collaboration[24], followed by evidence for conversion of solar electron neutrinos by the Sudbury Neutrino Observatory in 2001/2002 [27]. These findings indicate that neutrinos have different non-zero masses and that the flavour eigenstates are superpositions of the mass eigenstates. Yet, the mechanism which generates neutrino mass is still unknown.

With neutrino mixing it is clear that lepton flavour violation occurs in interactions in the neutral lepton sector. In the quark sector, flavour mixing via the CKM matrix has been a long established mechanism [13, 14, 73]. This immediately poses the

question of flavour violation in the charged lepton sector [26, 66]. In principle, neutrino mixing enables lepton flavour violation in the charged lepton sector via loop diagrams. However, these processes are severely suppressed well below any experimentally accessible rates. This makes any measurable lepton flavour violating process in the charge lepton sector a clear sign for new physics.

Experimentally interesting for the search of charged lepton flavour violation are decays of muons, e.g. $\mu^+ \rightarrow e^+e^-e^+$, due to the availability of intense muon beams combined with a clear experimental signature. Previously, the SINDRUM experiment (1983-86) searched for said decay $\mu^+ \rightarrow e^+e^-e^+$ and found an upper limit on the branching ratio of 1×10^{-12} at 90% confidence limit [19]. Recently, advances in detector technologies have put into prospect even more precise measurements.

The Mu3e experiment is a proposed new experiment [61, 64] that searches for $\mu^+ \rightarrow e^+e^-e^+$ with a projected sensitivity of 1 in 10^{16} decays. A high intensity, low energy muon beam is stopped on a target where the muons decay at rest. The resulting decay electrons are measured by a particle tracker in a solenoid magnetic field with four layers of silicon pixel sensors. The tracker needs to have a minimal material budget while maintaining a continuous, high data readout. The key to achieve this goal are novel fast, thin silicon pixel sensors, so called high voltage monolithic active pixel sensors that are fabricated in commercial CMOS technology.

The major challenges for Mu3e are both hardware and software related. On the hardware side, it is vital to show that these novel silicon pixel sensors work with a high efficiency and provide the required resolution. With only four detector layers, there is very little redundancy for inefficiencies. In the first part of this work, results from test beam measurements with one of the first working small-scale prototype sensors are presented.

The high data output of the detector and the signature of the signal decay necessitate online reconstruction to filter events of interest. This requires fast algorithms to precisely reconstruct low momentum, high curvature tracks with few measurements points. In contrast to established reconstructions at high energies with low curvature tracks and a large number of measurements, e.g. at the Large Hadron Collider, the tracks are dom-

inated by multiple scattering. In the second part of this work, I will present a systematic study of several track fitting algorithms and their performance under different experimental conditions. This includes a novel track fit algorithm based on hit triplets for fast online reconstruction and an application of the general broken lines fit as an advanced track fit for a detailed offline reconstruction.

I will first briefly review the theoretical motivation for the search for charged lepton flavour and give an overview of the Mu3e experimental design. Then, I will introduce the sensor prototypes and discuss their performance in test beam measurements. The following part will explain the basic concepts of track fitting, present the track fitting algorithms, and evaluate their performance in a generic setup and specifically for the Mu3e experiment.

LEPTON FLAVOUR VIOLATION

The Standard Model of particle physics is a quantum field theory constructed by assuming a set of symmetries. Since symmetries and conservation laws are intimately connected [3], the symmetries of the system can be examined by investigating conserved and non-conserved quantities. In the past, interesting physics phenomena were found, where perceived symmetries are broken.

2.1 LEPTON FLAVOUR IN THE STANDARD MODEL

Leptons in the Standard Model carry an additional quantum number, the lepton flavour or lepton family number, which indicates the generation they belong to, i. e. electrons, muons, or taus. Particles carry a positive lepton number, e. g. electrons and electron neutrinos both carry an electron lepton number $l_e = 1$, and anti-particles carry a negative lepton number. Until the discovery of neutrino oscillation measurements, lepton flavour was assumed to be a conserved quantity in the Standard Model. Neutrino oscillation [24, 27, 77] changes neutrino types, e. g. $\nu_e \rightarrow \nu_{\mu'}$ and consequently violates the lepton flavour number.

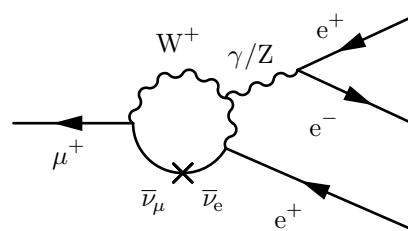


Figure 2.1: Feynman diagram for the lepton flavour violating decay $\mu^+ \rightarrow e^+e^-e^+$ via neutrino mixing.

Neutrino oscillation or mixing involves only neutral leptons. This opens an obvious question: does lepton flavour violation also occur in processes involving charged leptons? With neutrino mixing, charged lepton flavour changing processes can

occur via loop diagrams such as the one shown in Figure 2.1 for the $\mu^+ \rightarrow e^+ e^- e^+$ decay.

While theoretically allowed, the branching ratio for this decay is severely suppressed due to the large ratio of neutrino mass differences and W boson mass. The full branching ratio from [66] is proportional to

$$\text{BR}(\mu \rightarrow eee) \sim \left| \sum_{i=2,3} U_{\mu i}^* U_{ei} \frac{\Delta m_{i1}^2}{m_W^2} \right|^2 < 10^{-54}, \quad (2.1)$$

where the U_{ij} are the entries of the Pontecorvo-Maki-Nakagawa-Sakata neutrino mixing matrix [9, 10, 12], Δm_{ij} are the neutrino mass differences and m_W is the W mass. A branching ratio below 10^{-54} is unreachable by any experiment in the near future.

DECAY	BR LIMIT	EXPERIMENT
$\mu^+ \rightarrow e^+ \gamma$	5.7×10^{-13}	MEG [62]
$\mu^+ \rightarrow e^+ e^- e^+$	1×10^{-12}	SINDRUM [19]
$\mu^- + Au \rightarrow e^- + Au$	7×10^{-13}	SINDRUM II [34]

Table 2.1: Current experimental limits for the branching ratios (BR) of different lepton flavour changing muon decays.

While Figure 2.1 shows only the $\mu^+ \rightarrow e^+ e^- e^+$ decay, the same arguments apply to other charged lepton flavour violating processes, e. g. the $\mu^+ \rightarrow e^+ \gamma$ decay and $\mu^- + Au \rightarrow e^- + Au$ conversion. Both of which are suppressed in the Standard Model. The current experimental limits for the branching ratios of these lepton flavour violating processes are shown in Table 2.1.

2.2 BEYOND THE STANDARD MODEL

Since charged lepton flavour violating processes have an experimentally vanishing Standard Model expectation, they are very sensitive probes for new physics beyond the Standard Model. If any of these processes would be observed they must originate from additional contributions to the Standard Model diagrams discussed above.

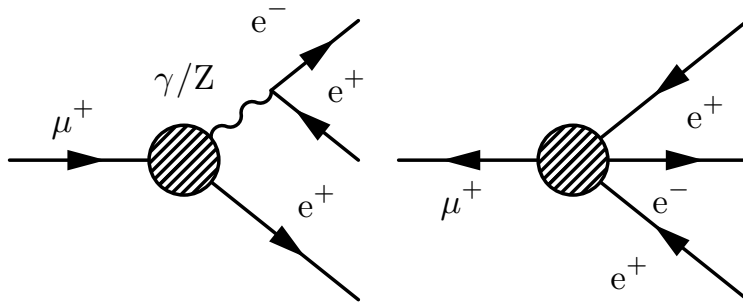


Figure 2.2: Generic Feynman diagrams for possible lepton flavour violating muon decays with new physics contributions. The left diagram is similar to Standard Model decay where new contributions occur inside the loop. The right diagram corresponds e. g. to new tree-level contributions.

In principle there are no restrictions on the possible type of new interactions. Two example generic diagrams for new physics contributions are shown in Figure 2.2. The left diagram is similar to the Standard Model loop diagram in Figure 2.1. Here, new physics would result in new particles running in the loop. The right diagram shows a four-fermion or contact interaction. This could be e. g. the result from new tree-level contributions with new heavy particles or from box diagrams. While both types of diagrams would contribute to the $\mu \rightarrow eee$ decay, only the left one will contribute to the $\mu \rightarrow e\gamma$ decay.

Instead of discussing specific new physics models, a model-independent comparison can be made by using an effective Lagrangian as discussed in [45, 66]. The simplified Lagrangian uses only two new physics parameters, an effective mass scale Λ and a scaling parameter κ that defines the relative contribution of different types of interactions. Small values of κ correspond to dipole-like interactions mediated by loop diagrams (Figure 2.2 left) and large values correspond to the contact interaction (Figure 2.2 right).

Using the effective Lagrangian the mass scale sensitivity with a given branching ratio sensitivity can be calculated for different muon decays. This is shown in Figure 2.3 where also the current branching ratio limits for the decays $\mu^+ \rightarrow e^+\gamma$ and $\mu^+ \rightarrow e^+e^-e^+$ are shown. The overall mass scale sensitivity can be as large as a few 10^3 TeV, significantly above the energy reach of current or future searches at the Large Hadron Collider.

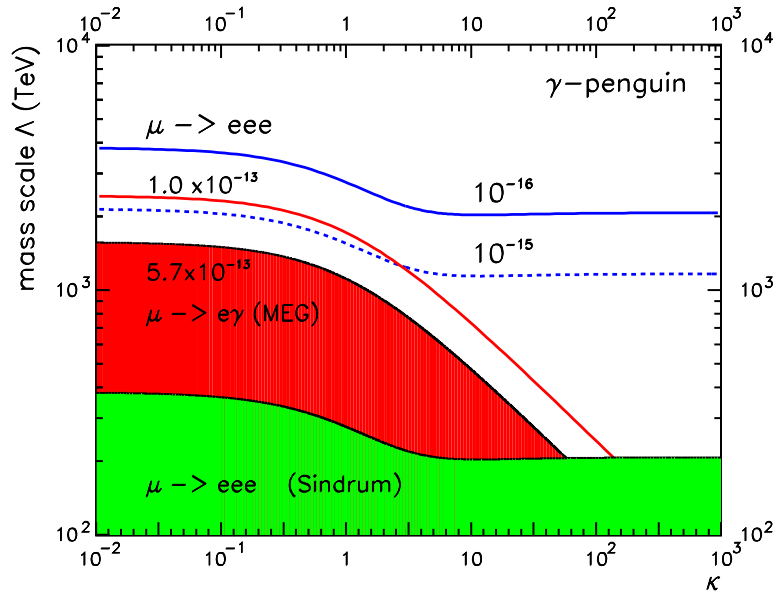


Figure 2.3: Effective mass scale Λ sensitivity for the decays $\mu \rightarrow eee$ and $\mu \rightarrow e\gamma$ for different decay branching ratios in a simplified effective field theory model. Shaded areas include the phase space that is already excluded by previous experiments. The κ parameter describes whether the interaction is of dipole type (small kappa) or a contact / four-fermion interaction (large kappa) [45, 64].

For small κ values the sensitivity of $\mu^+ \rightarrow e^+e^-e^+$ is suppressed by the additional photon vertex and the $\mu \rightarrow e\gamma$ decay can reach the same effective mass sensitivity with a three orders of magnitude lower branching ratio. For larger κ values the contact terms become important which contribute only to the $\mu \rightarrow eee$ decay.

To summarize: lepton flavour violating decays are an interesting indirect search for physics beyond the Standard Model. They are sensitive to effective mass scales in the 10^3 TeV range. Different decay modes allow complementary searches that could probe and possibly disentangle different types of new physics models. In addition to the Mu3e experiment, upgrades of the existing MEG experiment [63] and new conversion experiments [69, 71] are planned.

THE MU₃E EXPERIMENT

The Mu3e experiment is a novel experiment to be performed at the Paul-Scherrer Institute in Switzerland, searching for the lepton flavour violating decay $\mu^+ \rightarrow e^+ e^- e^+$. It aims for a sensitivity of better than 1 in 10^{16} decays, a four orders of magnitude improvement over the previous search by the SINDRUM experiment [19].

To achieve this high sensitivity, a new experimental design and new detector technology is required. The main component of the experiment is a magnetic spectrometer with a tracking detector based on innovative high voltage monolithic active pixel sensors. The necessary particles rates of $10^8 \mu^+/\text{s}$ to $10^9 \mu^+/\text{s}$ lead to raw data rates in excess of 1 Tbit s^{-1} [64]. Online reconstruction is required to filter events of interest and necessitates research of fast reconstruction algorithms.

In the following chapter I will discuss the experimental challenges and the resulting detector design choices with a focus on the tracking requirements. A detailed description of the experiment can also be found in the research proposal [64] and in the upcoming progress report [81].

3.1 SIGNAL & BACKGROUNDS

The signal decay $\mu^+ \rightarrow e^+ e^- e^+$ is identified by its three decay particles, two positrons and one electron, which I will collectively refer to as decay electrons from now on. They originate from the same decay vertex and have identical timing. As the sole resulting particles in this three-body decay, the sum of their four-momenta is identical to the muon mass¹

$$\left(\sum_{i=1}^3 P_{\mu,i} \right)^2 = m_{\mu}^2. \quad (3.1)$$

¹ In natural units
with $\hbar = c = 1$

In addition to the condition for the four-momenta, the total three-momentum of the decay electrons vanishes in the rest frame of the muon

$$\sum_{i=1}^3 \mathbf{p}_i = 0. \quad (3.2)$$

As will be discussed later, the muon rest frame is usually the lab frame of the detector and the condition of vanishing total momentum should be satisfied directly for the measured momenta. An example event topology can be seen in Figure 3.1.

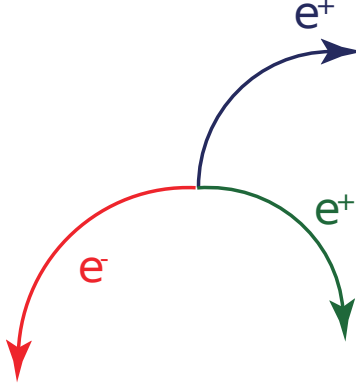


Figure 3.1: The event topology of the signal decay $\mu^+ \rightarrow e^+ e^- e^+$.

Because the signal decay is a three-body decay, the total momentum of each electron in the rest frame of the muon is limited by approximately half the muon mass, or more precisely

$$p_i^2 \leq \frac{m_\mu^2}{4} \left(1 - 10 \frac{m_e^2}{m_\mu^2} + \mathcal{O} \left(\frac{m_e^4}{m_\mu^4} \right) \right). \quad (3.3)$$

With a muon mass of about 105.66 MeV/c, the maximum momentum of a single decay electron is approximately 53 MeV/c. However, with three decay electrons at least one of them will have a much momentum significantly smaller than the maximum momentum. That means that the energy scale of the particles is extremely low compared to other particle physics experiments. This leads to strongly curved trajectories in a magnetic field and strong effects from multiple scattering. This will be discussed in detail in Chapter 7.

To identify a signal decay, the three electron tracks need to be reconstructed with the correct charges and with a high enough

precision to identify a common decay vertex and the correct four-momentum relation.

As discussed in Chapter 2, there are no irreducible physical backgrounds expected, i. e. decays with an identical final state, and all backgrounds originate from misidentification of other decay final states. In order to reach a given sensitivity for the signal decay, the possible backgrounds need to be suppressed below that level. In the following I want to shortly discuss the expected backgrounds.

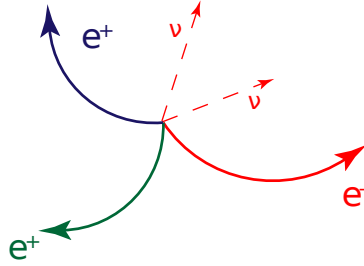


Figure 3.2: Topology of the internal conversion decay.

One prominent background is the internal conversion decay $\mu^+ \rightarrow e^+ e^- e^+ \bar{\nu}_\mu \nu_e$ as shown in Figure 3.2. It is similar to the signal decay but has two additional neutrinos in the final state to conserve lepton flavour. It is an allowed standard model process with a total branching ratio of $(3.4 \pm 0.4) \times 10^{-5}$ [73]. The neutrinos are not observable in the detector and carry away some of the momentum. The visible decay particles, i. e. two positrons and one electron, are identical to the signal decay described above. They originate from the same vertex at the same time. If the neutrinos carry very little momentum, the visible decay particles of this decay can look like the signal decay. However, the sum of four-momenta is not identical to the muon mass and the total sum of three-momenta in the muon rest frame does not vanish

$$\sum_{i=1}^3 \mathbf{p}_i \neq 0. \quad (3.4)$$

Whether the internal conversion decay is misidentified as a signal decay depends on the missing energy carried away by the neutrinos. Figure 3.3 shows the branching ratio of the internal conversion decay as a function of the visible center of mass energy. The three particle mass resolution determines the size of the signal window and the muon mass needed for a

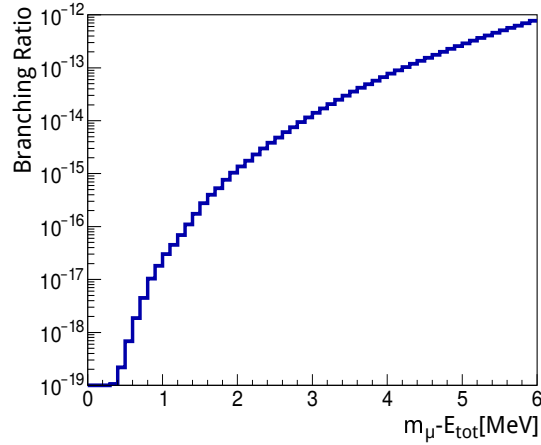


Figure 3.3: Branching ratio of the internal conversion decay as a function of the energy of the invisible neutrinos. E_{tot} is the energy of the visible decay electrons. Courtesy of Ann-Kathrin Peerevoort based on on a matrix element calculation by A. Signer and company. Original plot from [46].

reasonable efficiency and thus the amount of internal conversion background in the signal region. From Figure 3.3 it is clear that a mass resolution of better than $0.5 \text{ MeV}/c$ is required to suppress the internal conversion background below the target sensitivity.

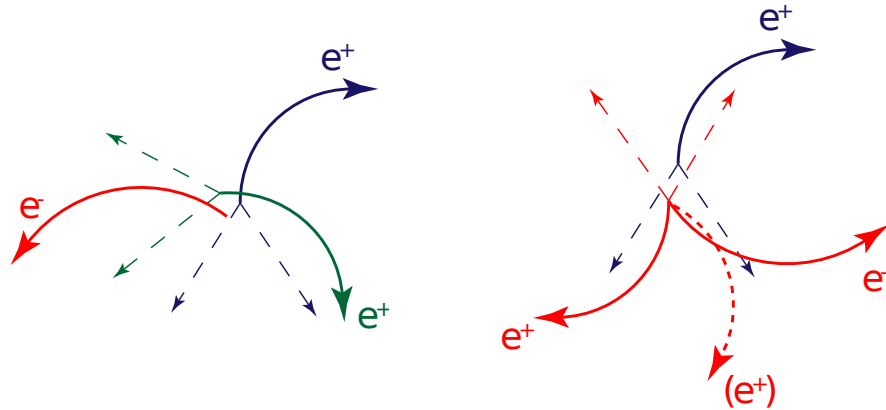


Figure 3.4: Topology of possible combinatorial background. The left diagram shows a random combination of two Michel decays and an independent electron. The right diagram shows a random combination where a positron is misidentified as an electron.

Another background source are accidental combinations of independent decays. The dominating muon decay mode is the Michel decay, i. e. $\mu^+ \rightarrow e^+ \nu_e \bar{\nu}_\mu$, where the only visible decay

particle is a positron. Additional electrons are easily created from interactions with material. Bhabha scattering in the target material is the largest source of electrons and can be minimized by reducing the target material. Due to the detector setup that will be discussed in later parts of this chapter, decay positrons can curl back in the magnetic field. The recurling incoming positron trajectory could then be misidentified as an outgoing electron.

As both electrons and positrons are readily available, accidental background originates from random coincidences in space, time, and momentum of three particles as shown in Figure 3.4. This could be a combination of two decay positrons from two independent regular Michel decays and an additional electron from other sources (Figure 3.4 left side) or from cases with misidentified electrons (Figure 3.4 right side). Whether such a random combination is identified as a signal decay depends again on the experimental resolution. A high momentum, vertex, and time resolution directly reduces the possible background rate. In addition, the accidental background rate also depends on the initial muon rate and the initial density of decay vertices. The temporal vertex density is minimized with a continuous muon beam. However, due to these dependencies, strict requirements for the resolution are not as easily derived as for the case of the internal conversion background.

The very small probability of these random coincidences has to be compared to the large number of muon decays.¹ Although this accidental overlap has a very small probability, the large number of observed muon decays means that even a very small coincidence rate of $10^{-16} / \mu^+$ leads to an observable background rate.

¹ At least $10^{16} \mu^+$.

For a successful search, we need to be able to reconstruct low momentum electron tracks with a very high precision. The combined mass resolution of the signal events needs to be below 0.5 MeV/c with an additional excellent vertex resolution to separate possible decay vertices. Ideally, the time resolution must be high enough to be able to separate all individual decays.

3.2 DETECTOR CONCEPT

The concept of the Mu3e experiment is shown in Figure 3.5. Incoming muons are stopped on an extended target where they

decay at rest. The decay electrons propagate in a homogeneous magnetic field and both the outgoing and returning part of the helical trajectory are measured by a tracking detector based on silicon pixel sensors. Additional timing measurements are provided by scintillating fibres and tiles. Signal decays are selected by reconstructing all tracks and searching for combinations consistent with the conditions described above. The initial phase I of the experiment will use an existing muon beam line at the Paul Scherrer Institute. To reach the full sensitivity an upgraded beam line with higher intensity and a possible extension of the detector geometry is needed.

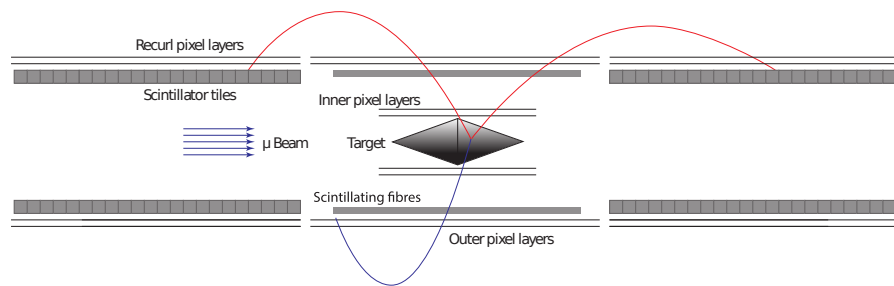


Figure 3.5: Overview of the Mu3e phase I experiment along the beam direction. The central detector contains the extended target, two inner and two outer cylindrical layers of pixel sensors, and the scintillating fibre detector. Upstream and downstream of the central detector are additional so-called recurl stations. Each contains two cylindrical layers of pixel sensors and thick scintillating tiles for additional timing measurements.

The outer layers of each of the three tracking stations have a length of 36 cm, while the inner layers of the central detector have a length of 12 cm. The lengths are designed to allow a large solid angle coverage of the decay electrons. The detector layers have a prism shape with average radii of the layers at 22 mm, 28 mm, 70 mm and 78 mm as shown in Figure 3.6.

3.2.1 Muon Beam

To reach the target sensitivity of 1 in 10^{16} decays much more than 10^{16} muons need to be stopped and their decay particles

reconstructed. As discussed in Section 3.1, a continuous beam is advantageous to suppress accidental background. Acceptance cuts and reconstruction inefficiencies will of course increase the required number of initial muons — or decrease the sensitivity for a fixed number of observed muons. With three years of data taking at a beam duty rate of 30%, i. e. approximately 10^7 s of integrated beam time per year, this would require a muon rate in excess of 10^9 s^{-1} .

The Paul-Scherrer Institute hosts the world most intense continuous proton beam [55]. High intensity muons beams are created as tertiary beams via pion decays. The primary proton beam hits a rotating carbon target and creates pions via various hadronic processes. The pions decay dominantly into muons [73] that are then extracted into a separate muon beam line and transported to the experiment [37]. Different kinematic regimes of the decay pions can be selected by the scattering angles of the pions, i. e. their angles with respect to the primary beam, and the transport properties of the beam line. By using large scattering angles, muons can be selected that originate from pion decays at rest. Their momentum is limited to the mass difference between pions and muons. They are often called surface muons since they originate from pion decays at rest on the surface of the primary target. Muons from pion decays in the bulk are stopped in the the target material or scattered away and do not reach the extraction beam line. The resulting low-energy, mono-energetic, continuous muon beam is ideally suited for the Muze experiment.

Existing beam lines at the Paul-Scherrer Institute can routinely provide beam rates of $10^8 \mu^+ / \text{s}$. The $\pi E5$ beam line provides a continuous surface anti-muon beam of with a mean momentum of 28 MeV/c and a momentum bite of 5% and is hosting the MEG experiment [62]. Due to the low energy, the anti-muons can be easily stopped and have not enough energy to participate in background inducing hadronic interactions.

With the existing rates a sensitivity on the order of 1 in 10^{15} can be achieved in a reasonable time. There are ongoing efforts to optimize existing beam lines for maximum beam intensities. Additional developments for upgraded targets and possible future beam lines are also underway [76].

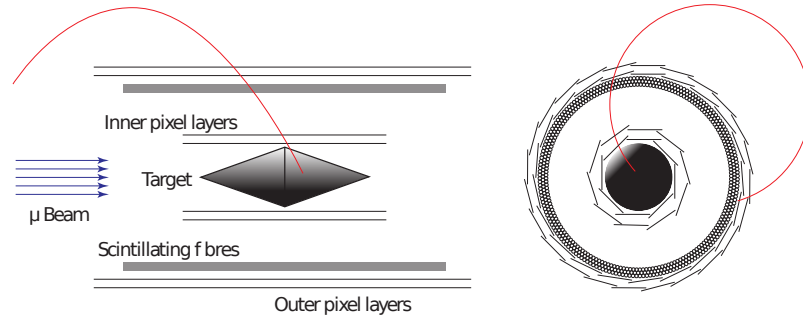


Figure 3.6: Overview of the central part of the Mu3e experiment with the muon stopping target, the inner and outer pixel detector, and the fibre timing detector. On the left is the view along the beam direction and on the right is the view transverse to the beam direction.

3.2.2 Target

The target has to fulfill two separate requirements: it must have enough material to stop all muons and it should have as little material as possible to reduce Bhabha scattering and to minimize the influence from material interactions on the particle trajectories. In addition, the muon decay vertices should be uniformly distributed over a wide area to suppress possible accidental background combination.

A hollow double cone target constructed from MylarTM foil, a geometry similar to the target shape in the SINDRUM experiment [19], is used to satisfy these requirements and can be seen in the center of Figure 3.5 and Figure 3.6. When viewed along the beam direction, the target appears as a circular block with a radius of 19 mm. The radius is matched to the expected beam size at the target position. The total target length is 100 mm in order to spread possible decay vertices over a wider range.

Along the beam direction effective material thickness for the muons is increased by the incidence angle of the beam on the inclined target surface, whereas decay particles moving transverse to the beam see very little material. A thickness of 75 μm for the upstream cone and 85 μm for the downstream cone in combination with an additional degrader upstream of the target is sufficient to provide a uniform stopping distribution of the incoming low energy muons.

3.2.3 Timing Detectors

With an expected muon rate of up to $10^9 \mu^+ / \text{s}$, a time resolution better than 1 ns is necessary to be able to separate individual decay electrons. The expected time resolution of the silicon pixel sensors is of the order of a few ns, i. e. a single readout frame as seen by the tracking detector contains an overlay of around 20 individual decaying myons. Additional timing detectors are needed to be able to distinguish independent decay electrons and to verify coincident particles from possible signal decays.

Timing measurements are provided by the scintillating fibres in the central detector and thick scintillating tiles in the recurl stations. The fibre detector in the central part of the detector consists of multiple layers of fibres in a cylindrical geometry close to the third layer of the tracking detector. To reduce the effects from multiple scattering on the propagating track, only three layers of fibres with $250 \mu\text{m}$ thickness each are used in the baseline design. This limits the signal amplitude and the time resolution to approximately 1 ns.

The scintillating tiles are positioned underneath the inner layer of the recurl stations. Since a particle reaches the tile detector only after it has passed all tracking layers, thick scintillating tiles with a size of $6.5 \text{ mm} \times 6.0 \text{ mm} \times 5.0 \text{ mm}$ can be used to stop the particles. The generated signal amplitude is much larger and results in a time resolution of better than 100 ps [78].

3.3 TRACKING REQUIREMENTS

The tracking detector and the subsequent track reconstruction algorithms needs to be able to efficiently reconstruct low momentum electron tracks at a very high rate, while maintaining a minimal material budget and optimizing the resolution to a precision much better than 1 MeV/c.

Due to the low momentum of the decay particles, multiple scattering effects are the dominating contributions to the reconstruction uncertainties. The multiple scattering effects are proportional to $\sqrt{x/X_0}/p$, where p is the absolute momentum and x/X_0 is the material thickness in units of the radiation length X_0 [73]. It will be discussed in more detail in Section 7.4.2. The electron momentum is fixed to a range of 10 MeV/c to 53 MeV/c. As discussed in Section 3.1 the upper momentum

bound is given by the muon decay kinematics while the lower bound is given by the detector geometry. To optimize the reconstruction uncertainties, the material budget, i. e. x/X_0 , has to be minimized.

The low momentum also leads to strongly curved trajectories in the magnetic field. With a 1 T magnetic field, the radius of a helical trajectory of a 50 MeV/c electron is 16.7 cm. This requires a small detector with the radii of the cylindrical layers smaller than the lowest reconstructable track. A weaker magnetic field would relax these size criteria. However, it would call for a larger, more expensive magnet to contain the trajectories. At some point, also scattering along the free propagation would become significant. The chosen 1 T field is a compromise between the competing constrains.

For existing experiments, e. g. ATLAS and CMS at CERN, highly curved trajectories are usually considered background. Due to these distinct features different detector geometries and reconstruction algorithms are necessary for Mu3e.

3.3.1 *Pixel Tracker*

The tracking detector is build from four cylindrical layers of thin silicon pixel sensors supported by a Kapton[®] framework. They are arranged in two sets of double layers. Since fitting a helix requires at least three measurement points, four measurements corresponding to four layers are the minimal number of layers with additional redundancy.

The inner double layer, also called the vertex detector, is located as close to the target as possible. Its inner radius is determined by the size of the muon beam to achieve the highest possible vertex resolution. The average radii are 22 mm and 28 mm.

The size of the outer two layers determines the acceptance and the momentum resolution for outgoing tracks. Low momentum tracks that are too strongly curved to reach the outer layers can not be reliably reconstructed. Small outer radii mean better acceptance but shorter propagation distance for the tracks. Since the momentum resolution depends on the propagation distance this would also result in lower momentum resolution. However, the Mu3e experiment does not require additional particle identification or calorimetric detectors. Par-

ticles can propagate freely and recur back to the tracker where they can be measured again. This increases the propagated distance significantly and determines the momentum resolution. The chosen average outer radii are 70 mm and 78 mm which limits the minimal momentum for transverse tracks to approximately 15 MeV/c.

The arrangement as doublet layers is favored for reconstructing multiple scattering dominated tracks. The large gap between the doublet layers increases the precision of the momentum determination. The arrangement is also favored from a pattern recognition point of view. By using the information in a doublet layer to construct short track stubs the combinatorial burden on the track finding procedure can be reduced.

Each tracker layer is constructed from high voltage monolithic active pixel sensors (HV-MAPS). These are a novel type of silicon pixel sensors that feature a monolithic design, i. e. the sensor and the necessary analog and digital readout electronics are integrated into the same sensor chip. They allow fast digital readout, a high geometric coverage and a small pixel size of 80 μm [41, 57, 67]. In addition, they can be thinned down to less than 50 μm without compromising their performance. The silicon sensor and the Kapton[®] support structure add up to a very low combined material budget of less than 0.1 % radiation length per layer. A detailed discussion of the general pixel sensor design and prototype performance can be found in Part i.

There are other existing technologies that could fulfill some of the tracking requirements. Gaseous detectors, such as wire chambers or time projection chambers, offer a low material budget but do not have the rate capabilities required for the Mu3e experiment or cannot deliver high precision due to space charge effects [65]. Existing hybrid silicon sensors are another proven technology that is at the core of most current collider experiments. They regularly provide the required resolution and rate capabilities, but do not fit in the Mu3e material budget. Existing monolithic active pixel sensors are too slow for the high data rates.

3.3.2 *Magnet*

The momentum of the decay particles is measured via the curvature of their trajectories in a solenoid magnetic field where

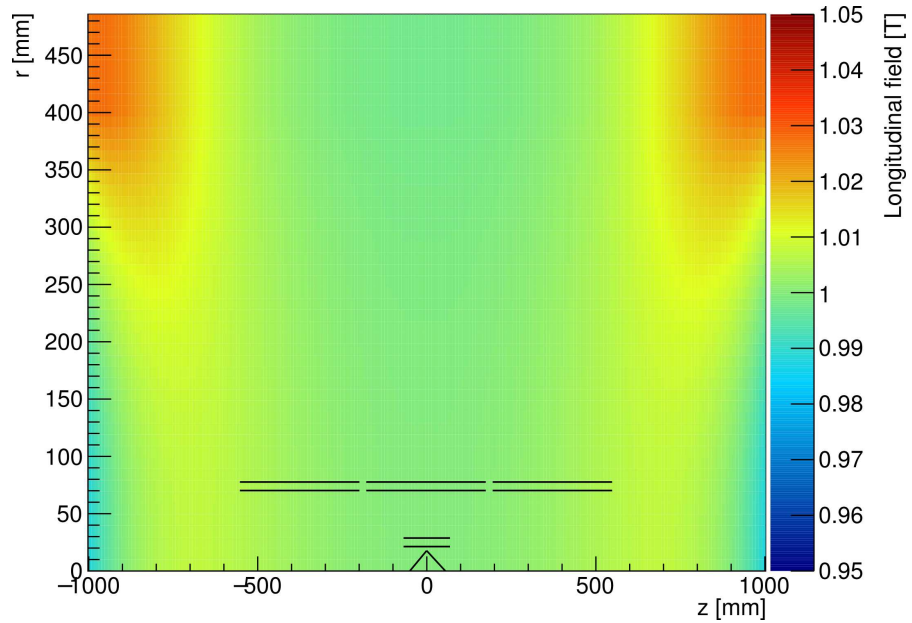


Figure 3.7: Magnetic field along the field axis as a function of the z position and the radial distance to the field axis. The field map was calculated for the expected solenoid field with compensation coils. The black lines in the bottom part of the histogram mark the position of the target and the inner and outer pixel layers. Courtesy of Niklaus Berger.

the field direction is aligned with the direction of the muon beam. The field in the center of a solenoid coil is reasonably well approximated by a constant magnetic field but will show inhomogeneities towards the coil edges. Additional compensation coils are used for the Mu3e experiment so that the magnetic field for the Mu3e experiment is well approximated by a homogeneous field over the largest possible area. This can be seen in Figure 3.7 where the expected axial field for the Mu3e experiment is shown. The homogeneity enables fast analytic track propagation methods that are discussed in detail in Part ii.

3.3.3 *Online Reconstruction*

The signal decay for the Mu3e experiment has a complex signature that involves multiple electron trajectories, vertex, and timing constraints. This allows strong background suppression, but poses a challenge for the readout and trigger systems. The separation of signal and possible backgrounds requires a full

reconstruction of each readout frame in order to use reconstructed trajectories and possible vertex positions to match multiple electrons to a possible signal decay.

However, the expected readout data rate at a muon rate of $10^9 \mu^+ / \text{s}$ is on the order of 1 Tbit s^{-1} . Since no simple trigger system can identify possible signal decays, online reconstruction is needed. The continuous data stream from the detector is read out via a network of FPGA-based readout boards and transferred to a GPU-based computer farm. Each readout frame is reconstructed online and only potentially interesting readout frames are stored for further analysis.

This requires suitable reconstruction algorithms for fast online reconstruction as well as for the refined offline analysis to achieve maximal resolution. I will give a systematic comparison of multiple algorithms in Part ii.

Part I

PIXEL SENSOR TESTBEAM MEASUREMENTS

PIXEL SENSOR PROTOTYPES

The tracking detector for the Mu3e experiment needs to measure the hit position of decay electrons with a reasonable single hit resolution. While doing so it has to maintain high rate capabilities and have a very low material budget. This requires the use of a novel type of silicon pixel sensors, so called high voltage active pixel sensors as discussed in Section 3.3.1.

Here, I want to shortly introduce the general working principles of silicon sensors and the particular properties of high-voltage monolithic active pixels sensors. I will then introduce the specific prototype chips developed for the Mu3e experiment.

4.1 SEMICONDUCTOR SENSORS

Semiconductors materials, especially silicon, are the basis of all modern electronic equipment. They are crystalline materials defined by a low charge carrier density and a low conductivity. By selectively introducing impurities, the electronic band structure and the conductivity can be tuned. This process is called doping and introduces new charge carriers — electrons in the conduction band and missing electrons or holes in the valence band — into the material. Depending on the dopant, the material is called a p-type material when holes are the majority charge carriers or an n-type material when the electrons are the majority charge carriers. The construction of semiconductor devices with complex doping profiles based on lithographic processes, e. g. computer chips, is a widely established and commercially available method, e. g. [40].

Semiconductor sensors are exploiting the properties of so-called pn-junctions, boundaries between differently doped regions in a semiconductor. One region has a p-type doping, while the other region is of n-type doping. At the boundary, the charge carriers diffuse into the opposite doped region where they are in minority and recombine to create a region without free charge carriers — the depletion zone.

Without an external voltage the thickness of the depletion zone is determined by the voltage built up due to diffusion of charge carriers and the densities of the donor η_D and acceptor atoms η_A . The so called diffusion voltage U_D in turn depends on the relative charge carrier densities. By applying an external voltage in reverse bias configuration the respective charge carriers can be forced further away from the boundary and the depletion zone can be increased. The thickness of the depletion zone depends on the applied voltage V as

$$d = \sqrt{\frac{2\epsilon}{q} \frac{\eta_A + \eta_D}{\eta_A \eta_D} \cdot (U_D - V)}, \quad (4.1)$$

with the permittivity ϵ and the magnitude of the electron charge q . A full derivation can be found in all solid state textbooks [40].

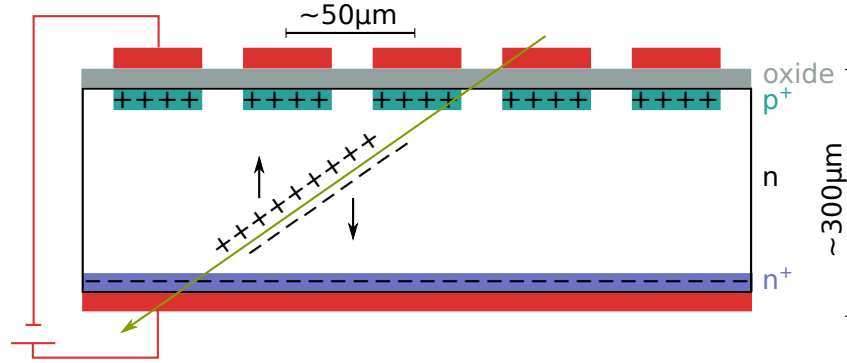


Figure 4.1: Working principle of a planar semiconductor particle sensor with typical structure sizes.

A typical configuration for a planar silicon pixel sensor is shown in Figure 4.1. In principle, a pn-junction is created by appropriately doping the two sides of a silicon crystal. Then, a sufficiently high voltage is applied in a reverse-bias configuration, to fully deplete the sensor, i. e. the depletion zone extends over the whole sensor and no free charge carriers exist in the bulk of the sensor material. For thick sensors, very high voltages have to be applied and the material has to be chosen appropriately to achieve full depletion. Usually, a more sophisticated doping scheme is chosen. Charged particles that traverse a detector will interact with the material and deposit energy. The energy depositions are mostly due to ionization of the detector material, but depend on the particle type and its energy

[73]. Along the particle path, ionization charges are generated that drift in the electric field towards the two sides. The drifted charges induce voltages in localized electrodes on one side of the detector.

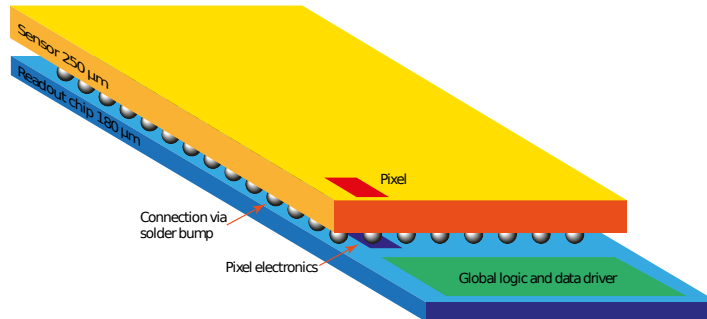


Figure 4.2: Structure of a hybrid semiconductor pixel sensor with separate sensor and readout chip. Courtesy of Niklaus Berger.

For a full sensor configuration, usually a separate chip is used to process the generated signals from the actual sensors. This configuration is called a hybrid (pixel) sensor and is depicted in Figure 4.2. In the hybrid setup, the actual sensor material and the required processing logic are separated. This allows the usage of different materials, e.g. a specialized semiconductor substrate for the sensor and a regular silicon-based process to construct the readout electronics.

Hybrid sensors are a well established technology and are currently used e.g. in the vertex semiconductor detectors of the ATLAS and CMS experiments at the Large Hadron Collider. With a typical sensor thickness of $200\ \mu\text{m}$ to $300\ \mu\text{m}$, bias voltages of up to $1\ \text{kV}$ are required to fully deplete the sensor [25]. The large active zone generates a large signal that allows for a high efficiency and small electrodes allow precise single hit resolution.

However, the separation between the sensor and the readout electronics requires bump-bonding to combine sensor and readout chip into a single package. This is a complicated procedure that contributes significantly to the overall costs of the sensor. The bump bonds usually contain heavy material, such as indium, and the total material budget of a sensor module is significantly above 1% radiation length [25]. This renders the hybrid detector technology unsuitable due to the material

budget requirements of the Mu3e experiment as discussed in Chapter 3 and Part ii.

4.2 HIGH-VOLTAGE MONOLITHIC ACTIVE PIXEL SENSORS

High voltage monolithic active pixel sensors (HV-MAPS) are novel semiconductor sensors for particle physics experiments developed by Ivan Perić [41, 67]. They combine the sensor and the necessary readout electronics on a single chip based on a commercial silicon complementary metal–oxide–semiconductor (CMOS) process. Commercial CMOS production processes are readily available, since they are used to build most analog and digital application specific integrated circuits (ASIC) and allow the creation of complex structures with multiple metal layers and varying doping profiles at relatively low cost. The specific process that is used to make HV-MAPS was driven by high voltage switching applications in the automotive industry. Due to their production process, HV-MAPS sensors are also called HV-CMOS sensors.

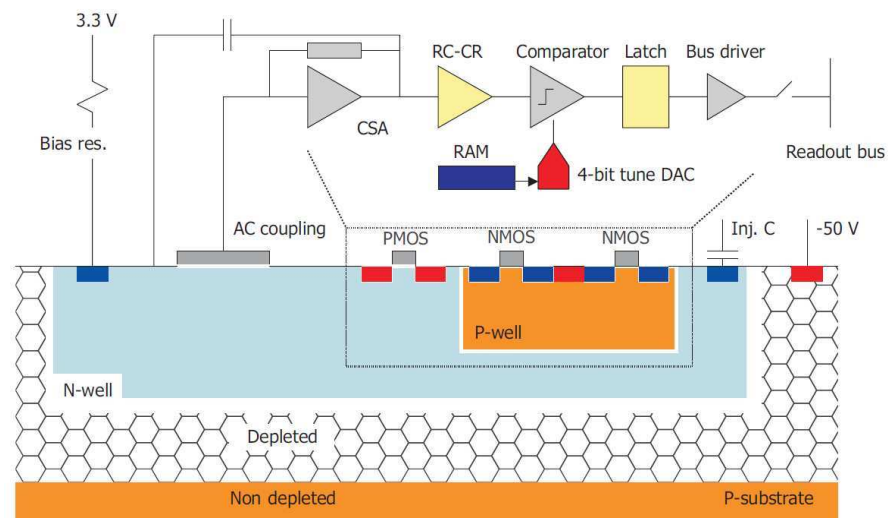


Figure 4.3: Schematic layout of a single pixel in a HV-MAPS sensor. From [41].

For the HV-MAPS sensor, the sensitive diode structure is defined by a deep n-doped well and the p-doped substrate of the chip. The deep n-well is created using the CMOS process and defines the size of a single pixel. By applying a bias voltage between the substrate and the n-well, as shown in Figure 4.3,

a depletion zone is created around and beneath the n-well that forms the sensitive area of the chip. The maximal voltage depends on the specific production process and is around 100 V. Although this bias voltage is smaller than the bias voltages of hybrid sensors, it is still referred to as high voltage in this context.

Since the bias voltage is applied between between the n-well and the substrate, the n-well can be used to house additional circuits. This can include both analog and digital electronics, e.g. charge-sensitive amplifiers to increase the signal generated by the traversing particle. With structure sizes of 180 nm routinely available and pixel cell sizes of the order of 50 μm to 100 μm , there is enough space even for extensive per-pixel electronics.

Compared to the hybrid designs with planar sensors, a HV-MAPS sensor has a much thinner active area. For the chosen silicon technology with bias voltages in the 50 V to 90 V range, the typical thickness of the depletion zone is around 15 μm [57, 67]. This results in less generated charge and a smaller signal. Since only the thin depletion depletion layer is needed for signal generation, the remaining substrate below can be removed to create a chip with minimal material. However, the smaller signal is compensated by the direct amplification of the in-pixel charge-sensitive amplifier. There is no signal degradation or additional noise due to bonding connections or a long path to the amplifier. The thin active area in combination with the bias voltage allows for fast charge collection via drift of the order of 40 ps [41, 57]. As a result, the practical time resolution is not determined by the charge collection, but by the time scales introduced by the signal shaping in the amplifier and the additionally introduced electronics.

Using a commercial CMOS processes has additional benefits. No bump bonding procedure is needed, which significantly reduces the material budget, simplifies the chip handling, and decreases the overall costs of the sensor. With the CMOS process additional digital logic, e.g. zero suppression, can be added to the chip to remove the need for additional readout chips.

The HV-MAPS detector technology is crucial to the design of the Muze experiment. It enables us to build a tracking detector that delivers the required resolution and particle rate capabilities while maintaining the low material budget that is key for low momentum particle tracking. However, since many of its

benefits, e. g. low cost, integrated readout, and small material budget, are not specific to the Mu3e experiment, it can be of interests to other experiments. Examples would be detector upgrades for a high intensity Large Hadron Collider or for detectors at future colliders [79].

4.3 MUPIX PROTOTYPES

The MuPix sensor prototypes are implementations of the HV-MAPS design described in Section 4.2. They are designed specifically for the Mu3e experiment. Different prototypes have been developed with different pixel sizes, overall geometry and functionality and are listed in Table 4.1.

The MuPix2 prototype was an initial proof-of-concept design that used a binary shift-register based readout system with very little additional logic on the chip. The MuPix3 sensor was the first prototype that included part of the digital readout logic on the sensor chip and increased the pixel size to $92\ \mu\text{m} \times 80\ \mu\text{m}$ closer to the specification values. Unfortunately, a design issue prohibited the usage of the digital readout components and allowed only tests of the analog behaviour. These problems were fixed with the MuPix4 sensor. This is the first working prototype that combines both analog and digital readout electronics on a single sensor. The MuPix4 prototype will be the main focus in this thesis.

NAME	PIXEL SIZE	MATRIX SIZE
MuPix2	$39\ \mu\text{m} \times 30\ \mu\text{m}$	36×42
MuPix3	$92\ \mu\text{m} \times 80\ \mu\text{m}$	32×40
MuPix4	$92\ \mu\text{m} \times 80\ \mu\text{m}$	32×40
MuPix6	$103\ \mu\text{m} \times 80\ \mu\text{m}$	32×40
MuPix7	$103\ \mu\text{m} \times 80\ \mu\text{m}$	32×40

Table 4.1: Pixel and matrix size for different MuPix HV-MAPS prototypes. A MuPix5 sensor does not exist.

The MuPix4 sensor has some minor issues that will be discussed in detail in Chapter 6. The MuPix6 chip introduced a second amplifier stage and fixed some problems in the digital logic. For the MuPix7 prototype, a fast serial readout link was incorporated. Both MuPix6 and MuPix7 were not yet available

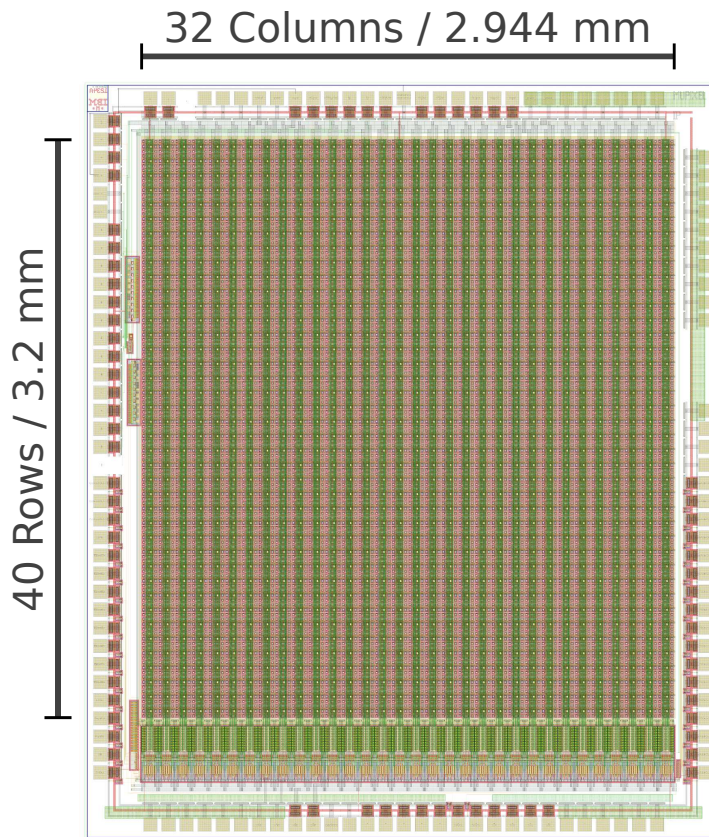


Figure 4.4: MuPix4 prototype schematic. The upper part shows the pixel matrix with the charge-sensitive per-pixel amplifiers. The lower green bar contains the digital readout logic. For each pixel in the upper matrix, a corresponding cell with the comparator and associated digital logic exists in the lower part.

for the work presented in this thesis. All prototypes feature binary hits using a single global threshold and additional per-pixel tuning, but they differ in pixel size, diode shape, and the level of integration of additional digital readout circuits on the chip.

Figure 4.4 shows the schematic of the MuPix4 prototype. The major part of the chip is occupied by the active pixel matrix in the upper part. With 32×40 pixels the total area is $2.944 \text{ mm} \times 3.2 \text{ mm}$ or 9.43 mm^2 . This is still a small scale prototype compared to the design specifications of $2 \text{ cm} \times 2 \text{ cm}$ for the final chip.

Each pixel contains the deep n-well, the signal electrodes, and the charge sensitive amplifier and signal shaper. The pixel is directly connected to a corresponding digital cell located in the smaller block on the bottom of the chip. Each digital cell

contains a comparator that checks if the signal is above the global threshold and memory blocks that store a hit flag and a time stamp. This configuration and the resulting signal shapes are shown in Figure 4.5. In addition to the global threshold, a per-pixel digital-to-analog converter (tune DAC) allows a fine tuning of the threshold for each pixel, by introducing small variations around the global threshold for the local comparator. In addition, the behaviour of the analog circuits, e. g. sensitivity of the charge-sensitive amplifier or the signal shape, can be tuned using a set of global parameters.

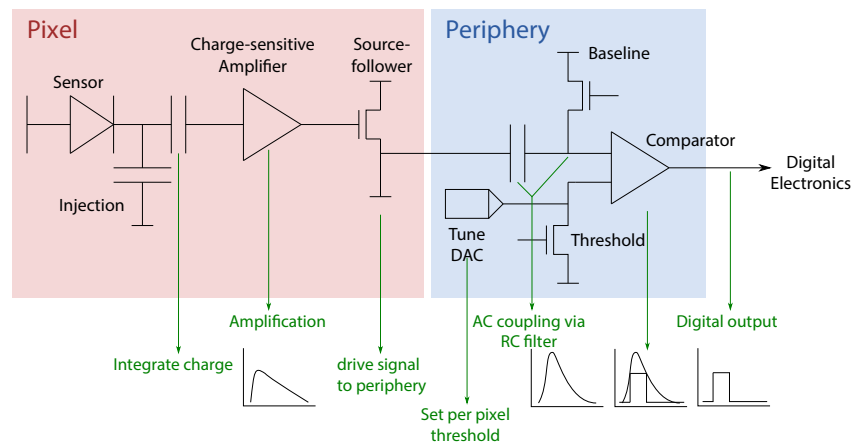


Figure 4.5: Schematic view of the analog and digital per-pixel circuits. The left part is located in the pixel itself while the right part resides in the corresponding digital cell in the bottom periphery. From [60].

The MuPix4 sensor uses a trigger-less or data-driven readout scheme, i. e. each pixel runs independently from other pixels and without a global trigger signal. An eight bit time stamp is distributed to all readout cells. For the MuPix4 prototype, the time stamp signal is externally generated with a frequency of up to 100 MHz. As soon as a signal above the configured threshold is detected, the pixel logic stores the current timestamp in a memory cell and activates a hit flag. The hit flag is stored until the pixel is read out, i. e. a second hit is not registered until the first one is read out.

The simplified data flow for the readout of the pixel is visualized in Figure 4.6. All hit flag signals along a single digital column are connected and read out by a per-column circuit. A digital column comprises the even or odd numbered pixels in

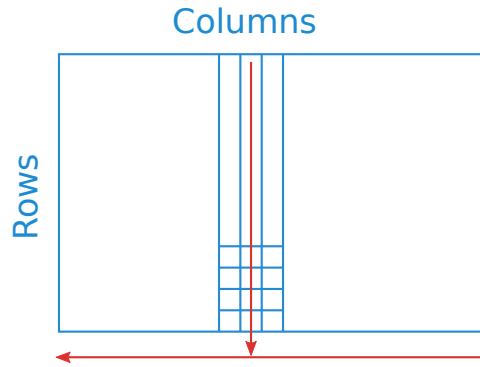


Figure 4.6: Data flow for the MuPix4 readout. Hits are read out along a column using a priority encoding scheme. Additional logic transfers the data to the readout FPGA.

one physical column, i. e. a physical column corresponds to two digital readout columns with separate column logic circuitry. This column logic detects whether any pixel in the column has a registered hit and then reads out the row position and stored time stamp of each hit starting from the bottom rows. The readout is priority encoded, i. e. a hit in a lower row is always read out before a hit in an upper row regardless of the time stamp. The final output is a continuous stream of hits — not necessarily ordered in time, where each hit is defined by a digital hit position and the time stamp.

The per-pixel logic and the digital logic for reading out the columns is implemented on the prototype chip. For both laboratory tests and for the test beam measurements, the prototype sensor is mounted on a custom PCB readout board. The state machine that drives the readout is implemented on an external FPGA that is directly connected to the PCB board (compare Figure 5.2). The FPGA sets the necessary signals, including the time stamp, to read out the hits over a parallel interface. This allows a detailed control of the readout logic and is crucial during the development phase.

The readout board and the FPGA state machine was originally designed by Ivan Perić and modified by the group at the Physikalisches Institut. The FPGA is connected via USB to a readout computer, where a custom software is used to store and process the received data. All measurements presented in this work are performed using the aforementioned setup. Starting from MuPix4, a new readout system is used. To allow high

data rates, a new FPGA board is directly connected to the PCI express bus of a computer. I designed and wrote the necessary drivers and laid the ground work for the read out software of future setups [72].

For the final chip, the full readout logic currently implemented on the external FPGA will be implemented on the chip itself. The latest prototype version MuPix7 already contains an implementation of the fully integrated read out logic that was extensively tested on the external FPGA in the test beam setups presented in this work. It also implements a fast serial link to be able to transmit data rates at 1.25 Gbit s^{-1} [81], significantly faster than the parallel setup used for these tests.

The different sensor prototypes have been extensively tested in laboratory setups using radioactive sources, lasers, and injection pulses to simulate the signals normally generated by a traversing particle [58, 60, 68].

Testing the performance of sensor prototypes is essential for detector development. It allows identification of deficiencies and possible improvements early on in the development process, a requirement for the successful construction of the final sensor chip for the any experiment.

Laboratory tests, i. e. by measuring the sensor response to radioactive sources, laser or LED pulses, and manual injection of electric signals into the sensor electronics, can provide initial checks and have been previously performed for the MuPix prototypes [58, 60, 68]. However, the artificially generated signals differ from the signals generated by traversing particles, e. g. laser pulses induce charges only on the surface and injection pulses need to be calibrated to the actual particle energy deposition. Performance tests using well defined particle beams are therefore crucial, both to test the sensor in a realistic setup and to calibrate the laboratory measurements.

Performance measurements with particles requires certain knowledge about the particles, especially the impact point on the sensor for position resolved measurements. This information is provided by a so-called beam telescope, a particle tracker based on silicon pixel sensors, that needs to be integrated with the MuPix4 device-under-test.

In the following chapter, I will discuss the setup and data analysis for test beam measurements performed at the facilities of the German Electron Synchrotron (DESY) laboratory. The measurements use an EUDET beam telescope to provide a track-based performance analysis. I will focus on measurements with the MuPix4 prototype performed during the February 2014 campaign at DESY.

5.1 TESTBEAM SETUP

The performance of the previously described sensor prototypes were tested during multiple test beam campaigns at beam facilities at the European Nuclear Research Center (CERN), at

the Paul-Scherrer-Institute (PSI), and at the German Electron Synchrotron (DESY) laboratory. A list of test beam campaigns where I contributed both to the setup, operations, and analysis efforts are listed in Table 5.1 with the tested sensor prototypes and the beam properties. The initial tests with the MuPix2 prototype were performed at CERN and DESY to show the general viability of the technology. The test beam measurements with the MuPix3 prototype were unsuccessful due to production problems of the digital readout. They were finally superseded by the test with the MuPix4 sensor, the first prototype chip with a working integrated digital readout.

DATE	FACILITY	SENSOR	BEAM
October 2012	CERN	MuPix2	180 GeV π
March 2013	DESY	MuPix2	1 GeV–6 GeV e^\pm
June 2013	DESY	MuPix3	1 GeV–6 GeV e^\pm
October 2013	DESY	MuPix4	1 GeV–6 GeV e^\pm
February 2014	DESY	MuPix4	1 GeV–6 GeV e^\pm

Table 5.1: List of testbeam campaigns.

All measurements discussed in this chapter were performed at the T22 beamline at DESY. The beam facility provides electron or positron beams with a maximum energy of 6 GeV. Bremsstrahlung photons are generated by placing a thin carbon rod in the beam halo of the DESY II synchrotron. DESY II stores electrons at an energy of 6 GeV and the energy of the photons is therefore limited to this energy. The photons are transported out of the synchrotron beam pipe to a target where they are converted to electron-positron pairs. The electrons and positrons pass an additional dipole magnet and a collimator. By setting different magnet currents the particle type and its energy can be selected [39].

The maximum particle rates are around 5 kHz, but depend on the conversion target and the selected energy. The rates are maximal at energies around 3 GeV. To reduce contributions to the telescope resolution from multiple scattering, a beam energy of 5 GeV was selected. The resulting rates were usually well below 1 kHz.

The full test beam setup with the beam telescope, the MuPix4 prototype, trigger scintillators, and the particle beam is shown

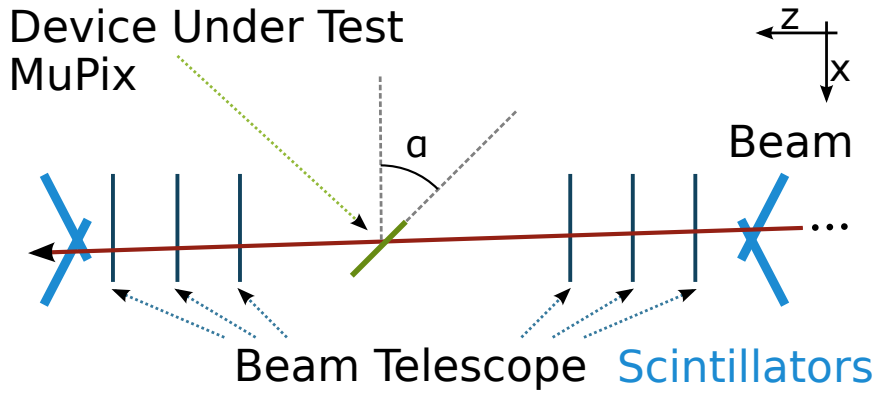


Figure 5.1: Beam telescope setup at the DESY testbeam facilities. The red arrow indicates an example trajectory that traverses the beam telescope, the four trigger scintillators, and the device under test.

in Figure 5.1. The MuPix4 sensor is placed inside the beam telescope, with three telescope sensors upstream and downstream. The MuPix4 sensor is mounted on a rotary stage to allow different beam incidence angles.

The beam telescope used is the ACONITE telescope. It is one of the telescopes developed by the EUDET collaboration, a European collaboration for high energy physics detector development [52], and is provided by the testbeam team at DESY as a user facility. The EUDET type telescopes are constructed from six planes of MIMOSA26 pixel sensors [36, 43, 44, 49]. These are $10.6 \text{ mm} \times 21.2 \text{ mm}$ monolithic active pixel sensors with a $18.5 \mu\text{m}$ pixel pitch and a rolling shutter readout.

The telescope planes are spaced to optimize the position resolution for the reconstructed tracks. Shorter distances to the device-under-test reduce the extrapolation error from the last telescope plane. However, the smallest possible distance in this setup is limited by the additional space required to allow rotations. This can be seen in Figure 5.2, where the full MuPix4 assembly barely fits into the available space for a rotation of 45° .

The readout of the EUDET telescope uses the EUDAQ data acquisition framework [85]. EUDAQ is a distributed system that uses a common trigger signal to synchronize multiple components, e.g. telescope sensors and the device-under-test. A trigger logic unit generates a global trigger signal using the co-

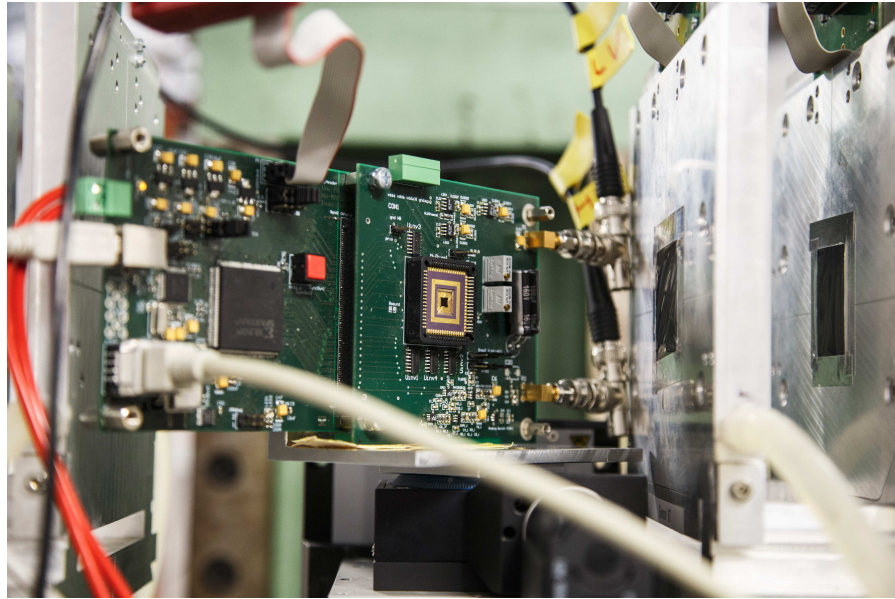


Figure 5.2: Photo of the telescope setup at DESY. The MuPix4 prototype on its readout board is seen in the middle in a rotated configuration. The FPGA board is directly connected to the MuPix4 readout board and can be seen on the left with its connection to the controlling computer. The aluminum housing of the telescope sensors can be seen at both edges; two downstream planes on the right side, one upstream plane on the left side. The electron beam enters from the right. Photo courtesy of Niklaus Berger.

incidence of four small finger scintillators, two before and two after the telescope assembly. The trigger logic unit is also responsible to communicate a unique trigger number to all hardware components for easy synchronization. It ensures that no additional trigger signals are generated while any participating device is still busy.

All devices process the readout data separately on different computers. The data is then sent over a network connection to a central data collector to assemble a combined data stream. My responsibility was the integration and adaption of the existing MuPix readout systems into the EUDAQ system to take advantage of all the available tools. This included the conversion between competing data formats, synchronization among multiple systems (EUDAQ, MuPix FPGA), and data transfers over the network.

This simplifies subsequent analysis, since all data resides in a single stream with a common timing identifier. No addi-

tional synchronization is needed and many possible errors, e. g. dropped events due to buffer constraints, are recoverable.

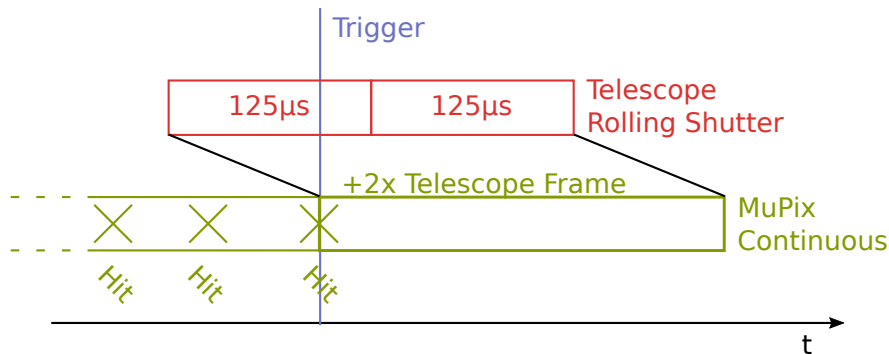


Figure 5.3: EUDAQ trigger scheme and readout timing.

The triggered data acquisition system in combination with the slow rolling-shutter-based readout of the telescope sensors poses a complication for the MuPix integration. MIMOSA26 sensors read out the pixel matrix line by line, which takes approximately 125 µs for the full pixel matrix. With a given trigger signal, the DAQ system does not know whether the corresponding hit is located above or below the current line. To ensure that no hit goes missing, the full pixel matrix is read out twice as indicated in Figure 5.3.

For the MuPix₄ prototype, the triggered readout has to be emulated. The sensor is continuously read out and hits are accumulated in an internal buffer as soon as a previous readout cycle has finished. When the MuPix DAQ system receives the trigger signal, it has to accumulate hits for the duration of two MIMOSA26 cycles. The accumulated hits are then combined into one event for the EUDAQ system.

5.2 ANALYSIS PROCEDURE

The raw data, i. e. the recorded hits on the telescope planes and the MuPix₄ prototype, requires additional processing steps to perform the prototype performance analysis. The hits are measured in the local pixel coordinates and need to be transformed to space points using the telescope geometry. Hits from the separate planes must be matched to tracks, the corresponding best-fit trajectories must be reconstructed, and the estimated intersections with the device-under-test must be calculated. These

analysis steps are performed using the EUTelescope analysis software [54, 86]. EUTelescope is a comprehensive pixel telescope analysis framework that was developed as the analysis package for the EUDET type telescopes. It is based on the software framework of the International Linear Collider Collaboration [88].

Since the EUTelescope packages allows its application to a variety of setups, extensive configuration and optimization are required for a successful test beam analysis. In the following, I will explain all the necessary steps that I performed to enable the final performance analysis of the prototype sensor.

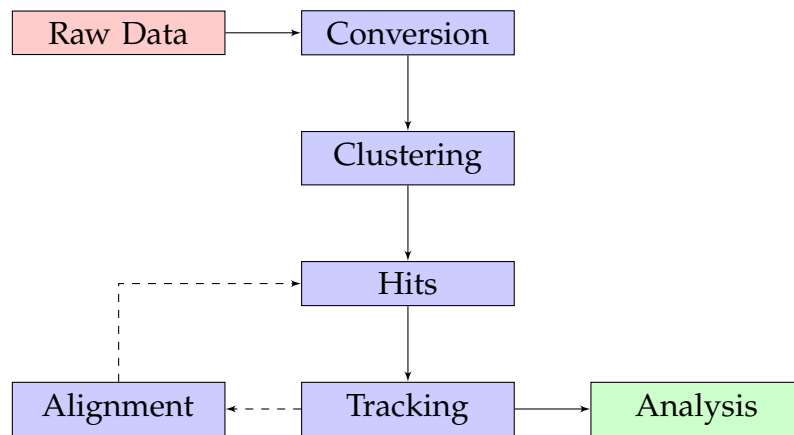


Figure 5.4: Data flow in the EUTelescope analysis framework.

The multi-step analysis procedure defined by EUTelescope is outlined in Figure 5.4. The raw data is first converted to a common file format. To simplify the analysis at later stages, noisy pixels are removed already at this point. Noisy pixels are defined as pixels with a high average hit rate, above 0.1%/event for the telescope sensors and above 1%/event for the MuPix4 prototype. In the next step, hits are formed on the local planes by merging adjacent hit pixels into clusters. Local hits on each measurement plane are defined by the center-of-mass position of the amplitude weighted pixel hits of each cluster. Local hits are then transformed into the global coordinate system using the telescope geometry.

Particle tracking assumes a linear track along the nominal beam axis. Track candidates are constructed by projecting the hits onto a common plane and combining hits within a fixed radius of $750\ \mu\text{m}$. Only candidates with exactly six hits, one on each telescope plane, are fitted using a linear track model.

Tracks are further selected by requiring a maximum χ^2 value and a maximum slope of 0.1, i. e. tracks must be well-fitted and be consistent with the beam direction.

First, the telescope without the device-under-test is aligned using special runs where the device-under-test is physically removed from the beam position. The initial geometry information is gathered by manual position measurements. Then, a manual rough alignment follows using hit correlations between the different planes. This allows an alignment precision on the order of 50 μm . The alignment is then further optimized by an automated track-based alignment procedure. The automatic alignment procedure is based on the general broken lines track fit [35, 59] and the Millepede alignment program [28, 54]. An application of the general broken lines fit as an advanced track fit for the Mu3e experiment will be discussed in Chapter 8.

Next, the device-under-test is aligned with respect to the telescope. Due to the much smaller size of the MuPix4 compared to the Mimosas26 sensors, it is difficult to locate its position relative to the telescope. By plotting the telescope hits for events with registered hits in the MuPix4 sensor, the sensitive area of the MuPix4 is visible as a shadow in the hit maps of the telescope layers. This allows a direct determination of the MuPix4 position relative to the telescope sensors. After the initial alignment, the same procedures discussed above are used to achieve full alignment. The only difference is that now tracks with seven hits, six hits on the telescope and one hit on the device-under-test, are used.

The final results from the EU Telescope processing are the extrapolated positions of the reconstructed telescope tracks on the nominal plane of the MuPix4 device-under-test. For the performance analysis, the extrapolated positions and the unprocessed raw MuPix data is processed using custom software that I have designed and implemented.

5.3 BEAM TELESCOPE PERFORMANCE

The operating parameters of the telescope sensors are provided by the DESY testbeam group and were used without further optimization. The data taking is organized into runs, where each runs is defined by a fixed amount of accumulated data. Alignment is performed for sets of runs with identical position-

ing. An overview of the different sets of runs can be found in Table 5.2. Here, I will shortly discuss the performance of the telescope reconstruction described above. The results of the performance analysis for the MuPix4 prototype are discussed in the next chapter.

FIRST RUN	ROTATION	V_{BIAS}	CONTENT
6054			Alignment run
6070	0°	50 V	Threshold scan
6082	0°	70 V	Threshold scan
6094			Alignment run
6108	45.0°	50 V	Rotated threshold scan
6112	45.0°	70 V	Rotated threshold scan
6118	22.5°	50 V	Rotated threshold scan
6122	22.5°	70 V	Rotated threshold scan

Table 5.2: List of analyzed datasets from the February 2014 testbeam campaign presented in this thesis. The datasets are identified by their first run. The rotation angle α and the bias voltage V_{bias} are the settings of the MuPix4 device-under-test if present.

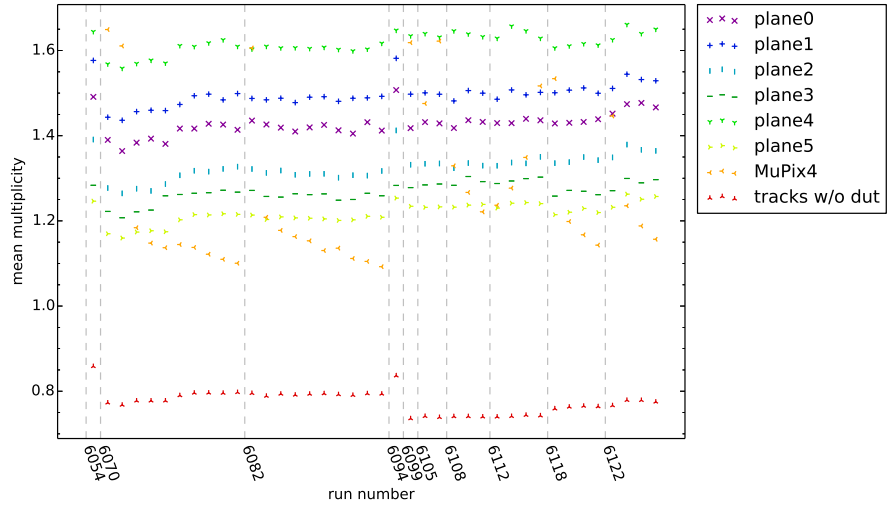


Figure 5.5: Mean number of clusters and reconstructed tracks per event for the telescope planes and the MuPix prototype for different runs. The run number are not continuous and the dashed lines mark changes in the configurations, e. g. a change of the MuPix bias voltage or the beam incidence angle.

The event rates for all analyzed runs are shown in Figure 5.5. The hit rate of the telescope planes and the MuPix4 prototype

is the mean number of clusters per event after removal of noisy pixels. The track rate, on the other hand, is the mean number of reconstructed tracks using only the telescope hit information.

The hit rate for each telescope plane stays relatively constant over the whole testbeam campaign. There are differences between the telescope planes on the order of 15 % that are not correlated to plane positions along the beam. This suggests different single hit efficiencies and noise rates rather than beam dispersion effects as the source. The track rate is significantly lower than the hit rate, suggesting a low tracking efficiency. However, its exact value cannot be reliably estimated from the rates alone without knowledge of the telescope plane efficiencies.

The telescope and MuPix hit rates are of comparable size. A naive expectation would be that they have a ratio comparable to their relative sensitive areas, i. e. $9.4 \text{ mm}^2 / 224 \text{ mm}^2 = 0.042$. This ignores possible effects from non-uniform particle distributions and the different integration times for the telescope plane and the MuPix sensor discussed above. The similar rates are most likely a result of the much larger integration time of the MuPix4 sensor due to the different readout architecture discussed previously.

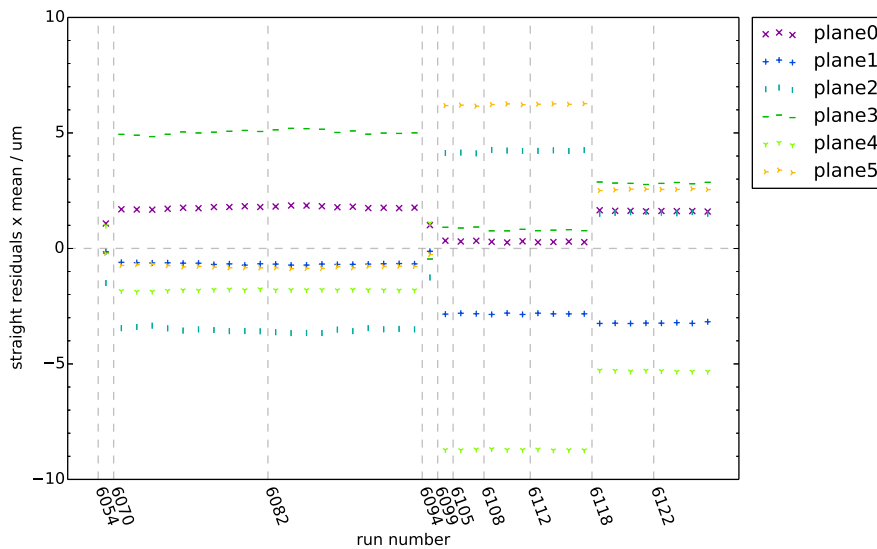


Figure 5.6: Residual distribution mean for reconstructed tracks on all planes of the beam telescope for different runs. The run number are not continuous and the dashed lines mark changes in the configurations.

The telescope alignment can be checked by looking at the residual distributions of the tracks, i. e. the distances between the fitted and measured track positions on each telescope plane. Deviations of the distribution mean from zero indicate possible misalignment and are shown in Figure 5.6 for the track residuals along the global x-direction for all telescope planes.

The deviations are on the order of $5\ \mu\text{m}$ to $10\ \mu\text{m}$. Due to technical limitations with the EU Telescope software, the alignment could not be further improved using the automated alignment procedure. Since the misalignment is still small compared to the MuPix4 pixel sizes and the track rate is low, this is not a problem for the analysis. This invariance and the effective resolution of the extrapolated track position on the device-under-test will be discussed in the next chapter.

Overall, the telescope setup could reliably reconstruct the particle tracks and allowed the subsequent analysis of the MuPix4 prototype performance.

PROTOTYPE PERFORMANCE

The performance of the MuPix4 prototype with respect to its single hit resolution, clustering properties, and efficiency is analyzed using the telescope setup. After discussing the properties of the pixel sensor data, the matching between telescope tracks and sensor hits is examined. The sensor efficiency, both globally and position resolved, is analyzed for different threshold and bias voltage settings.

6.1 THE STRIXEL FEATURE

Before considering the full test beam analysis, the raw data from the MuPix prototype needs to be studied. The raw pixel hit map, i. e. an histogram of the registered hit positions in row and column coordinates is shown in Figure 6.1 for an example run. Unfortunately, the hit map does not show a uniform distribution of hits. Instead, a clear horizontal stripe-like pattern is visible. Out of groups of four rows, two neighboring rows have almost no hits and the other two rows display uniformly distributed hit registration. The hit counts for the lowest two rows are about 10 times larger than the average hit counts for the regular ones.

An examination of the chip schematics revealed a possible problem with the readout and reset circuitry. When a registered hit is processed by the column logic, it reads the corresponding row address from a fixed memory cell and resets the pixel. For half of the cells, the readout timing was incorrect and a zero address was stored instead of the actual address. The incorrect timing is not completely deterministic as a minor fraction of the pixels in the defective rows are active and generate hits with correct addresses. The column address was not affected as it was generated at a different point in the readout circuit. The alternating structure in groups of two rows is a result of the two separate digital columns per physical column, where every second pixel in a digital column is affected.

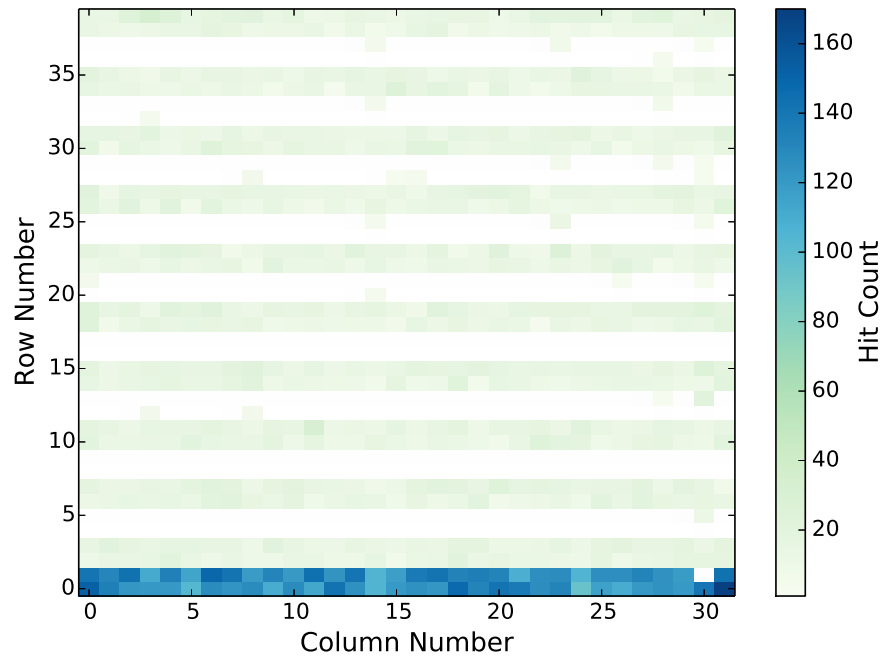


Figure 6.1: Raw pixel map for an example run with a global threshold of 838 mV, a high voltage of 70 V, and zero incidence angle. The missing pixel at position (30, 1) is a hot pixel and was removed from the analysis.

The 10 times higher hit count for the lower two rows is consistent with integration of the missing hits from the empty nine double rows. The sensor effectively works as a combination of a pixel and a strip sensor, i.e. half of the pixels have the correct row and column information while the other half only provides column information.

In order to still be able to extract meaningful information from the acquired data, a number of possible mitigation techniques exist. One possibility is to restrict measurements to the working rows. This reduces the available data by a factor of two and introduces possible edge effects at each transition between working and non-working rows. Another solution is to take advantage of the low particle rates and match reconstructed tracks to possible pixel hits using only the column information. This is the approach taken for this data analysis.

6.2 CLUSTERING

A single particle can generate more than one pixel hit due to charge sharing effects between neighboring cells. The distribution of the cluster sizes can be used to measure the strength of these charge sharing effects. Clusters are constructed for the raw pixel hits using a simple clustering algorithm. Starting from a seed pixel, all active pixels that are directly connected are combined. Pixels that are only connected at the corner and do not share a common edge are treated as two separate clusters. This procedure is independent of the choice of seed pixel, due to the requirement of a direct connection.

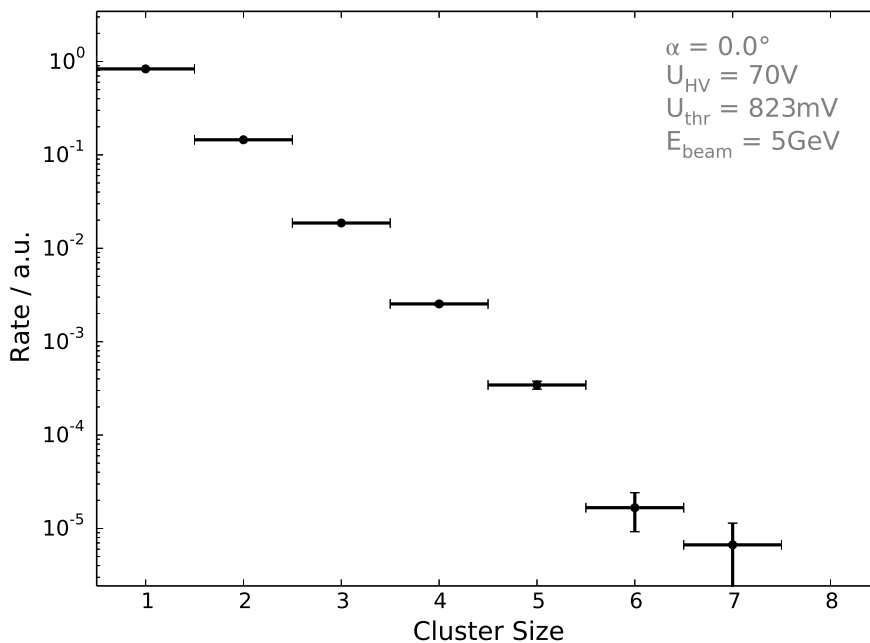


Figure 6.2: Distribution of cluster sizes for a run with a global threshold of 823 mV, a high voltage of 70 V, and zero track incidence angle. These settings correspond to the highest efficiency.

The resulting cluster size distribution is shown in Figure 6.2. Single pixel clusters are strongly preferred and clusters containing two or more pixels are suppressed by an order of magnitude. Due to the faulty rows, there must be an inherent bias towards lower cluster sizes. However, this affects only half of the pixels for cluster sizes above two and only along one direction.

The qualitative picture does not change for different settings. The shown configuration is a setting with the highest tested

bias voltage of 70 V and the lowest tested threshold of 823 mV. This corresponds to a high efficiency that will be discussed later on. Higher thresholds reduce the possibility that a small signal shared from a neighboring pixel can activate the comparator. For other configurations the single pixel clusters fraction is increased, especially for higher thresholds.

The very small clustering rate is expected and a result of the shape of the sensitive sensor area. The active area underneath each pixel cell forms a thin sheet with a depth of around $15\ \mu\text{m}$ [67] that is small compared to the pixel size of $92\ \mu\text{m} \times 80\ \mu\text{m}$. In combination with the applied high voltage, the generated charge drifts quickly to the sensor electrode. Charge transfer to neighboring cells can only occur at the very edges of each cell and is therefore suppressed.

In hybrid pixel sensors, charge sharing is usually larger due to the thicker sensitive layer and the Lorentz-drift in the magnetic field. Signal amplitude measurements can be used to enhance the single hit resolution by using appropriately weighted sums to determine the center of mass of a cluster. The binary readout of the MuPix sensor allows only small improvement of the single hit resolution. For the Mu3e experiment, single hit resolution is not a limiting factor. Large cluster sizes would only increase the output data rate without significant resolution benefits.

6.3 TRACK MATCHING AND RESOLUTION

A prerequisite for the efficiency measurement is a correct matching of reconstructed tracks and possible hits of the MuPix device. Possible ambiguities could arise when multiple tracks are reconstructed in the sensor area. However, as shown previously in Figure 5.5, the track rate is below 1 track/event for the whole test beam campaign. To further reduce possible interference from matching ambiguities, only events with exactly one track are considered. To accommodate the missing column information, reconstructed tracks and pixel hits are matched using only the column information with a matching cut of 1.5 pixels. The specific cut value was manually chosen to be slightly larger than the pixel size plus the telescope resolution. With these cuts, around 2×10^4 reconstructed tracks are available for each tested configuration.

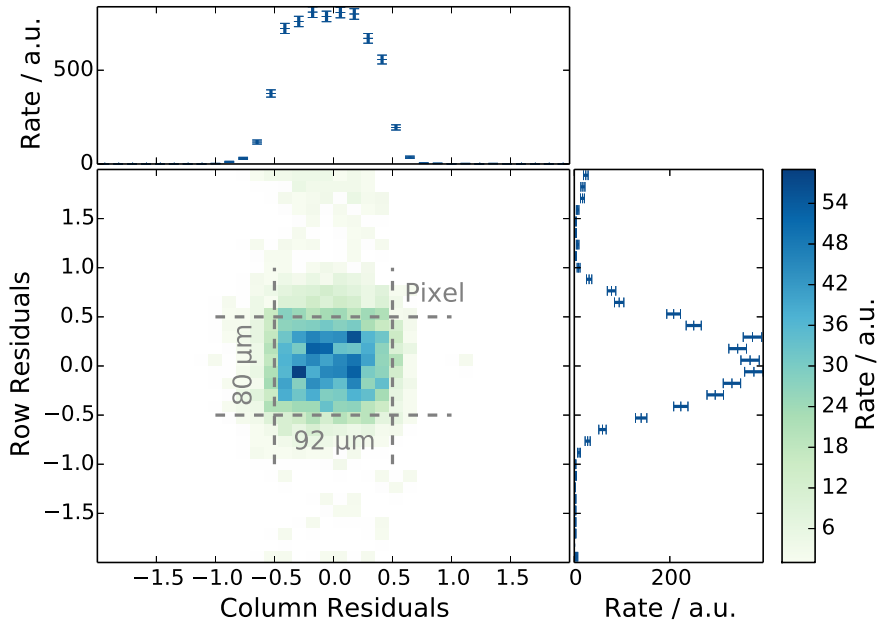


Figure 6.3: Residuals between track position and matched pixel position in digital pixel coordinates on the sensor plane for a track incidence angle of zero degrees. The central graph shows the residuals in the plane and the upper and right graphs show the projections along the column and row direction.

The resulting residuals between the extrapolated track position and the matched pixel position of the closest pixel for an example dataset are shown in Figure 6.3. Due to the row address problem, the residuals are only correct for the hits inside the working rows. For the other rows, the residuals are shifted by the nominal row address. The remnants of this effects are visible at the upper edge of the plot. The residual distribution is the convolution of the intrinsic hit distribution of a single pixel with the uncertainty distribution of the extrapolated track position. With binary readout the hit distribution inside a pixel is expected to be uniform.¹ The extrapolated track position is assumed to be of Gaussian shape with a width determined by the telescope resolution.

The smearing at the edges of the projected distributions are a result of the telescope resolution. The extrapolated telescope resolution is significantly smaller than the pixel size, around 0.1 to 0.2 the average pixel size or 9 μm to 18 μm . The nominal pixel size is marked with the dashed lines. Within the telescope resolution, no systematic misalignment between the track and

¹ Under the assumption of a uniform track distribution inside a pixel.

the pixel positions is visible. The hit resolution is therefore determined by the pixel pitch.

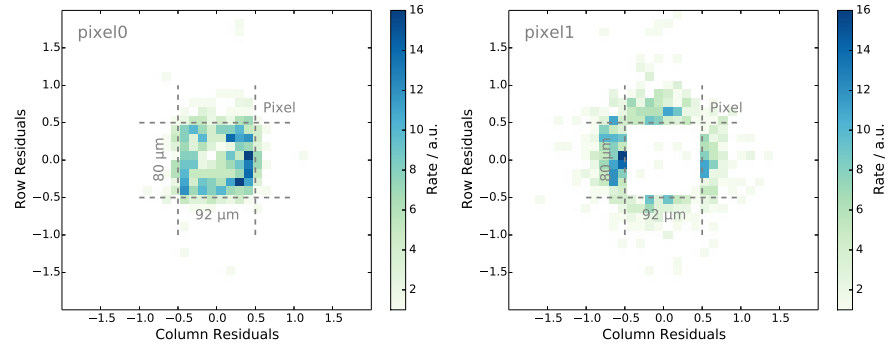


Figure 6.4: Residuals between the track position and nominal pixel position for tracks matched with pixel clusters of size two. The left plot shows the residuals for distances to the closest pixel in the cluster and the right plot show the residuals to the other pixel.

Although most of the hits on the MuPix sensor are single pixel hits, it is interesting to look at the residuals specifically for the clusters with more than one active pixel. For clusters, residuals can be separately defined for each constituent pixel. This has been done for two pixel clusters in Figure 6.4, where the track residuals are shown separately for the first and the second pixel ordered by distance to the track.

Both distributions are localized at the corners of the nominal pixel position with a width comparable to the telescope resolution. Two-pixel clusters correspond to hits that are located very close to the border between two pixels. Only at these positions can the generated charge reach two separate cells, a finding consistent with the suppressed rate of two pixel clusters.

6.4 EFFICIENCY

With an effective matching between hits and extrapolated tracks, the efficiency can be calculated. To accommodate for variations in the track density, the efficiency is normalized using the initial tracks. All tracks extrapolated to the nominal sensor area are matched with the closest available hit using the column distance. The efficiency ϵ is calculated as the ratio

between the total number of tracks and the tracks that have a matched hit within a column distance of 1.5, i. e.

$$\epsilon = N_{\text{matched}}/N_{\text{total}}. \quad (6.1)$$

Noisy pixels are removed before the matching and all tracks inside the nominal pixel matrix are considered. Due to the strong correlation between the number of matched and total tracks, the efficiency errors are calculated using Bayesian confidence intervals calculated with the TEfficiency procedure in ROOT [82].

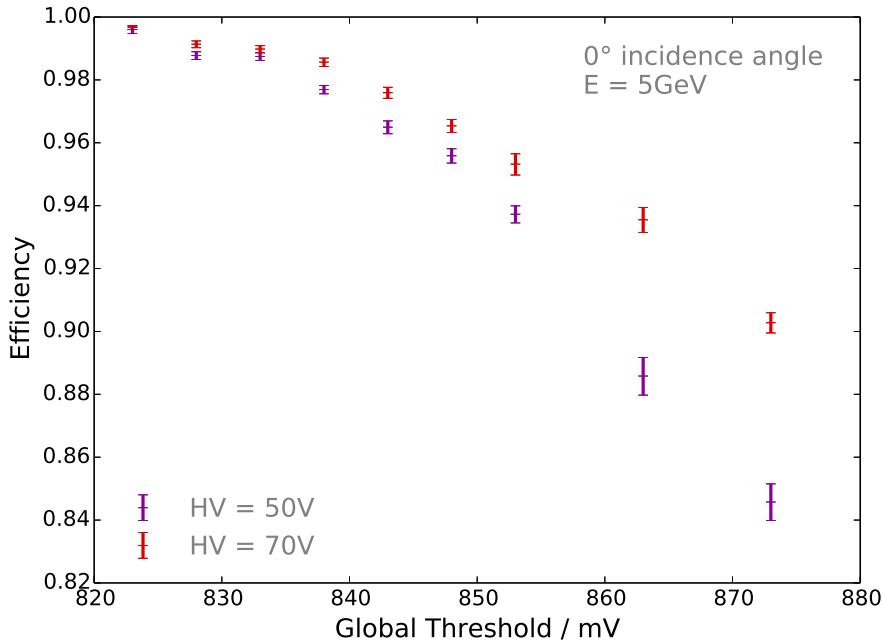


Figure 6.5: Global sensor efficiency as a function of the global threshold voltage for a fixed beam incidence and two different high voltage settings.

The global efficiency as a function of the configured global threshold is shown in Figure 6.5. A clear rise of the efficiency for lower thresholds is visible. The maximum efficiency of 99.5% is reached at the minimal threshold of 823 mV. The efficiency usually follows a sigmoidal curve. It should start at zero for very large thresholds where no signal reaches the configured threshold. As the threshold decreases, the efficiency increases as a larger fraction of the statistically varying signal amplitude reaches the threshold. Above a certain value, all signals surpass the threshold and the efficiency should reach a plateau at the

maximum efficiency. The width of the transition region defines the strength of the statistical signal variations.

Here, the width has two separate causes: the intrinsic sensor noise and the per-pixel variations. The latter can be significantly reduced by tuning the additional per-pixel thresholds to account for production variations between the per-pixel circuits. For the first measurements presented here, no tuning was performed and the measured width can not be used to estimate the sensor noise.

Figure 6.5 shows the efficiency for two different bias voltages. Higher bias voltages enlarges the depletion zone as discussed in Chapter 4. The incident particles traverse a larger active zone and consequently generate more charges. The signal amplitude is larger and a higher fraction of signals pass the given threshold, consistent with the measured efficiency increase.

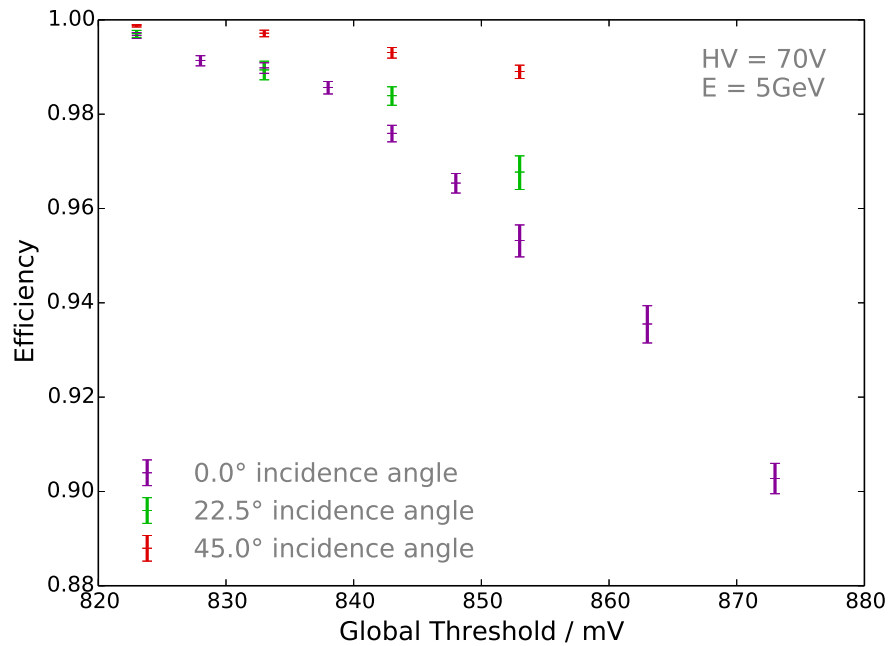


Figure 6.6: Global sensor efficiency as a function of the global threshold voltage for a fixed high voltage and three different beam incidence angles.

A similar effect can be achieved by changing the incidence angle of the tracks for a fixed threshold. Larger incidence angles increase the effective path length by a factor of $1/\cos\alpha$ compared to normal incidence. Consequently, the generated charge and the resulting signal amplitude increase. This effect can be seen in Figure 6.6, where the efficiency as a function of the

threshold is plotted for different incidence angles. The increase from 22.5° to 45° has a larger effect than the increase from 0° to 22.5° due to non-linearity of the $1/\cos \alpha$ term.

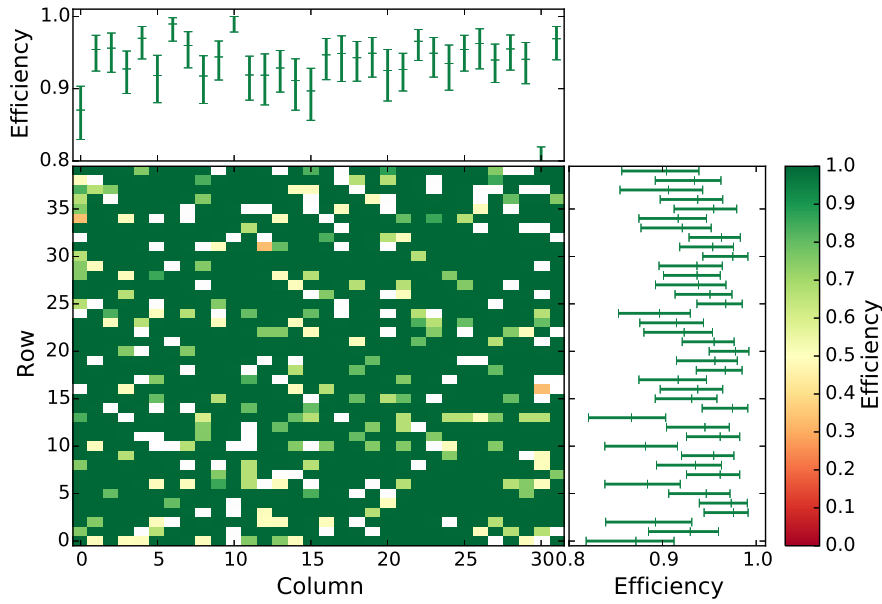


Figure 6.7: Efficiency distribution over the pixel matrix for a global threshold of 863 mV, a high voltage of 70 V, and zero track incidence angle. The global efficiency is 89%.

To verify that the sensor response does not depend on the pixel location, one can investigate the efficiency as a function of the track position. This is done in Figure 6.7, where the efficiency is plotted for a configuration with a low global efficiency of 89%. Since the track matching uses only the column information, the efficiency can be calculated also for the faulty row addresses. No obvious structures are visible in the efficiency map, i. e. the increased threshold affects all pixels uniformly within the statistical limits of the acquired data.

The high telescope resolution also allows a position measurement within each pixel and enables the investigation of sub-pixel efficiencies. However, the number of reconstructed tracks per configuration results in only around ten hits per pixel. Since only statistical fluctuations between the pixels and no systematic position dependent effects are visible on the level of the whole pixel matrix, the matrix can be folded back into a single four-by-four submatrix. This increases the reconstructed tracks per pixel under the assumption that all submatrices behave identical.

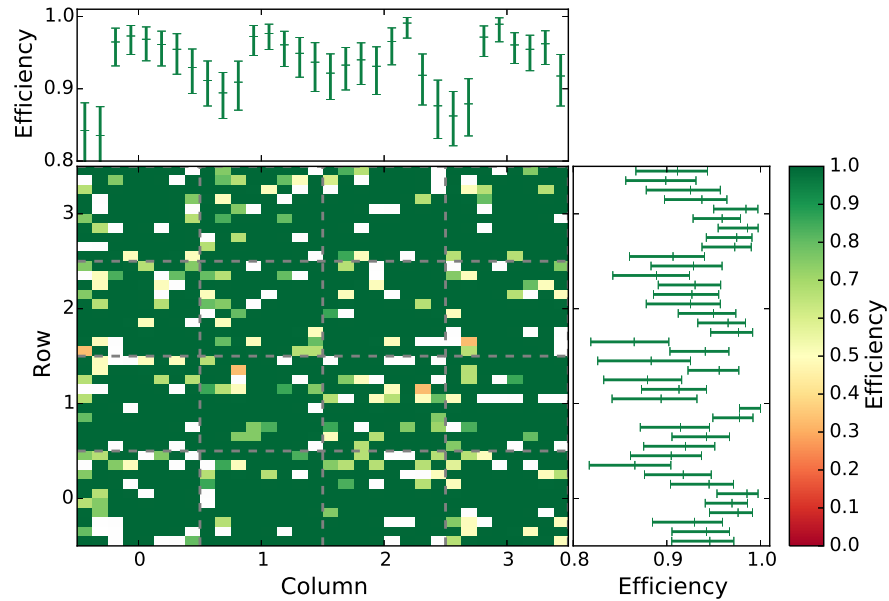


Figure 6.8: Subpixel efficiency for a four-by-four submatrix. To increase the statistical power, the track positions for all non-overlapping four-by-four submatrices are folded into the first submatrix. The sensor settings are identical to Figure 6.7.

The folded efficiency is shown in Figure 6.8 for the same sensor configuration. The overall efficiency is decreased and, in addition, some structures are visible in the the projected efficiencies along the column and row direction. Additional drops in the efficiency coincide with the pixel edges within the telescope resolution. The efficiency drop at the edges are a result of the previously discussed two-pixel clusters. Their generated charge is shared between the neighboring cells and each signal has less chance to be over the threshold.

6.5 SUMMARY

The test beam measurements show that high-voltage monolithic active pixel sensors can be successfully operated with a high efficiency of $>99\%$. Apart from the row addressing problem, the MuPix4 prototype shows a uniform response both over the given pixel matrix and locally inside each pixel. This is the first systematic efficiency and resolution measurement using this novel prototype design.

The results are encouraging, but a few caveats still exist. One important missing piece is a simultaneous noise measurement

to verify that the efficiency is not a result of spurious coincidences of tracks with noise hits. One indicator could be the number of unmatched hits, i. e. the hit rate after removing hits matched to a track. Unfortunately, the telescope and device under test have different integration times that also vary between events. The telescope also has a tracking efficiency below 100 %. A large number of unmatched hits therefore result from genuine particle tracks that are not reconstructed in the telescope. This is a severe limitation of the telescope setup. Initial lab measurements with injection pulses and radioactive sources indicated signal over noise ratios above 20 [58, 60].

The lowest threshold configuration was limited by read out rates of the data acquisition system. Lower threshold saturated the readout due to single noisy pixels and lead to unstable running conditions. Ideally, a large efficiency plateau should be available to have a wider set of possible working points. Later test beam measurements with the MuPix6 and MuPix7 chips could measure such an efficiency plateau. The later measurements were performed using the updated readout system with the EUDET telescope setup and a custom MuPix telescope [72].

All measurement shown here were taken with untuned sensors. By tuning the per-pixel threshold corrections, a significant increase in uniformity can be achieved. The given measurements are therefore the base upon which further improvements can be build.

Part II

TRACK FITTING WITH MULTIPLE SCATTERING

Precise knowledge of a particle's momentum and position is the key to almost any successful particle physics experiment. It is particularly important for the Mu3e experiment to suppress possible backgrounds and reach the projected branching ratio sensitivity. Consequently, particle tracking detectors are at the core of many current experimental setups. In contrast to e.g. calorimetric measurements, where the quantities of interest can be measured directly, tracking devices require additional reconstruction steps to recover the full particle trajectory from the tracker measurements.

Reconstructing the particle trajectory from the measurements involves two core components: a deterministic track model that describes the idealized particle motion and a statistical description of possible uncertainties from the measurements and from interactions of the particle with the material it traverses. The distinction between these two components is not a strict one, i.e. some effects can be described both as a deterministic element of the track model or as a statistical contribution to the uncertainty.

The different track fits that will be discussed later in this work, differ in their assumed propagation model and in the type of uncertainties that are assumed. In order to understand their behaviour in different regimes, i.e. configurations with different dominating uncertainties, it is necessary to fully understand the interplay of track models and uncertainties. While this topic is technical in nature, a thorough introduction is needed to understand the following discussions on the various track fit and their behaviour.

In this chapter, I will discuss the helical track model, track parametrizations, and sources of uncertainty. A detailed discussion of the helical track model can also be found in Appendix A.

7.1 ANALYTIC HELIX PROPAGATION

A charged particle moving in a magnetic field is subject to the Lorentz force [32]. In the absence of an electric field, the resulting equations of motion are given by

$$\frac{d\mathbf{p}}{dt} = \mathbf{F} = q(\mathbf{v} \times \mathbf{B}), \quad (7.1)$$

where natural units with $\hbar = c = 1$ are assumed.

Under the assumption of negligible energy loss, i. e. constant absolute momentum, the relation $ds/dt = v$ between path length, time, and absolute velocity holds. The momentum vector contains information on the direction and the curvature, which is related to the absolute momentum. It is usually easier to separate these two parameters and rewrite the equations of motion as two sets of ordinary first-order differential equations for the position \mathbf{x} and normalized momentum or tangent vector $\hat{\mathbf{T}} = \mathbf{p}/p$ as functions of the integrated path length s along the particle trajectory

$$\frac{d\mathbf{x}}{ds} = \hat{\mathbf{T}}, \quad (7.2)$$

$$\frac{d\hat{\mathbf{T}}}{ds} = \hat{\mathbf{T}} \times \frac{q}{p} \mathbf{B}(\mathbf{x}). \quad (7.3)$$

The track model is the solution to these six coupled differential equations.

For arbitrary magnetic fields, the equations of motion (7.2) have no analytical solution and require numerical methods. There are a number of well established methods, e. g. [16, 47, 48], mostly based on the Runge-Kutta methods [1, 2] for numerically solving differential equations. However, they are computationally expensive and are not the first choice for fast tracking with the Mu3e experiment.

A typical magnetic field configuration for collider detectors and the configuration used in the Mu3e experiment is a solenoid magnet. In the inner central volume of the solenoid, the field can be reasonably well described by a constant axial magnetic field. How well this approximation holds depends on the specific magnet configuration. The solenoid magnet for the Mu3e experiment was specifically designed to be as homogeneous as possible for the largest possible area as discussed in Chapter 3. In the following, the field axis is used to define the z -axis of the global Cartesian coordinate system, i. e. $\mathbf{B} = B_z \hat{\mathbf{Z}}$

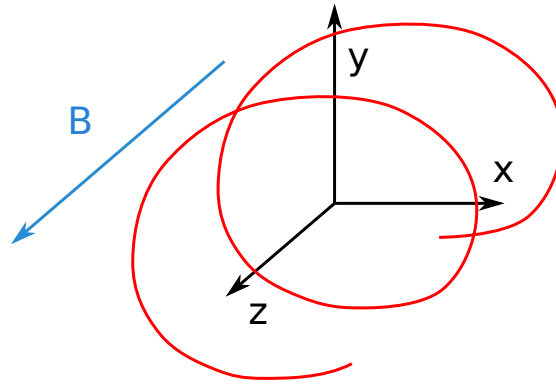


Figure 7.1: Helical trajectory along the z-axis.

For a constant magnetic field, the equations of motion (7.2) can be solved analytically. The full derivation and the explicit analytical solution is described in Appendix A. The solution is a helix trajectory along the magnetic field direction, i. e. a circular motion in the plane transverse to the field direction and a linear drift along the field direction as shown in Figure 7.1.

7.2 TRACK PARAMETERS

The derivation of the helix trajectory in the previous section directly used the position and momentum or tangent vector to define the track. Depending on the circumstances other parametrizations are more appropriate. In addition, only five parameters are required to fully describe the trajectory for a given reference surface. Additional parameters, e. g. when using the global parameters, introduce correlations among the parameters and complicate e. g. the propagation of uncertainties.

The track parameters \mathbf{a} can be calculated at every point on the trajectory. A function that propagates the track parameters as a function of the initial parameters \mathbf{a}_0 and the path length s can be formally defined:

$$\mathbf{a} = f(\mathbf{a}_0, s). \quad (7.4)$$

The track parameters need to be propagated not only along the trajectory, but also to specific points of interests, e. g. to the intersection with a measurement surface or to the closest approach to a possible vertex position. With the helix trajectory this is equivalent to finding the corresponding path length. This

can be done analytically in most cases. A full derivation of the initial trajectory and the relevant propagation equations for the helical propagation can be found in Appendix A.

The definition of the different track parameters in the following section follows the definitions in [38].

7.2.1 Global Parametrization

The global parameters $\mathbf{x}, \hat{\mathbf{T}}, q/p$ use the position vector, tangent vector, and signed inverse momentum to define the track in the global Cartesian coordinate system. This is not a minimal set of parameters, but allows a direct calculation of the trajectory in the global coordinate system.

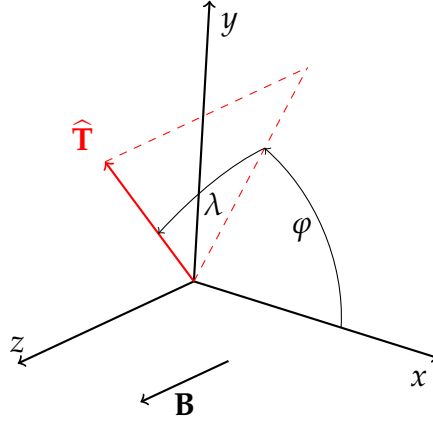


Figure 7.2: Definition of the coordinate system and the global track angles φ and λ .

Due to the normalization, the tangent vector has only two free parameters. Instead of using its Cartesian coordinates it can be defined using two global direction angles

$$\hat{\mathbf{T}} = \begin{pmatrix} \cos \lambda \cos \varphi \\ \cos \lambda \sin \varphi \\ \sin \lambda \end{pmatrix} \quad (7.5)$$

as shown in Figure 7.2. The momentum vector is the tangent vector scaled with the absolute momentum, i. e. $\mathbf{p} = p\hat{\mathbf{T}}$. The dip angle λ measures the relative strength of the longitudinal motion and is proportional to the longitudinal momentum. The azimuth angle φ indicates the direction in the global xy-plane or transverse plane.

7.2.2 Curvilinear Parameterization

The curvilinear track parameters $x_{\perp}, y_{\perp}, \varphi, \lambda, q/p$ as discussed in [38] define the track at the point of closest approach to a reference position.

The track direction is defined by the global track angles φ and λ that were previously defined and q/p is again the signed inverse momentum.

The track position is defined by the offset $[x_{\perp}, y_{\perp}]$ in the curvilinear plane. The curvilinear coordinate system is a local system with coordinates $[x_{\perp}, y_{\perp}, z_{\perp}]$ defined at every point on the trajectory. It is defined as a plane perpendicular to the track, i. e. the normal unit vector of the curvilinear plane is the tangent vector of the track at the given position. The plane is spanned by two unit vectors that are defined as follows

$$\hat{\mathbf{U}} = \frac{\hat{\mathbf{Z}} \times \hat{\mathbf{T}}}{\|\hat{\mathbf{Z}} \times \hat{\mathbf{T}}\|}, \quad (7.6)$$

$$\hat{\mathbf{V}} = \hat{\mathbf{T}} \times \hat{\mathbf{U}}. \quad (7.7)$$

The three unit vectors of the curvilinear system are orthonormal. By construction, the $\hat{\mathbf{U}}$ unit vector lies in the global xy -plane. In the case of a transverse track, where the tangent vector lies also in the xy -plane, the $\hat{\mathbf{V}}$ unit vector is identical to the $\hat{\mathbf{Z}}$ unit vector. Otherwise, the $\hat{\mathbf{V}}$ unit vector is rotated away from the z -axis. Since the curvilinear plane is orthogonal to the track direction, z_{\perp} changes correspond to path length changes and would define a new curvilinear system.

7.3 PROPAGATION OF UNCERTAINTIES

Often, one is not interested in the full propagated parameters but only in the propagated corrections along a reference trajectory

$$\mathbf{a} + \Delta = f(\mathbf{a}_0 + \Delta_0, s) \quad \text{with } \mathbf{a} = f(\mathbf{a}_0, s). \quad (7.8)$$

Since only small corrections are now considered, the propagator can be expanded around the reference trajectory \mathbf{a}_0 for a fixed propagation path length in terms of the corrections, i. e.

$$\Delta = f(\mathbf{a}_0, s) - \mathbf{a} + \frac{\partial f}{\partial \mathbf{a}} \Delta_0 + \mathcal{O}(\Delta_0^2) \approx F_s \Delta_0. \quad (7.9)$$

The whole propagation dynamics is now contained in the Jacobian matrix $F_s = \partial f / \partial \mathbf{a}$. The validity of this linearization depends on the non-linear nature of the initial propagator, which depends among other things on the specific choice of parameters.

Curvilinear parameters are used for the propagation in the helical track model. Here, all parameters changes are orthogonal to each other and to the initial track direction. This means that the linearization is valid over a wide range of parameters and propagation path lengths.

The specific form of the propagation or transport Jacobian for the helical model can be found in [38], where it is derived for a helix with arbitrary axis. For the computations in this work a simplified version is used that assumes a magnetic field direction along the z-axis and allows a simpler computation.

For the following discussions it is instructive to consider how small changes in the parameters at one point of the trajectory effect the curvilinear parameters after a given propagation path length in leading order. Initial position changes are orthogonal to the track direction and do not change along the trajectory. This means that an initial position uncertainty yields the same position uncertainty at a later position. Initial direction changes also effect the position and depend linearly on the path length. Direction uncertainties, e.g. from multiple scattering, can lead to large position uncertainties after long track propagation. Changes in momentum, i. e. the curvature of the track, mostly affect the position in the transverse plane.

7.4 SOURCES OF UNCERTAINTIES

All effects that are not described by the deterministic track model are described as additional statistical noise. For all practical purposes, the noise is assumed to be normally distributed with a defined covariance matrix Σ . Multiple noise sources are combined by adding their separate corresponding matrices.

7.4.1 *Measurement Uncertainties*

All particle detectors have a finite resolution and the measured nominal position differs from the true crossing point of the particle. For the case of a silicon pixel sensors with pixel pitches

l_u and l_v along each measurement direction, the center of a pixel is usually used as the measured position. Ignoring possible charge sharing effects, the true crossing point can be anywhere inside the pixel and the corresponding residual distribution is a uniform distribution with width l_u and l_u along each direction. An corresponding normal distribution is defined by using the variance of the uniform distribution. In the local measurement system the covariance matrix is diagonal and given by

$$\Sigma_{\text{pixel}} = \begin{pmatrix} l_u^2/12 & 0 \\ 0 & l_v^2/12 \end{pmatrix}. \quad (7.10)$$

7.4.2 Multiple Coulomb Scattering

A charged particle traversing a medium will be deflected by consecutive elastic scattering at the nuclei of the medium, mostly due to the Coulomb interaction between the particle and nuclei charge. This effect is called multiple Coulomb scattering. Its theory was first discussed by Wentzel [4] and fully developed by Molière and Bethe [5–8]. It describes the distribution of the effective scattering angles and displacement after the traversal as shown in Figure 7.3. The resulting distribution of scattering angles has a vanishing mean, a normally distributed core, and additional tails due to large angle single scattering events.

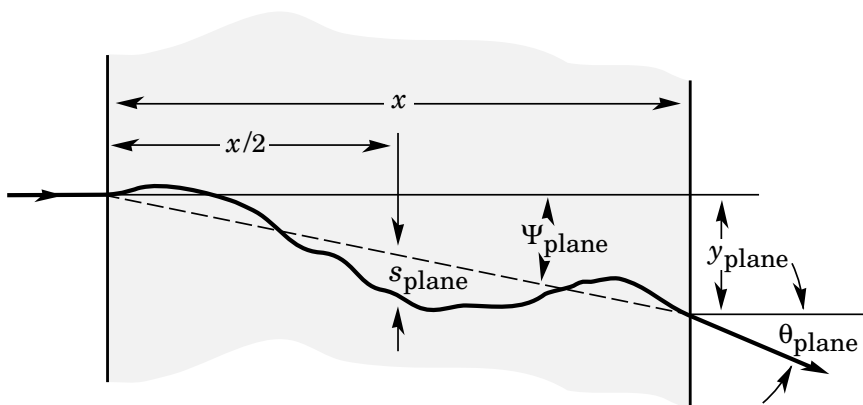


Figure 7.3: Effect from multiple Coulomb scattering on the direction of a particle trajectory. From [73]

The scattering can be described either by the angular distribution in space or by projecting the angular distribution onto two orthogonal planes. For most practical purposes the planar scattering distribution is used and approximated by a normal distribution. Its width can be described by the following parametrization for the RMS of the 98 % core of the distribution according to Highland [15, 73]

$$\theta_0 = 13.6 \text{ MeV}/c \frac{q}{p} \sqrt{\frac{x}{\beta^2 X_0}} \left(1 + 0.038 \ln \left(\frac{x}{X_0} \right) \right), \quad (7.11)$$

where p is the momentum in MeV/c, q is the absolute charge of the particle in units of e , β is the relativistic velocity, and x/X_0 is the thickness of the material in units of the radiation length X_0 . The radiation length X_0 is a material constant that depends mostly on the nuclear charge, i. e. it is generally longer for lighter elements.

The additional displacement due to multiple scattering is strongly correlated to the scattering itself. The width of the displacement distribution is given by $\sigma_y = x \theta_0 / \sqrt{3}$, which means that for thin scatterers the displacement can usually be neglected.

We performed our own measurements of multiple Coulomb scattering in thin 50 μm to 140 μm silicon targets during the test beam campaigns at DESY. We found good agreement for the measured width of the multiple scattering distribution with the theoretical width described above. However, the shape of the distribution was best described by a Student's t -distribution with larger tails than a Gaussian [70]. While this can be considered in the future, only the Gaussian core is of interest for this work.

The planar scattering angles are defined in two planes that are orthogonal to each other and that both contain the initial track direction. One such system is the curvilinear system defined above with the two planes spanned by $(\hat{\mathbf{T}}, \hat{\mathbf{U}})$ and $(\hat{\mathbf{T}}, \hat{\mathbf{V}})$ respectively (see also [50]). The planar scattering angles correspond to a change of slope in this system and the contribution to the global change of direction can be written as

$$d\hat{\mathbf{T}} = \hat{\mathbf{U}} dx'_\perp + \hat{\mathbf{V}} dy'_\perp. \quad (7.12)$$

The change of direction can also be written in terms of the global track angles by using the definition of the tangent vector in Equation 7.5

$$d\hat{\mathbf{T}} = \hat{\mathbf{U}} \cos(\lambda) d\varphi + \hat{\mathbf{V}} d\lambda \quad (7.13)$$

Comparing the two expressions shows that scattering angles along $\hat{\mathbf{V}}$ correspond directly to equivalent λ changes whereas scattering angles along $\hat{\mathbf{U}}$ are related to changes in φ by an additional scaling given by $\cos(\lambda)$. The resulting global angles' covariance matrix due to multiple scattering is diagonal and can be written as follows.

$$\Sigma_{MS} = \begin{pmatrix} \sigma_{\varphi,MS}^2 & 0 \\ 0 & \sigma_{\lambda,MS} \end{pmatrix} = \begin{pmatrix} \theta_0^2 / \cos^2(\lambda) & 0 \\ 0 & \theta_0^2 \end{pmatrix} \quad (7.14)$$

The description in Figure 7.3 shows a normal incidence of the track on the scattering medium. In most cases, the track will have an additional incidence angle α with respect to the material normal. When calculating the planar scattering angle, the effective path through the material, i. e. $x_{eff} = x / \cos \alpha$, should be used.

7.4.3 Other Effects

Additional sources of uncertainty are mostly due to energy losses of the particle while traversing a medium or a detector layer. As discussed e. g. in [73], low energy electrons lose energy mostly via ionization¹. Due to the thin detector material, the energy loss is usually very small compared to the total energy of the particle. Another effect is Bremsstrahlung when traversing a detector layer. However, this is usually relevant only at very high energies and with thick detectors, both of which are not the case at the Muze experiment.

¹ Otherwise, our silicon detectors would not work

TRACK FITS

Track parameters are reconstructed from the measurements by fitting the full statistical track model, i. e. the combination of an idealized deterministic track propagation and a statistical error description, to the measurements. There are multiple algorithms available which usually differ in the treatment of the uncertainties. Often, they can be categorized either as fast and approximate or as slow and precise.

In the following chapter I will discuss two track fits of the former category: a single helix fit based on the fast Karimaeki circle fit and a novel track fit based on hit triplets which both built on the helical track model. I will also discuss the general broken lines fit, an extended track refit that belongs to the latter category.

Having a correct fit model is not only relevant for determining the optimal track parameters. It is also an important tool to tackle the related problem of pattern matching and track finding, i. e. determining which measurements belong to the same particle trajectory. With a correct fit model, the fit quality can be used to judge possible candidate associations.

8.1 METHOD OF LEAST SQUARES

In general, the principle of maximum likelihood (see e. g. [31]) is applied to estimate optimal parameters for a given statistical model. Under the assumption of normally distributed residuals, maximizing a likelihood expression is equivalent to minimizing the corresponding objective function that is given by the sum of weighted squared residuals. This is called the method of least squares. For a given vector of measurements \mathbf{m} with corresponding covariance matrix Σ and a track model $\mathbf{f}(\mathbf{a})$ that calculates the expected measurements as a function of a set of track parameters \mathbf{a} , the least squares objective function can be written in matrix notation as follows:

$$S = (\mathbf{m} - \mathbf{f}(\mathbf{a}))^T \Sigma_m^{-1} (\mathbf{m} - \mathbf{f}(\mathbf{a})). \quad (8.1)$$

The so-called precision matrix, the inverse of the covariance matrix, is used to weight the residuals. This ensures that more precise measurements have stronger contributions to the result and that possible correlations between the measurements are correctly accounted for. The best-fit parameters are those that minimize the objective function.

Minimizing the objective function (8.1) for a general non-linear track model is usually only possible with computationally expensive numerical methods. A direct, faster solution is possible if only linear models need to be considered. This means that either the parameters are chosen such that the expected measurements $\mathbf{f}(\mathbf{a})$ from the track model depend only linearly on the parameters, or the non-linear track model is linearized around a suitable expansion point $\mathbf{f}(\mathbf{a}) \approx \mathbf{f}_0 + F \mathbf{a}$, where $F = \frac{\partial \mathbf{f}}{\partial \mathbf{a}}$ is the Jacobian matrix of the track model. The linear least square objective function is then given by

$$S = (\mathbf{m}_0 - F \mathbf{a})^T \Sigma_m^{-1} (\mathbf{m}_0 - F \mathbf{a}) \quad (8.2)$$

with $\mathbf{m}_0 = \mathbf{m} - \mathbf{f}_0$.

Minimizing the least square objective function is equivalent to solving the resulting normal equations $dS/d\mathbf{a} = 0$. For the linear case the normal equations are the following set of linear equations

$$F^T \Sigma_m^{-1} F \mathbf{a} = F^T \Sigma_m^{-1} \mathbf{m}_0. \quad (8.3)$$

Under the assumption that the Jacobian matrix F and the precision matrix Σ_m^{-1} are well behaved, the resulting best-fit parameters and the corresponding covariance matrix can be expressed as follows

$$\mathbf{a} = \left(F^T \Sigma_m^{-1} F \right)^{-1} F^T \Sigma_m^{-1} \mathbf{m}_0, \quad (8.4)$$

$$\Sigma_a = \left(F^T \Sigma_m^{-1} F \right)^{-1}. \quad (8.5)$$

The matrix inversions should be understood as purely symbolic expressions. Depending on the situation the solution can be calculated without performing an explicit numerical inversion of the relevant matrices.

The computational complexity of the solution depends on the specific form of the covariance matrix and the Jacobian matrix. For a dense system the complexity scales with $\mathcal{O}(n^3)$ where

n is the number of measurements. For special cases, e. g. independent measurements with a diagonal covariance matrix and a simple track model, the computational complexity can be significantly reduced to $\mathcal{O}(n)$.

If the track model and the uncertainty description are consistent, then the resulting sum of squared residuals is drawn from a χ^2 distribution (see e. g. [31]) with the number of degrees of freedom given by the number of degrees of freedom of the fit, i. e. # measurements - # parameters. Deviations from the expected χ^2 distribution indicate inconsistencies, e. g. from an invalid linearization, under- / overestimated measurement uncertainties, or simply from a wrong model.

8.2 SINGLE HELIX FIT

Fitting a single helix directly from measured positions without any additional assumptions is a highly non-linear problem. In the helical track model the particle motion in three dimensions derived in Chapter 7 comprises two lower-dimensional motions, a purely circular motion in the transverse plane and a linear motion along the longitudinal axis as discussed previously. The single helix fit described here splits the three-dimensional helix fit into two two-dimensional fits, a circle fit in the transverse plane followed by a line fit along the magnetic field direction, that are performed separately. This separation is valid if the measurements along the beam direction and the ones transverse to the beam direction are independent.

The fast approximate circle fit developed by Karimäki [22] is used to estimate the distance of closest approach to the origin d_{ca} , the transverse track angle φ at the point of closest approach, and the transverse curvature κ from two-dimensional measurements $\mathbf{m}_i = [x_i, y_i]$ as shown in Figure 8.1. It assumes independent measurements corresponding to a diagonal covariance and precision matrix. With these assumptions the objective function for the least square formalism takes on the form

$$S = \sum w_i \epsilon_i^2, \quad (8.6)$$

where the ϵ_i are the residuals of the fitted circle and the measurements, i. e. $\epsilon_i = \|\mathbf{m}_i - \mathbf{f}(d_{ca}, \varphi, \kappa)\| - (1/\kappa)$. Assuming the

residuals are small compared to the circle radius, they can be written in terms of the track parameters as follows

$$\epsilon_i = \frac{1}{2}\kappa r_i^2 - (1 + \kappa d_{ca})r_i \sin(\varphi - \phi_i) + \frac{1}{2}\kappa d_{ca} + d_{ca}, \quad (8.7)$$

where r_i and ϕ_i are the polar coordinates of the measurement \mathbf{m}_i .

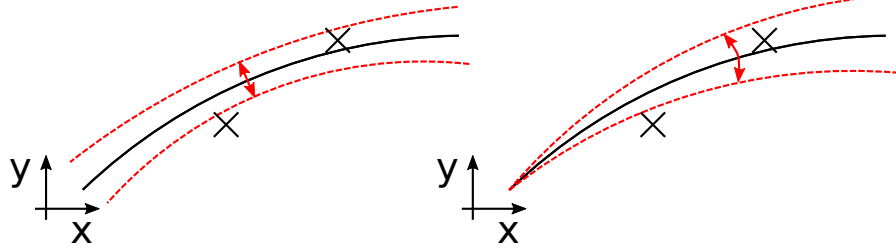


Figure 8.1: Visualization of how the circular trajectory changes as a result of the fit changes. The left part shows changes of the transverse curvature κ and the right part shows changes of the azimuth angle φ .

This approximate expression can be rewritten in terms of new parameters k and d such that the residuals can be expressed as $\epsilon_i = (1 + \kappa d_{ca})\eta_i$ where η_i depends only linearly on k and d . Instead of minimizing the original objective function, the objective function can be written as

$$S = (1 + \kappa d_{ca})^2 \hat{S} = (1 + \kappa d_{ca})^2 \sum w_i \eta_i, \quad (8.8)$$

where now only the reduced objective function \hat{S} is minimized. As a result of the reparametrization the normal equations for the reduced objective function can be solved analytically and the fit parameters can be calculated directly from the input measurements.

Using the fitted circle parameters, the fitted arc length a along the circle path can be calculated for each measurement. The arc length in the transverse plane is the projection of the integrated path length s in three dimensions onto the transverse plane, i. e. $a = \cos \lambda s$. Consequently, the motion along the z-axis as discussed in Appendix A can be written as

$$z = z_0 + \tan \lambda a, \quad (8.9)$$

and the longitudinal track parameter can be estimated by a linear regression of the measured z-position onto the fitted arc

length. Direct solutions for this problem are readily available in the literature, e. g. in Press [23].

The single helix fit allows a direct, linearized fit for the initial non-linear fitting problem. It does so by assuming uncorrelated measurements and splitting the three-dimensional problem into two lower-dimensional fits. This allows a fast calculation but ignores all possible correlations between measurements.

Other possible algorithms for the circle fit exists, e. g. conformal mapping [20], the Riemann fit [29, 30], and various iterative methods [33], but were not considered for this comparison.

8.3 SINGLE TRIPLET FIT

For the case of dominating multiple Coulomb scattering the single helix model becomes less viable. The uncertainties induced by multiple scattering dominate the position uncertainties. That means in a single helix track model, measurements are strongly correlated and the measurement covariance matrix has significant off-diagonal contributions from multiple scattering effects. The simplified assumptions for the single helix fit discussed above do not hold anymore and a different approach has to be used.

The triplets fit is a novel track fit optimized for trajectory reconstruction in multiple scattering dominated environments originally developed by André Schöning [75, 80]. This is the case for modern highly-segmented, thin tracking detectors, e. g. the Mu3e pixel tracker, where multiple Coulomb scattering can be modelled as localized discrete scatterers (compare Part i). It allows a direct reconstruction of the full particle trajectory, i. e. with local direction parameters at each hit position and a global momentum estimate, without requiring a reference trajectory, iterative procedures, or computationally expensive inversions of large matrices.

The basic building block of the triplets fit is a triplet of space points in the global Cartesian coordinate system. With highly segmented tracking detectors these space points can be calculated directly from the lower dimensional measurements. The particle trajectory is modeled as a piece-wise helix with a discrete scatterer localized at the middle hit. The detector resolution is assumed to be much better than the expected spatial

effects from multiple scattering such that the nominal hit positions are fixed points on the particle trajectory. This trajectory construction is shown in Figure 8.2.

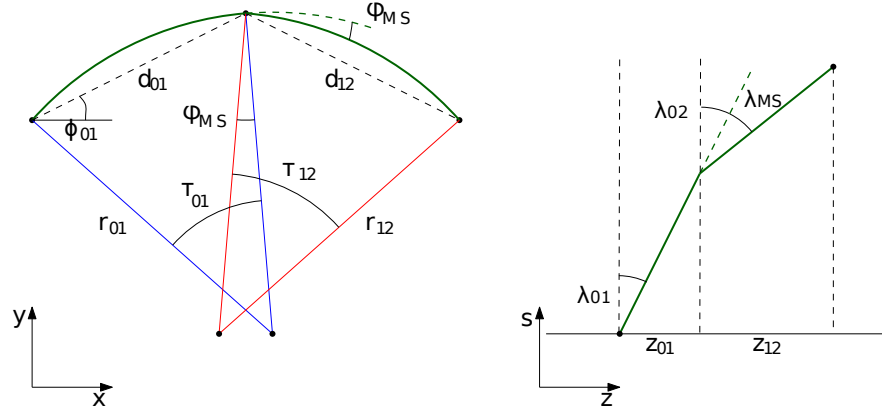


Figure 8.2: Broken helix trajectory for a hit triplet with the various angles and distances [75].

The particle momentum and its corresponding three-dimensional radius of curvature R are assumed to be conserved and the discrete scatterer changes only the direction of the track, i. e. it creates a kink in the trajectory. The kink is described as a change in the global track angles φ and λ . The corresponding kink angles φ_{MS} and λ_{MS} have expected zero mean and expected variances σ_φ^2 and σ_λ^2 , respectively. The variances can be calculated e. g. from multiple scattering theory as described in Section 7.4.2, but a more detailed analysis is required if effects from a finite hit resolution need to be considered.

Instead of minimizing spatial residuals, as in the case of the single helix fit in Section 8.2, the trajectory is fitted by finding the radius R that minimizes the scattering kink by minimizing the following objective function

$$S(R) = \frac{\varphi_{MS}(R)^2}{\sigma_\varphi^2} + \frac{\lambda_{MS}(R)^2}{\sigma_\lambda^2}, \quad (8.10)$$

where σ_φ^2 and σ_λ^2 are assumed to be constant.

Choosing R as the independent variable is not a strict requirement. The procedure can also be formulated using the three-dimensional curvature $K = 1/R \sim 1/p$, which is proportional to the inverse absolute momentum. The general idea is identical, but the resulting equations differ. Depending on the specific configuration one or the other parametrization might be

favoured mostly on numerical grounds. In the following, the algorithm is computed using the radius R .

As discussed in Section 8.1, minimizing (8.10) is equivalent to solving the corresponding normal equation $dS(R)/dR = 0$, i. e.

$$\frac{d\varphi_{MS}(R)}{dR} \frac{\varphi_{MS}(R)}{\sigma_\varphi^2} + \frac{d\lambda_{MS}(R)}{dR} \frac{\lambda_{MS}(R)}{\sigma_\lambda^2} = 0. \quad (8.11)$$

Using the triplet definition in Figure 8.2 the kink angle φ_{MS} in the transverse plane can be calculated from the azimuth angles Φ_i of the distance vectors and the propagation angles τ_i along each of the two arcs

$$\varphi_{MS} = (\Phi_{12} - \Phi_{01}) - \frac{\tau_{01}(R) + \tau_{12}(R)}{2}, \quad (8.12)$$

where the propagation angles $\tau_i(R)$ are the assumed solutions to the following transcendental equations

$$\sin^2 \frac{\tau_i}{2} = \frac{d_i^2}{4R^2} + \frac{z_i^2}{R^2} \frac{\sin^2 \frac{\tau_i}{2}}{\tau_i^2}, \quad i \in \{01, 12\} \quad (8.13)$$

which can be derived from the helix trajectory by assuming fixed endpoints and a known radius and curvature. This equation can have multiple solutions and care has to be taken to select the one corresponding to the actual physical configuration.

In the same manner, the longitudinal kink angle λ_{MS} can be calculated as

$$\lambda_{MS} = \lambda_{12} - \lambda_{01}. \quad (8.14)$$

The dip angles λ_{ij} can be derived from the z -distance, the radius, and the propagation angles using the following relation which can be directly derived from the z -component of the helix trajectory

$$\sin \lambda_i = \frac{z_i}{R\tau_i} \quad i \in \{01, 12\}. \quad (8.15)$$

The objective function defined in Equation 8.10 is now a non-linear function of the fit parameter R . Solving it directly would require an expensive numerical method, especially since Equation 8.13 is a transcendental equation that does not have an

algebraic solution. In order to find a fast solution, the procedure outlined in Section 8.1 is followed, i.e. the track model is linearized around a suitable expansion point, converting the initial construction into a linear least square problem with a direct solution.

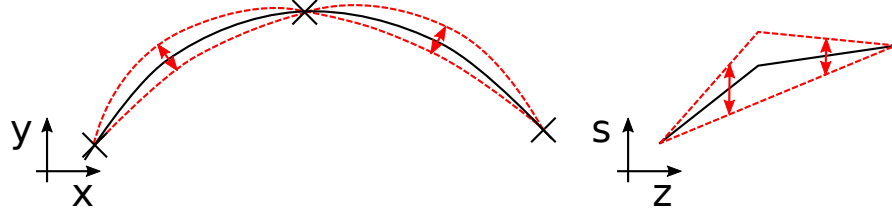


Figure 8.3: Helix linearization around the circle solution with fixed endpoints. The black line indicates the initial trajectory and the red dashed lines show possible trajectories resulting from a change in the three-dimensional radius.

To efficiently solve the normal equation (8.11) approximate expressions for $\varphi_{MS}(R)$ and $\lambda_{MS}(R)$ or $\tau_i R$ and $\lambda_i(R)$, respectively, are derived by a Taylor expansion of the track model around an appropriate expansion point. Since the scattering angles are usually small, a good expansion point is the circle solution in the transverse plane, i.e. a configuration with $\varphi_{MS} = 0$ and identical transverse radii $r_{01} = r_{12}$, as shown in Figure 8.3.

The circle solution describes the case of constant curvature in the plane transverse to the magnetic field $r_1 = r_2$ and no scattering in that plane, $\varphi_{MS} = 0$. The radius r_C of the circle in the transverse plane going through three points is given by

$$r_c = \frac{d_{01}d_{12}d_{02}}{\sqrt{-d_{01}^4 - d_{12}^4 - d_{02}^4 + 2d_{01}^2d_{12}^2 + 2d_{12}^2d_{02}^2 + 2d_{02}^2d_{01}^2}}, \quad (8.16)$$

where d_{ij} is the transverse distance between the hit i and j of the triplet as shown in Figure 8.2.

The circle solution is usually not a physical solution since the partial helices would have different three-dimensional radii violating the initial assumption of conserved momentum. However, this solution exists for any hit triplet and is usually reasonably close to a physical solution under the assumption of small scattering angles and is a good starting point for the linearisation.

Using the transverse circle, the angles of each arc, i. e. the propagation angles $\tau_{c,i}$, can be easily calculated as

$$\tau_{i,c} = 2 \arcsin \frac{d_i}{2r_c} \quad i \in \{01, 12\}. \quad (8.17)$$

Note that the above equations have two solutions, $\tau_{ij,c} \leq \pi$ and $\tau_{ij,c} > \pi$, and care has to be taken to select the physical one.¹

A common circle in the transverse plane usually results in separate three-dimensional radii that can be calculated by inserting the circle solution for the propagation angle (8.17) back into its initial transcendental equation (8.13).

$$R_{i,c}^2 = r_c^2 + \frac{z_i^2}{\tau_{i,c}^2} \quad i \in \{01, 12\} \quad (8.18)$$

The dip angles also differ for the two arcs and can be calculated by inserting the previously determined three-dimensional radius into the initial equation (8.15).

$$\lambda_i = \arcsin \frac{z_i}{\tau_{i,c} R_{i,c}} \quad i \in \{01, 12\} \quad (8.19)$$

Using the circle solution as the expansion point, the track model is linearized with respect to the curvature parameter. The propagation angles and the dip angles for each arc are approximated as

$$\tau_i(R) \approx \tau_{i,0} + \left. \frac{d\tau_i}{dR} \right|_{R_{i,0}} (R - R_{i,0}) \quad (8.20)$$

$$\lambda_i(R) \approx \lambda_{i,0} + \left. \frac{d\lambda_i}{dR} \right|_{R_{i,0}} (R - R_{i,0}) \quad (8.21)$$

where the derivatives can be calculated from the initial transcendental equations (8.13) and (8.15). With the linearized expression for the propagation angle and dip angles, the final linearized expression for the kink angles can be calculated

$$\varphi_{MS} = \varphi_{MS,0} + \alpha R \quad (8.22)$$

$$\lambda_{MS} = \lambda_{MS,0} + \beta R \quad (8.23)$$

where the different expansions points of the two triplets arcs are now absorbed in the initial kink angles and the linearization coefficients α and β . Now, the kink angles depend linearly on

¹ This mostly affects recurving tracks in the Muze tracker.

the global radius and the solution can be directly derived using the methods described in Section 8.1.

$$R = \frac{-\frac{\alpha\varphi_{MS,0}}{\sigma_\varphi^2} - \frac{\beta\lambda_{MS,0}}{\sigma_\lambda^2}}{\alpha^2/\sigma_\varphi^2 + \beta^2/\sigma_\lambda^2} \quad (8.24)$$

The fit result is the three-dimensional radius R and its variances σ_R^2 . The global track angles at each hit position ¹ can be calculated using the previously calculated linearization (8.20) and also depend only linearly on the fitted radius. The covariance of the full set of track parameters, i. e. φ , λ , and R , are to be calculated from the variance of the radius using error propagation.

¹ Separate angles can be calculated before and after the trajectory kink at the middle hit

Until now, the variances of the kink angles were assumed to be known. This would require prior knowledge of the track parameters, e. g. the momentum and direction, to estimate the expected multiple scattering variance. Since scattering angles are assumed to be small, the circle solution can be used. This means that the fit only needs to be performed once and can still use reasonable uncertainty estimates.

For the construction of the triplets fit, hit uncertainties are assumed to vanish or at least to be small compared to the induced position uncertainties from multiple scattering. To extend the fit into a region where this is not necessarily the case, one can include the effects of the hit uncertainties as additional contributions to the kink variances. The full kink variance is then

$$\sigma_{Kink}^2 = \theta_0^2 + \sigma_{Hit}^2/s^2, \quad (8.25)$$

where the θ_0^2 is the multiple scattering variance, σ_{Hit}^2 is the position variance in the curvilinear plane, and s is the propagation path between the hits.

8.4 TRIPLETS FIT

In order to move from a single triplet fit with three hits to a full track fit with an arbitrary number of hits, overlapping triplets are defined as shown in figure Figure 8.4. Instead of finding a local radius for each triplet, a global radius $\langle R \rangle$ needs to be determined that minimizes all triplets at once. The corresponding

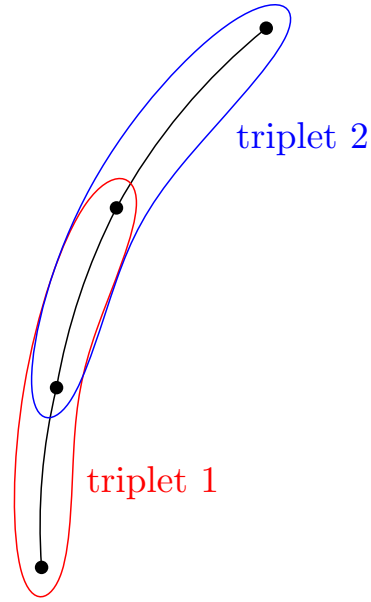


Figure 8.4: Full triplets trackfit construction scheme from overlapping triplets [75].

global objective function is the sum over the previously defined objective functions $S_i(R)$ from Equation 8.10 for each triplet.

$$\langle R \rangle = \arg \min_R \sum S_i(R) \quad (8.26)$$

Instead of following again an explicit minimization procedure for the global fit, the triplets can be fitted separately following the previous linearisation ansatz. The result is a fitted radius R_i and corresponding variance $\sigma_{R_i}^2$ for each triplet. The radius $\langle R \rangle$ that minimizes the global objective function (8.26) can then be calculated using a weighted average of the results from each triplet.

$$\langle R \rangle = \sum \frac{R_i}{\sigma_{R_i}^2} / \sum \frac{1}{\sigma_{R_i}^2} \quad (8.27)$$

Using the global radius $\langle R \rangle$, optimized scattering angles and local direction angles can be calculated for each hit position. In addition, the variance $\sigma_{\langle R \rangle}^2$ and the resulting full covariance matrix for all parameters can be easily derived from the global radius and the linearization ansatz for each triplet.

The solution for the global radius $\langle R \rangle$ in (8.27) was derived under the assumption that the fit variances $\sigma_{R_i}^2$ are constants, i.e. they are independent of the fitted radii R_i . However, this is not really the case. The fitted variances are calculated from

the kink variances which in turn are dominated by the multiple scattering variance. The multiple scattering variance is momentum dependent and we end up with

$$\sigma_{R_i} \sim \theta_{0,i} \sim \frac{1}{p_i} \sim \frac{1}{R_i} \quad (8.28)$$

which means that there is a dependency between fitted radius and variance. When using Equation 8.27, this correlation is ignored and the resulting global radius is biased.

Since the dependency is known, this problem can be easily solved by taking the dependency into account when solving Equation 8.26. The resulting expression for $\langle R \rangle$ takes on a similar form to the previous one, but includes additional counter terms to unbias the variance dependency.

$$\langle R \rangle = \frac{\sum \frac{R_i^2}{\sigma_{R_i}^2}}{\sum \frac{R_i}{\sigma_{R_i}^2}} \quad (8.29)$$

The corresponding variance for the global radius can be calculated using the updated averaging formula (8.29) and uncertainty propagation.

The triplets fit allows a fast direct fit of the global trajectory for the case of dominating multiple scattering effects. It achieves this by using only the local information from three hits without significant computational complexity. This is also beneficial for pattern recognition, where possible hit combination candidates can be fit with separate triplets. Matching triplets can be easily combined to larger trajectories.

8.5 GENERAL BROKEN LINES FIT

The general broken lines fit is an extended track refit developed by Volker Blobel and Claus Kleinwort [35, 56, 59], that takes uncertainties from both measurements and multiple scattering into account. It does so by linearizing the particle trajectory around a reference trajectory and fitting a local trajectory with corrections around the reference trajectory using a least square method.

The general procedure of the fit as used for this study is shown in Figure 8.5. Using a reference trajectory in the global coordinate system the track is linearized and only small parameter corrections with respect to the reference trajectory are considered for the fit. Along the reference track, parameter changes

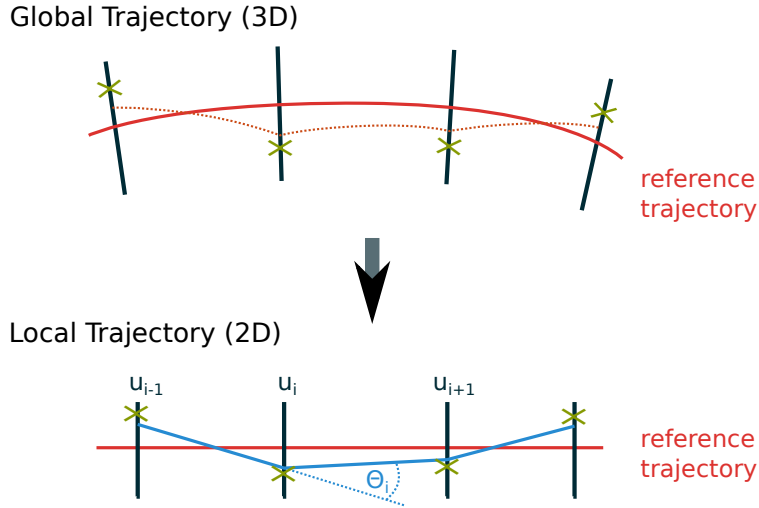


Figure 8.5: Global and local trajectory definition for the general broken lines fit.

at one point are propagated to a following point using the transport Jacobian F , i. e. $\mathbf{a}_{i+1} = F_i \mathbf{a}_i$ as defined in Chapter 7. The backward transformation, i. e. the propagation of changes at a given point to corresponding changes at a previous point, is given by the inverse of the corresponding forward Jacobian, i. e. $\mathbf{a}_{i-1} = F_{i-1}^{-1} \mathbf{a}_i$.

At each measurement and intersection with a possible scatterer, a local coordinate system is defined. For a consistent track model with the triplets fit discussed in Section 8.3 and Section 8.4, the measurement plane and the scattering plane are assumed to be identical. The local curvilinear plane anchored at the measurement point is used with the local offset $\mathbf{u} = (x_{\perp}, y_{\perp})$, local slope $\mathbf{u}' = (x'_{\perp}, y'_{\perp})$, and signed inverse momentum q/p as local corrections. The refitted local trajectory is defined by the offsets \mathbf{u}_i at each point on the trajectory and by a global correction to the signed inverse momentum $\Delta q/p$.

The measurement system, e. g. the local system on a planar pixel sensor, need not be identical with the local curvilinear system. The residuals to the measurements are then computed by projecting the offsets in the local system

$$\mathbf{r}_i = \mathbf{m}_i - H_{m,i} \mathbf{u}_i \quad (8.30)$$

where \mathbf{m}_i is the measured position in the measurement system and $H_{m,i}$ is the projection from the local system to the measurement system.

Scattering effects are taken into account by explicitly modeling them as kinks in the trajectory. They are calculated by examining the slope induced by offsets from neighboring points. The propagation Jacobian can be split up into separate components to calculate the offset change induced by parameter changes at a previous point.

$$\mathbf{u}_{i+1} = J_i \mathbf{u}_i + S_i \mathbf{u}'_i + \mathbf{d}_i \Delta q / p \quad (8.31)$$

For each triplet of adjacent points \mathbf{u}_{i-1} , \mathbf{u}_i , \mathbf{u}_{i+1} , the slope at the inner point can be calculated by inverting the propagation equation (8.31). This can be done twice, once using the forward propagation from the first point and once using the backward propagation from the last point (indicated by $-$ and $+$).

$$\mathbf{u}'_- = S_-^{-1} (\mathbf{u}_{i-1} - J_- \mathbf{u}_i - \mathbf{d}_i \Delta q / p) \quad (8.32)$$

$$\mathbf{u}'_+ = S_+^{-1} (\mathbf{u}_{i+1} - J_+ \mathbf{u}_i - \mathbf{d}_+ \Delta q / p) \quad (8.33)$$

Consequently, the kink at the inner point can be calculated as the slope difference before and after the inner point.

$$\mathbf{k}_i = \mathbf{u}'_+ - \mathbf{u}'_- \quad (8.34)$$

The local trajectory defined by the local offsets $\mathbf{u}_1, \dots, \hat{\mathbf{u}}_N$ and a global curvature correction $\Delta q / p$ is fitted by minimizing both the residuals and the possible kink angles. The expected multiple scattering angle is of course zero, but depending on the reference trajectory an initial kink value $\mathbf{k}_{i,0}$ can be present. The objective function is therefore

$$S = \sum_{i=1}^{i=N} \mathbf{r}_i^T \Sigma_{m,i}^{-1} \mathbf{r}_i + \sum_{i=2}^{i=N-1} (\mathbf{k}_{i,0} + \mathbf{k}_i)^T \Sigma_{k,i}^{-1} (\mathbf{k}_{i,0} + \mathbf{k}_i) \quad (8.35)$$

where $\Sigma_{m,i}$ and $\Sigma_{k,i}$ are the measurement and kink covariances. The measurement covariance is given e. g. by the pixel size in a pixel detector and the kink covariance can be calculated from multiple scattering theory.

Since the kinks depend only linearly on the offsets and on the global curvature correction $\Delta q / p$, the problem is now a purely linear least square problem and the optimized trajectory can

be found by solving the corresponding normal equations. Due to the construction of the local trajectory, the corresponding normal equations have a special form. They are band-diagonal with an additional fixed size dense edge, since only three neighboring offsets need to be considered for calculating a kink but all kinks depend on the global curvature correction. The special form allows a fast solution with a computational complexity of only $\mathcal{O}(n)$ [35].

With the fitted local offsets, corrections to all local parameters and corresponding covariance matrices at each point can be computed from the original propagation equations (8.32). Since the full covariance for the whole trajectory is readily available, possible alignment effects, i. e. changes to the orientation of the measurement planes, can be directly computed. This makes the general broken lines fit an excellent starting point for track-based alignment of tracking detectors. It was used e. g. for the CMS experiment tracker alignment [56].

Whether the general broken lines is a suitable track model depends on the validity of the underlying linearization, which in turn depends on the reference trajectory. Different reference trajectories may allow different approximations or result in different validity ranges.

8.6 OTHER METHODS

The three track fit methods described above are only a selection of the many methods that have been established over the last decades.

The single helix fit and the novel triplets fit are both fast initial fits. They can operate without additional information or a prior reference track and can be used either directly or as an initial step for a more detailed track fit. However, both fits assume a specific type of uncertainty to enable faster calculations. The general broken lines fit is an example for a detailed fit that requires additional reference information but allows an accurate treatment of both measurement and scattering uncertainties. All fits discussed so far are based on the least square formalism and are global or semi-global methods, i. e. all measurements that are expected to belong to a trajectory are required as an input.

The most prominent other track fit method is the Kalman filter [11]. It is a recursive linear filtering technique that was established by Billor, Frühwirth, and Regler [17, 18, 21] as a track fitting algorithm. It is an iterative procedure that incorporates one measurement at a time to continuously update the track parameter estimate. It works for arbitrary magnetic field configurations and can incorporate different kinds of uncertainties including multiple scattering and energy loss. It has been shown in [56, 59] that the general broken lines fit is mathematically identical to a Kalman filter with a reference trajectory and of similar computational complexity.

The Kalman filter is widely established and is currently used as the primary track fitting algorithm by many high energy physics experiments. One of its main features is its iterative nature that allows it to add additional measurement information without having to recompute previous steps. This is a big advantage in tracking detectors with a large number of measurements per track, e. g. for the ATLAS and CMS tracking systems, where tracks are reconstructed from an initial seed and then propagated to subsequent measurement layers where possible additional measurements can be selected. However, generating an initial helical seed already requires at least three positions. With only four available hits in the central tracker, the possible benefits from an iterative procedure for Mu3e square only minor.

A different aspect why the general broken lines fit is currently favoured for the Mu3e experiment is the aforementioned possible application for track-based alignment of the tracker. The general broken lines fit was specifically designed to facilitate track-based alignment. Its trajectory construction enables an easy way to calculate the effects from measurement changes due to (mis-)alignment on the whole trajectory.

8.7 IMPLEMENTATION

The helix and general broken lines algorithms are already established and are used in one way or another in currently running experiments. For these algorithms, there are existing implementations that are usually integrated into the reconstruction frameworks of the various experiments. The triplets fit is a novel algorithm that has no previous implementations.

I implemented all of the discussed fit algorithms and the necessary additional tools, e.g. track propagation, geometry calculations, uncertainty calculations, in a new tracking software package called *watson*. It provides minimal implementations designed for the requirements of the Mu3e experiment, but can also be used for other applications. A motivation and description of the *watson* tracking library can be found in Appendix B.

GENERAL COMPARISON

Before examining the specific performance of the different fits described in the previous chapter for the Mu3e experiment, I want to explore the overall behaviour of the algorithms in a more general context.

Instead of using the Mu3e configuration, which is dominated by multiple scattering effects only, I will use a generic detector geometry similar to a pixel detector at ATLAS or CMS. Depending on the momentum of the particles, tracking is either multiple scattering or hit resolution dominated. The performance of the different algorithms is compared with respect to their precision, possible bias, and description of parameter uncertainties.

9.1 SIMULATION SETUP

My main interest is the intrinsic behaviour of the different algorithms. To eliminate possible effects that could originate from the specifics of the detector geometry, an idealized detector setup is used.

The idealized detector geometry for the comparison is shown in Figure 9.1. The sensitive detector layers are assumed to have a cylindrical shape and to be aligned with the magnetic field direction. The inner radius is 40 mm and the outer radius is 360 mm with a total of six layers with equidistant spacing. This layout is motivated by the geometry of the barrel part of the current ATLAS pixel detector and its possible upgrades. The inner radius is given by the size of the beam pipe and the radius of the recently installed ATLAS Inner B-Layer [51] and the outer radius is given by the expected radius of the pixel-strip transition.

For simulating multiple scattering, each detector layer has an assumed thickness of 1.5% radiation lengths. This would correspond e. g. to 1.4 mm of pure silicon or less silicon and additional support structures. This is smaller than e. g. the current material budget of the ATLAS pixel tracker of approximately 2.5% radiation lengths per layer and in line with the planned

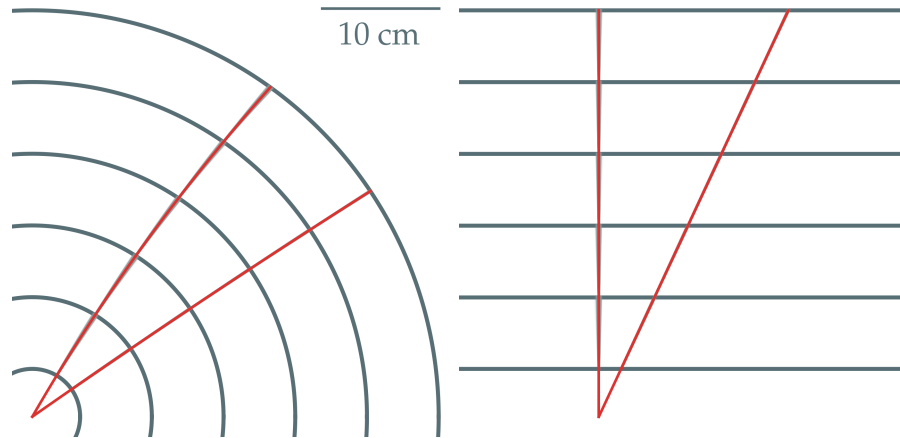


Figure 9.1: Idealized detector setup for a barrel-type pixel detector with six layers similar to e. g. possible upgrades of the ATLAS pixel detector. The left part shows the view in one quadrant of the xy -plane and the right part shows the corresponding area in the zr -projection. Two undisturbed example tracks with a momentum of $1\text{ GeV}/c$ (upper left) and $5\text{ GeV}/c$ (lower right) and the calculated propagation uncertainties due to scattering in each layer (tiny grey bands) are shown.

material budget for future upgrades. For the purpose of this comparison the exact composition is irrelevant and only the effective multiple scattering effects are of interest. The hit resolution along both directions along the barrel surface is assumed to originate from a square pixel size of $50\ \mu\text{m}$.

Particle tracks are generated at the center of the coordinate system as the nominal vertex position with a fixed charge. The absolute momentum p and the global track angles φ and λ are generated uniformly over the full accessible parameter space to scan the resolution. The tracks are propagated in a uniform magnetic field of 2 T according to the propagation equations discussed in Chapter 7 and Appendix A.

Multiple scattering is simulated assuming thin scatterers located at the detector layers. After propagation to the intersection with a detector layer, the global track angles are updated by drawing kink angles from a normal distribution with zero mean and a width calculated from multiple scattering theory as discussed in Section 7.4.2. Hit positions are simulated by smearing the nominal position at the intersections with noise drawn from a normal distribution with zero mean and a width corresponding to the simulated pixel size.

A layout with equidistant layers was simulated. A layout with double layers would be favored for multiple scattering dominated tracks due to the larger available propagation path that allows a better curvature measurement. It would also be better from a pattern recognition point of view. The short distance between the two elements of each double layer reduces the number of possible combinations that need to be considered when searching for a track.

However, the equidistant layout is much easier to understand since it only involves a single scale, i.e. the ratio of projected position uncertainty induced by multiple scattering and the single hit measurement uncertainty. It also coincides with the current ATLAS geometry.

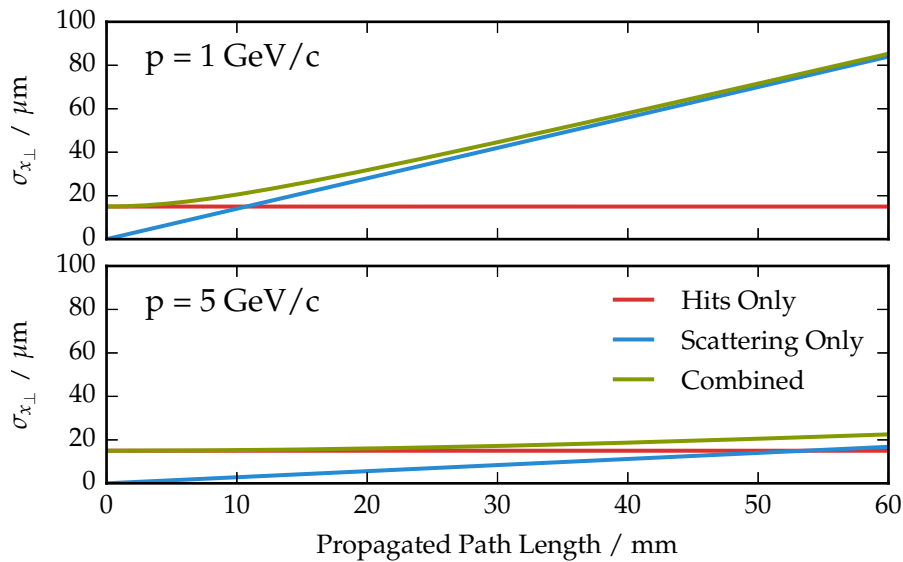


Figure 9.2: Propagated position uncertainty along a helical trajectory for 1 GeV/c and 5 GeV/c tracks after traversal of a simulated detector layer. The initial uncertainties at zero propagation length are due to hit uncertainties and multiple scattering. The initial uncertainty corresponds to the expected position and scattering uncertainties after traversing a layer of the idealized detector geometry.

The simulated momentum range is 1 GeV/c to 5 GeV/c. This range comprises both scattering and hit resolution dominated tracks. This is illustrated in Figure 9.2, where the propagated uncertainty of the curvilinear offset x_{\perp} after traversal of a simulated detector layer is shown for different momenta. The maximum propagation distance of 60 mm corresponds to the radial distance between two simulated detector layers. The

effects from the hit resolution stay constant along the track, whereas the propagated multiple scattering effects increase with the propagation distance. In combination with the momentum dependence, multiple scattering effects dominate the 1 GeV/c tracks, but are very small at 5 GeV/c tracks for the chosen geometry.

9.2 RECONSTRUCTION SETUP

The performance of the track fits is measured by comparing the reconstructed track parameters with the simulated true parameters. For a consistent comparison, all fitted parameters and their uncertainties are converted to curvilinear parameters. For tracking at the LHC, the reference position would usually be the nominal vertex position. This involves additional effects due to the propagation from the last measurement layer to the vertex, which might obscure the behaviour of the track fits. For the later comparison for the Mu3e geometry, no nominal vertex position exists. Instead, the vertices would be spread out over a large area and the propagation length from the inner-most layer to the nominal vertex would vary. For a consistent comparison, the inner-most simulated hit is used as a reference position.

When using the single helix or the triplets fit, the hit positions in the global Cartesian coordinate system are used as inputs. The general broken lines fit requires a reference trajectory to compute the local trajectory system and the relative orientation of the measurement system. At each hit position, the tangent plane to the cylinder surface is used to define a virtual measurement plane. The local trajectory point is defined at the intersection of the reference trajectory and the virtual measurement plane. This allows the computation of the projection from the local trajectory system to the measurement system using their relative rotation matrices.

The resulting parameter residuals are in general normally distributed, as expected from the simulation setup. The width of the distribution is a measure of the parameter resolution and the deviation of the distribution mean from zero is a measure for a possible bias. The sample standard deviation of the residual distribution, i. e. the square root of the distribution variance, is used to describe the width of the distribution and thus the resolution. Since possible non-Gaussian contributions to the

residuals would also affect the standard deviation, it is a conservative measure of the parameter resolution. If the fitted track model and the uncertainties are consistent, then the residual variances should be described by the fit uncertainties. The normalized residual distribution or pull, i. e. the residuals divided by the fit error, should follow a standard normal distribution.

9.3 TRIPLETS FIT

The triplets fit is a novel type of track fit that has only been recently put forward in [75, 80]. On the contrary, the single helix fit and its possible variations have been established as track fitting algorithms for many decades. It is imperative to closely examine the triplets fits' behaviour before comparing its performance to the other track fits discussed in Chapter 8. Here, I will investigate the differences between the possible variations of the triplets fit itself and discuss its general behaviour. Two possible types of variations exist: inclusion or omission of hit uncertainties as contributions to the kink variance at each triplet and the use of different averaging methods for the triplets combination.

The fit parameters of the triplets fit are the radius and the direction angles. The radius is the only global trajectory parameter, i. e. it is defined over the whole trajectory. The direction angles are defined locally, i. e. at a given hit position or with respect to a single triplet. Consequently, the parameters are affected differently when changing the triplets fit algorithm.

The effect on the reconstructed momentum¹ can be seen in Figure 9.3, where the resolution, bias, and pull is shown for different triplets fit variations. At low momenta all triplets fits yield consistent results, with no significant bias and a pull width of one. As seen in the top plot, the width of the relative residual distributions is not affected by different triplets fits, whether only the multiple scattering uncertainties (mean and counter) or also the hit uncertainties (counter with hit uncertainties) are considered. Only very minor differences can be seen above 4 GeV/c.

Deviations are visible for the fit bias and the pull distribution width in the bottom two plots. The triplets fit without hit uncertainties using a simple arithmetic mean to combine triplet radii has an increasing fit bias for higher momenta and an increas-

¹ Radius and absolute momentum differ only by a magnetic field factor.

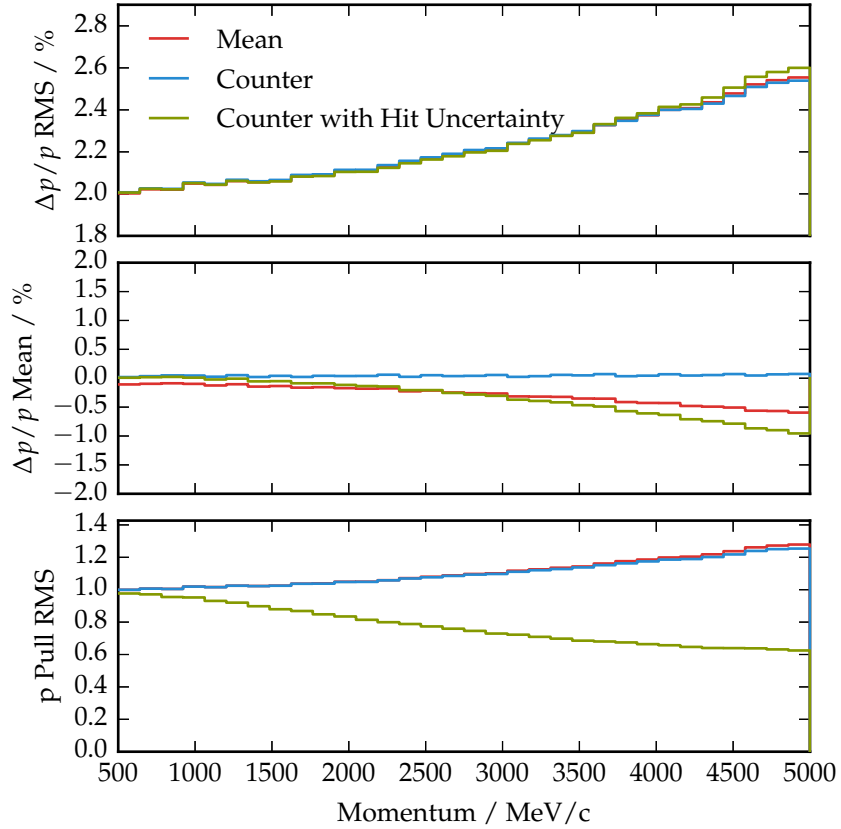


Figure 9.3: Absolute momentum fit performance using different triplets fit configurations for an ATLAS-like geometry. The triplets fit is performed using only multiple scattering uncertainties with (Counter) or without (Mean) a counter-term in the averaging procedure or including the hit uncertainties (Counter with Hit Uncertainty). From top to bottom: relative resolution, bias, normalized residuals (pull). Tracks with fixed dip angle of $\lambda = 20^\circ$ are used.

ing pull width above unity, i.e. it underestimates the momentum and the associated fit uncertainty. This is the result of two effects: first, the resulting radius weights are momentum dependent² and second, hit uncertainties contribute significantly at high momenta as shown in Figure 9.2. The first effect can be reduced by combining triplets using the averaging method with counter term. This removes the bias, but does not change the pull.

Introducing the hit uncertainties as additional contributions to the kink uncertainty normalizes the pull width for the direction angles. This will be discussed in detail in Section 9.5. How-

² As discussed in Section 8.4

ever, it introduces an additional bias for the momentum resolution at higher momenta where the hit uncertainties significantly contribute to the kink uncertainty. For a single triplet, the fit introduces an artificial kink due to position mismeasurement by changing radius. Since the triplets fit only considers three hits at a time, long range correlations due to the undisturbed helical propagation are effectively ignored and the global radius or momentum is underestimated. This can also be seen in the momentum pull width that is below one for this configuration. The momentum uncertainty is increasingly overestimated since the hit uncertainty contributes fully to each triplet without taking into account hit correlations between triplets.

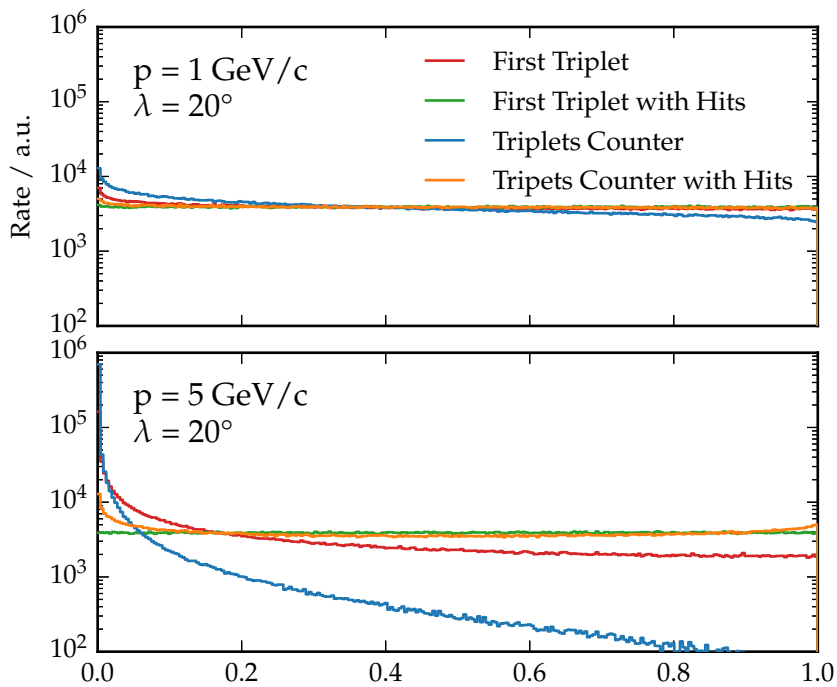


Figure 9.4: χ^2 probability distributions for different single triplet and triplets configurations. Both plots use a fixed momentum with 1 GeV/c (upper plot) and 5 GeV/c (lower plot).

The non-vanishing bias and the under- or overestimation of the fitted momentum uncertainty are a result of the triplets combination and not of inconsistencies in the separate triplets. Each triplet, when considered in isolation and including hit uncertainties, results in a consistent track description. Biases occur only when multiple triplets are stitched together into a combined trajectory.

This can be seen when considering the fit quality of the different fit variations is examined. With a consistent fit model, the value of the objective function for the fit result is distributed according to a χ^2 distribution and the distribution of resulting probabilities should be flat. The χ^2 probability distributions for different triplets fits using two different fixed momenta are shown in Figure 9.4. A flat distribution is only achieved when considering a single triplet¹ with hit uncertainties included. All other methods show significant deviations from a flat distribution. Using the triplets combination with counter term and including hit uncertainties yields the distribution closest to a flat one for the full trajectory fit. This is most prominent for the 5 GeV/c tracks where hit uncertainties are significant. The behaviour is reasonable because the triplets fit assumes negligible hit uncertainties.

¹ Here: the first triplet.

It should be noted that the discrepancies arise in a region where the tracks are not multiple scattering dominated anymore and have very low curvature. Thus, the initial assumptions of the triplets fit are not given. For consistency, I will use the triplets fit with hit uncertainties for the rest of this chapter.

9.4 GENERAL BROKEN LINES FIT REFERENCE TRAJECTORY

Since the general broken lines fit only considers small local changes along the track, it requires prior knowledge of the trajectory. Both the results from the single helix fit and the triplets fit can be used to provide such a reference trajectory.

In the case of the helix fit, the input trajectory contains large initial measurement residuals between the fitted helix and the hit positions but no initial kinks. The fit will then optimize the measurement residuals by introducing kinks in the local trajectory.

When using the triplets fit to provide the reference trajectory the situation is reversed. The input trajectory has vanishing measurement residuals by virtue of the triplets construction, but large initial kinks at all inner points. The fit will then reduce the initial kinks by introducing additional measurement residuals.

Ideally, the fit should converge to the same answer regardless of the input trajectory. The effects on the absolute momentum resolution and bias are shown in Figure 9.5. While the width of

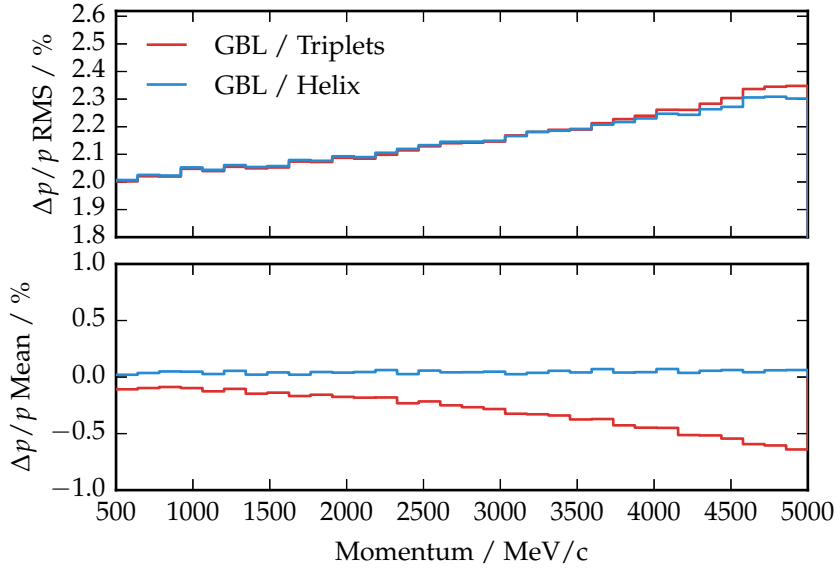


Figure 9.5: Momentum resolution and bias for the general broken lines fit using either the helix fit or the triplets fit with counter term and hit uncertainties as a reference trajectory.

the residual distribution shows no significant variation between the different input trajectories, there is a difference with respect to the fit bias. Using the triplets fit as a reference results in a momentum bias of up to 0.6 %. This is a remnant of the bias in the initial triplets trajectory discussed in the previous section; it cannot be completely eliminated, but is reduced compared to the maximum triplets fit bias of 1 %. One also needs to take into account that for the triplets fit with hit uncertainties, the initial kinks in the trajectory are likely to be overestimated. The general broken lines fit needs to amend both the initial momentum bias and the kink overestimation.

Both variants show a constant pull of 1 over the whole momentum range (pull distributions not shown). Other parameters besides the absolute momentum resolution are not affected by the bias and corresponding examples plots can be found in Appendix C. They will be discussed when comparing the different track fits in the following. In light of these results, the general broken lines will be shown with the helix fit as a reference trajectory for the rest of this chapter.

9.5 RESOLUTION

After discussing the variants of the triplets and general broken lines fits and choosing the respective relevant version, the resolution of the three different fit models — triplets fit, helix fit and general broken lines fit — can now be compared. The resolution of the absolute momentum and the two direction angles is shown in Figure 9.6 as a function of the momentum for tracks with a fixed dip angle. The dip angle is kept constant to reduce the spread of multiple scattering effects due to different effective material thicknesses.

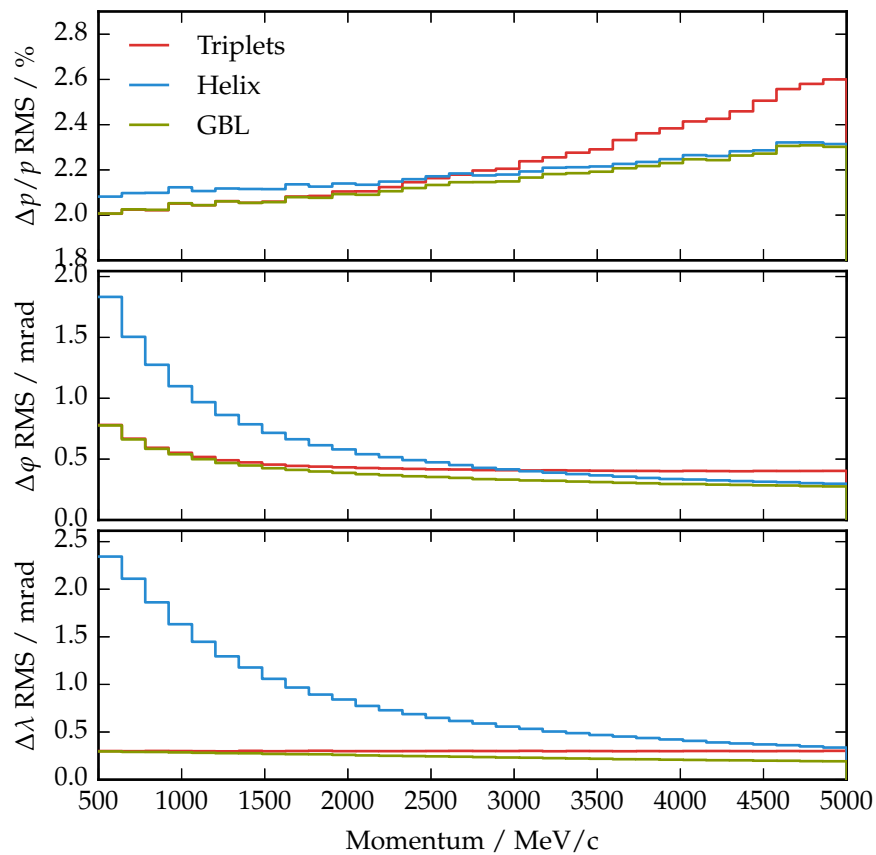


Figure 9.6: Momentum and angular resolution for the different track-fits over the simulated momentum range for a fixed dip angle of $\lambda = 20^\circ$

As expected, the general broken lines fit gives the best resolution over the whole momentum range since it takes into account all relevant sources of uncertainty in its track model. For lower momenta and dominating multiple scattering, the triplets

fit works almost as well as the general broken lines fit and provides virtually identical performance. The single helix fit shows a better resolution than the triplets fit at higher momentum and consequently dominating hit uncertainty and there is a clear crossover visible between the two regimes. For the (relative) momentum resolution the transition region lies around $2.5 \text{ GeV}/c$, for the azimuth angle resolution around $3 \text{ GeV}/c$, and for the dip angle only at about $5 \text{ GeV}/c$.

There are, however, qualitative differences in how the triplets and the single helix fit scale when they operate outside their designed uncertainty regimes. The helix fit has significantly higher deviation from the general broken lines fit, especially when looking at the global track angles.

The momentum scale where the transition occurs is a result of the chosen detector configuration and not intrinsic to the algorithms. Increasing the material budget increases multiple scattering and moves the transition to higher momenta. The same effect can be seen for increasing dip angles, i. e. more forward tracks, where the amount of material traversed by a track increases by a factor of $1/\cos \lambda$ and consequently multiple scattering becomes more important. Increasing the pixel size and reducing the detector resolution has the opposite effect, but the sensitivity for these changes are higher in the transverse plane than along the longitudinal direction.

In addition to the momentum and direction resolution, the position resolution at the inner hit must be considered. The resolution for the two curvilinear position parameters is shown in Figure 9.7. The general ordering among the different algorithms is similar to the momentum parameters described above, but the quantitative effects are different.

The triplets fit has a constant position resolution over the whole momentum range. Since the triplets fit does not consider position changes, the position resolution is fully determined by the detector resolution which is of course independent of the momentum. The difference in resolution between the two directions is due to the dip angle, i. e. the relative angle between the \hat{V} unit vector and the longitudinal measurement axis \hat{Z} of the measurement layer. The resulting position resolution is consistent with the pixel size and the orientation of the curvilinear plane with respect to the measurement sur-

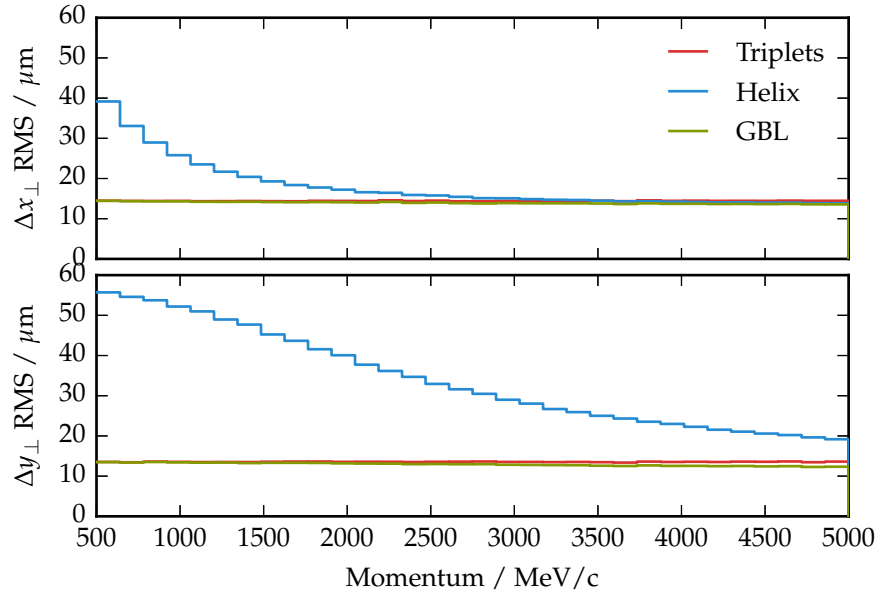


Figure 9.7: Position resolution for different trackfits over the simulated momentum range and a fixed dip angle of $\lambda = 20^\circ$.

face, i.e. $\sigma_{x_\perp} \approx 15 \mu\text{m} \approx 50/\sqrt{12} \mu\text{m}$ and $\sigma_{y_\perp} \approx 12 \mu\text{m} \approx 50/\sqrt{12}/\cos \lambda \mu\text{m}$.

The general broken lines fit resolution is also dominated by the detector resolution. Only at higher momenta can the fit take advantage of the additional measurements and improve the position resolution below the detector resolution. However, the effects are very small.

The helix fit has a significantly worse resolution than the other two algorithms when multiple scattering is dominating and the resolution improves with increasing momentum. Especially the longitudinal position resolution is always at least a factor of 1.5 less than the other fits. The helix fit result is influenced by all measurements and includes multiple scattering effects between all later measurements. Due to the split between the circular and linear fit (compare Section 8.2) for this single helix fit, possible correlations can not be taken into account.

9.6 BIAS AND PULLS

In addition to the resolution, an unbiased estimation and a correct uncertainty description are important performance metrics to characterize a fit algorithm. The fit bias for the momentum

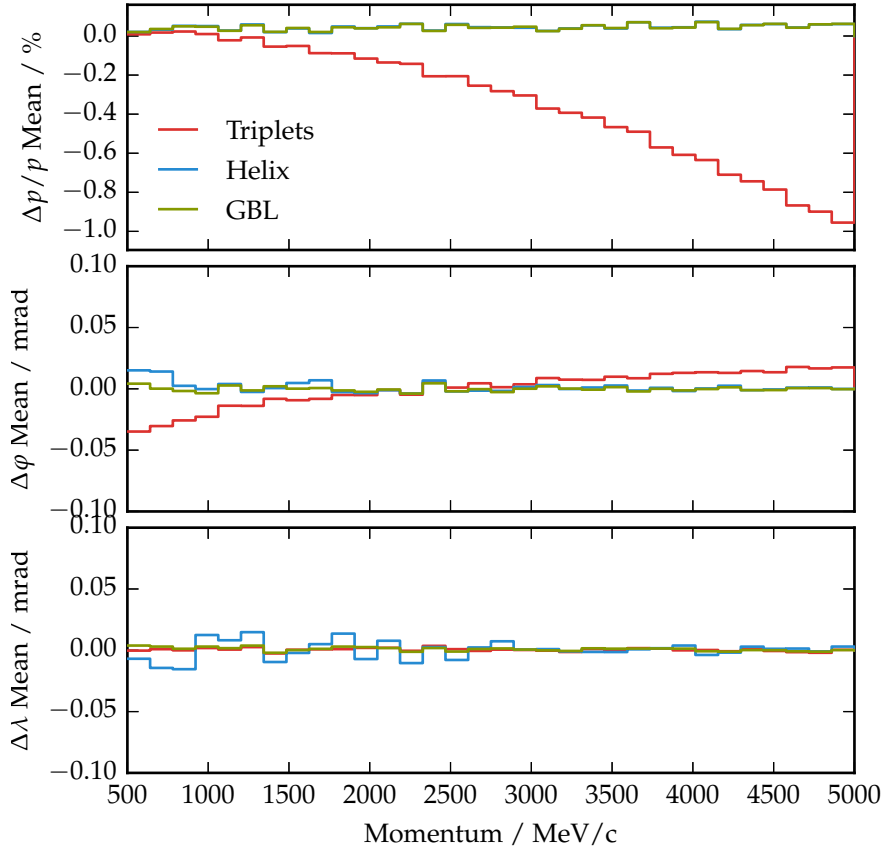


Figure 9.8: Mean value of the momentum and angles residual distribution for different track fits over the simulated momentum range.

parameters with different track fits is shown in Figure 9.8. Both the helix fit and the general broken lines fit are unbiased, i. e. they show no significant deviation of the mean of the residual distributions from zero. The absolute momentum bias of the triplets fit that was previously discussed in Section 9.3 can be clearly seen. There is a small bias visible for the azimuth angle ϕ result of the triplets fit. At a scale below 0.05 mrad it is an order of magnitude below the corresponding resolution of 0.5 mrad shown in Figure 9.6.

The results for the position parameters for all fit algorithms show no significant bias over the whole momentum range and can be found in Appendix C.

The width of the corresponding pull distributions are shown in Figure 9.9. The general broken lines fit provides a correct error description with a pull width of one for all parameters

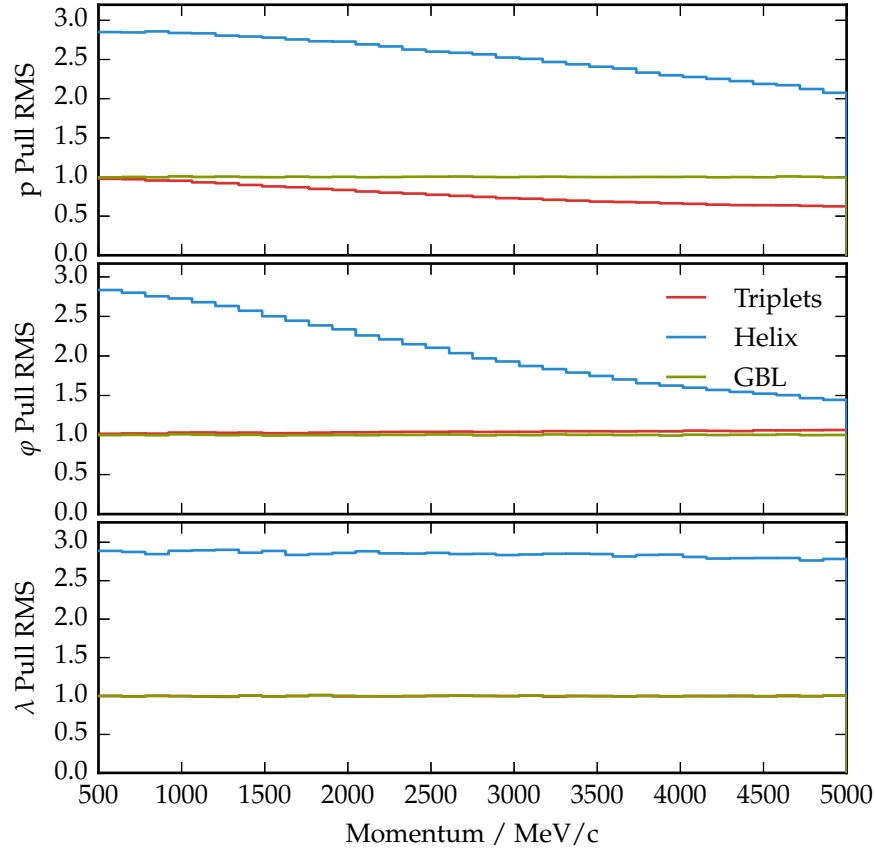


Figure 9.9: Pull widths for the momentum and angles residuals for different trackfits over the simulated momentum range. The triplets fit in the bottom plot is hidden by the general broken lines graph.

while the helix fit shows significant deviations. The triplets fit pull is one for the dip angle λ and shows only small deviations from one for the azimuth angle φ . The triplets pull for the absolute momentum exhibits the departure from a unit pull width previously discussed in Section 9.3. The good description of the triplet fit's uncertainties results from taking the hit uncertainties into account. Without them, the uncertainties would be underestimated and the pull width would be significantly above one. It shows that the triplets fit still gives a reasonable result for the track direction even in a region where hit uncertainties are a substantial contribution to the overall track uncertainties.

A similar picture emerges for the pull width with respect to the position resolution shown in Figure 9.10. Both general

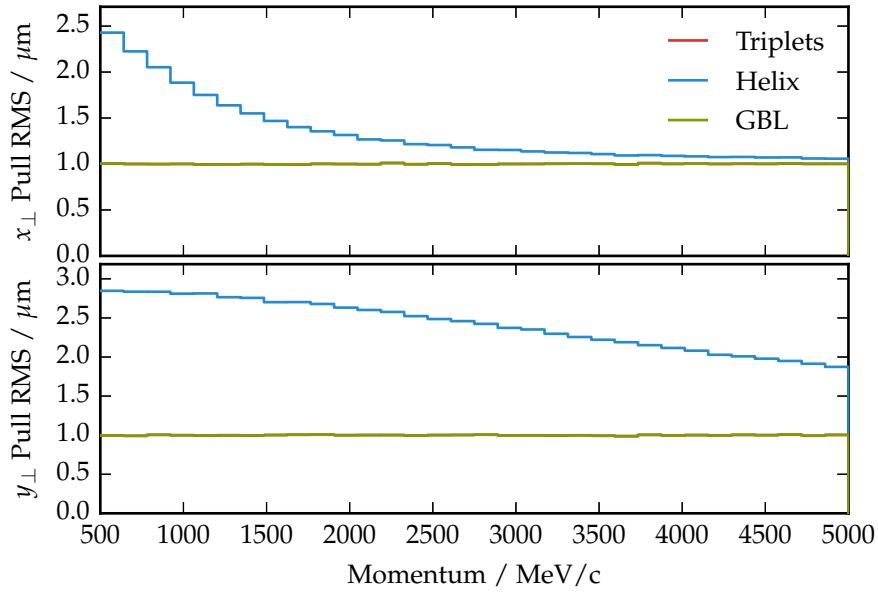


Figure 9.10: Pull distribution widths for the position residuals for different trackfits over the simulated momentum range. The triplets result is hidden by the general broken lines graph.

broken lines and triplets fit display an excellent description of the fit uncertainties with unity pull widths over the whole momentum range. For the triplets fit this follows directly from its construction, since the position resolution is fully determined by the hit resolution of the detector. The helix pulls decrease with increasing momentum and are again above unity, since the fit ignores multiple scattering effects and therefore underestimates the resulting fit uncertainties.

9.7 SUMMARY

For the ATLAS-like detector configuration, the general broken lines fit consistently yields the best results, both in terms of parameter resolution and by providing a consistent uncertainty description. This does not come as a surprise as it is the only fit that uses an extended track model where different uncertainties enter.

The single helix track fit as implemented here, is viable only at higher momenta and where hit uncertainties are dominant. It should be noted that the different track parameters show different behaviour. While the momentum resolution is competitive

already at lower momenta, the direction resolution is significantly worse. This is consistent with the fact that the curvature is a global parameter that is defined over the whole trajectory, while e. g. the direction angles are strongly influenced by local effects. Since the position uncertainty is the only considered uncertainty, the error description is inconsistent in the considered momentum range.

The triplets fit is designed for the opposite regime. It works well at low momenta where multiple scattering is dominating. When considering also the hit uncertainties, it yields a sufficient uncertainty description even in regions where multiple scattering is not the dominating source of errors. While the momentum estimate shows significant bias at higher momenta, the direction angles bias is still negligible.

PERFORMANCE FOR THE MU₃E EXPERIMENT

In the previous chapter, the behaviour of the different track fits was evaluated in settings that were either multiple scattering or hit uncertainty limited. This was done using a simplified detector geometry typical for a collider experiment such as the ATLAS barrel pixel detector.

In this chapter, I compare the performance of the different track fits specifically for the Mu₃e detector geometry. In contrast to the previous chapter, this setup is multiple scattering dominated over the whole parameter range even though the material budget per layer is only 0.1 % radiation length. In addition, all tracks have a large curvature. To accommodate the unique Mu₃e detector setup described in Chapter 3, two different situations need to be considered: the case where only short tracks in the central detector are reconstructed and the case where long recurling tracks that return back to the outer layers are examined. The former case is related for online reconstruction while the latter is related to the full offline analysis.

10.1 SIMULATION SETUP

The general simulation procedure and its implementation is identical to the system previously described in Section 9.1. Differences are the result of the change in detector geometry and material budget. Four layers of cylindrical sensors are simulated with radii of 22 mm, 28 mm, 70 mm and 78 mm. The values are consistent with the mean layer radii of the central Mu₃e pixel tracker discussed in Chapter 3. Multiple scattering at each layer was simulated with a thickness of 0.1 % radiation lengths. The hit resolution was simulated by Gaussian smearing equivalent to a square pixel geometry with a pixel pitch of 80 μm.

Single tracks are again generated at the center of the coordinate system with in the allowed momentum range of 15 MeV/c to 55 MeV/c with a fixed charge and a fixed dip angle. They are propagated in a constant magnetic field of 1 T along a full turn, i.e. until they have curled back in the magnetic field and

have been measured again in the outer layers. Tracks that do not reach the fourth layer, e.g. due to low transverse momentum, are not considered. For the selected tracks either the short part with four hits in the central detector or the full tracks are fitted.

In the experiment the tracks vertices would be distributed over the target area and would only very rarely originate from the origin. However, this mostly affects the propagation distance from the innermost hit back to the vertex and not the reconstruction in the detector.

10.2 SHORT TRACKS

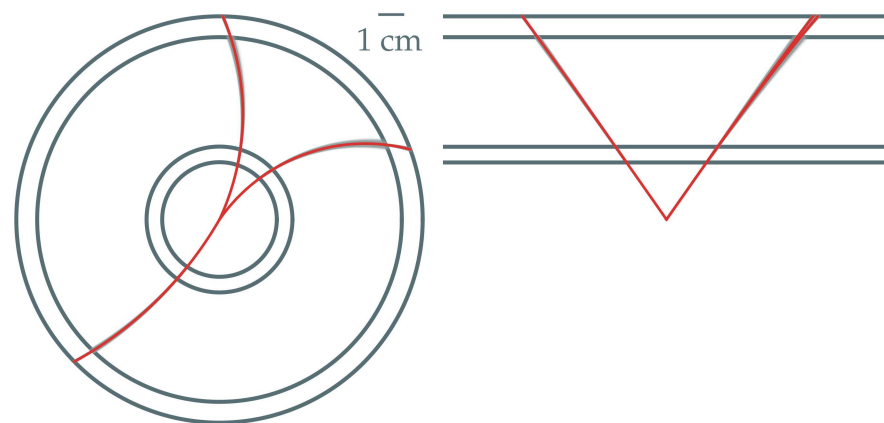


Figure 10.1: Idealized simulation setup for the central Mu3e tracker with three tracks from a signal decay including only the outgoing part of the trajectory. The red path shows the idealized trajectory and the grey bands indicate the multiple scattering induced along the path. The left part shows the projection in the xy -plane and the right part shows the tracks in the zr -projection.

A example signal event with three decay electrons can be seen in Figure 10.1 where the uncertainty induced by multiple scattering is shown as grey bands. The lower left track has the maximum momentum of $53 \text{ MeV}/c$. For the Mu3e setup, multiple scattering is clearly the dominating effect; even for the highest momentum track, the uncertainty induced by multiple scattering is significant and visible in the global system. In contrast to the previous generic setup discussed in Chapter 9, all tracks have a large curvature.

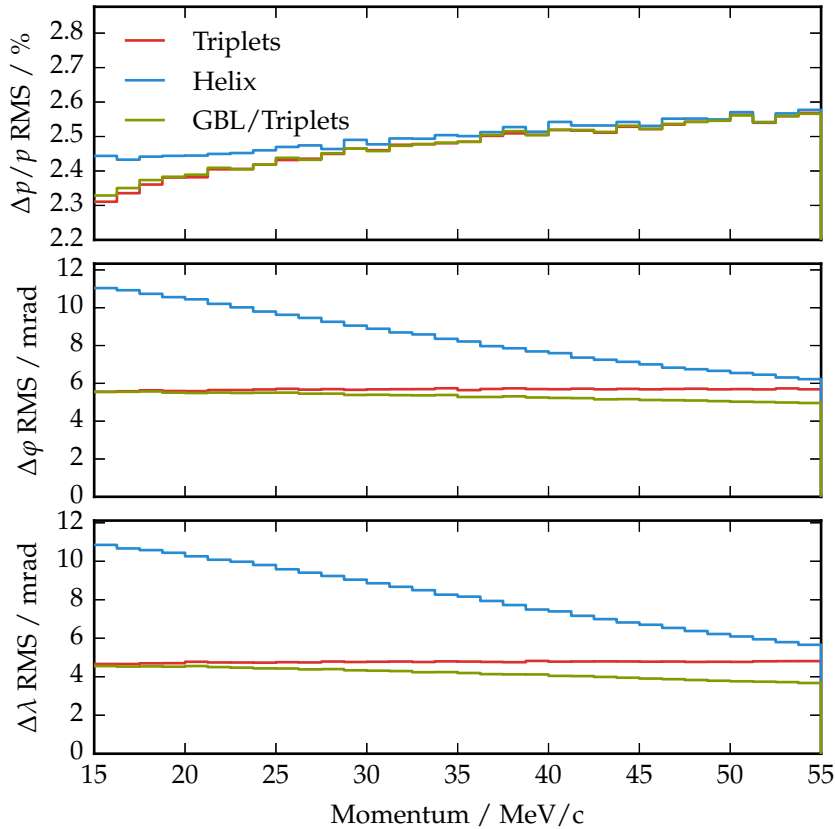


Figure 10.2: Momentum parameters resolution for different algorithms for short tracks with four hits in the central detector. The dip angles λ is fixed at 20° .

The momentum resolution for a sample configuration with a fixed dip angle of 20° is shown in Figure 10.2. For the outgoing tracks the results look similar to the low momentum limit of the general comparison discussed in the previous chapter. The general broken lines fit provides the best performance over the whole momentum range. The triplets fit shows identical performance for lower momenta with a very small change at higher momenta compared to the general broken lines fit. The helix fit is consistently worse than all other algorithms. However, the differences effect only the global track angles and not the absolute momentum resolution.

At higher momenta above $35 \text{ MeV}/c$ all algorithms show the same relative momentum resolution. Due to the detector geometry the propagation length is short compared to the trajectory radius.¹ A possible curvature of the track has very little effect

¹ Corresponding to a small propagation angle

for the short distances inside each double layer and the momentum is almost completely determined by the longer propagation between the two double layers.

The resolution of the global track angles at the inner-most hit position is dominated not by multiple scattering, but by the pixel size as a result of the short propagation distance. Both the triplets fit and the general broken lines fit only use the local information to determine its value and are not affected by the multiple scattering at later positions. Consequently, the resulting resolution is constant for the triplets fit and almost constant for the general broken lines fit over the full momentum range. The small resolution at higher momenta means that the general broken lines fit can use additional information from later positions to constrain the direction if the uncertainties allow it. This is not true for the helix fit, where the track angles are influenced by uncertainties at all measurement positions and have a diminished resolution compared to the other fits.

In contrast to the previous chapter, the resolution for the general broken lines fit shown in Figure 10.2 uses the triplets fit as a reference trajectory. When considering only the short tracks, the choice of reference trajectory¹ has little effect on the general broken lines fit result. However, this will change when considering long recurling tracks. Since the Mu3e experiment also intends to use the triplets track fit as a fast online track fit, it is here chosen as the reference trajectory. All fits show no significant bias over the whole momentum range (compare figures in Appendix C).

¹ *Single Helix or Triplets.*

The pull distributions for the momentum parameters are shown in Figure 10.3. Again as expected, the triplets fit and the general broken lines fit give a good error description with consistent pull values of one over the whole momentum range. The helix fit significantly underestimates the parameter errors since it does not include multiple scattering effects.

When considering outgoing tracks in the Mu3e geometry, both the triplets fit and the general broken lines fit can reconstruct the trajectory with comparable resolution and a correct description of the associated uncertainties. Small improvements are possible for the global track angles when using the general broken lines fit, but at the expense of a computational complexity. The behaviour of the position resolution is identical to the

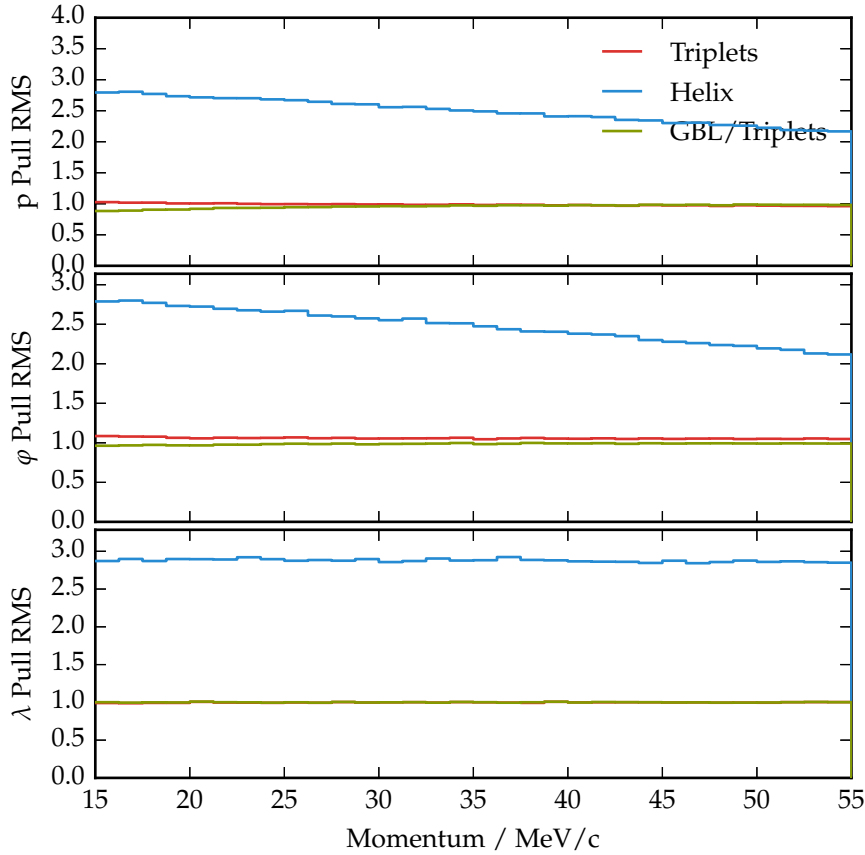


Figure 10.3: Momentum parameters pull distribution widths for different algorithms for short tracks with four hits in the central detector. The dip angle λ is fixed at 20° .

behaviour for the global track angles and can be found in Appendix C.

Although all resolutions have been shown for a fixed dip angle, the behaviour does not change qualitatively when the dip angle is changed. A higher dip angle increases the effective layer thickness traversed by the track by a factor of $1/\cos\lambda$. This means that the multiple scattering effects increase by a factor of $1/\sqrt{\cos\lambda}$ as discussed in Section 7.4.2. Conversely, the effective hit resolution also scales down by the same factor of $1/\cos\lambda$ due to the projection from the cylinder surfaces to the curvilinear plane. With a maximum dip angle acceptance of 60° , the possible changes are of the order of $1/2$. This shifts the resolution curves to higher momenta but does not change the overall picture.

10.3 LONG TRACKS

For long, recurling tracks the geometry stays the same, but tracks are propagated through the magnetic field back to the outer layers after they have passed the central detector. They are called recurlers, since they curl back to the detector. Depending on the momentum along the magnetic field axis, i. e. $p_l \sim \sin \lambda$, they return either back to the central detector or to one of the upstream and downstream stations, the so-called re-curl stations. In the real detector geometry, the re-curl stations are separate detectors at the same radii as the outer layers of the central detector but separated by a gap along the beam axis. However, this only affects the geometric acceptance and not the parameter resolution itself. In the idealized geometry, the re-curl stations are simulated by extending the outer layers of the central detector without a separating gap.

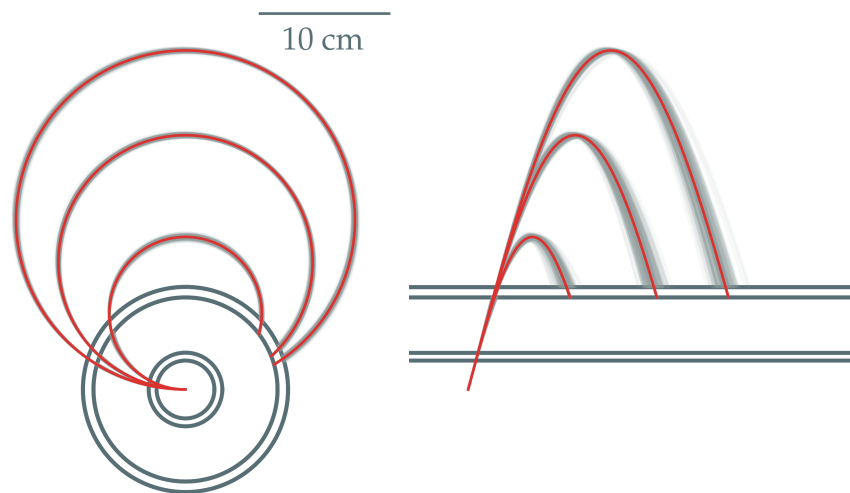


Figure 10.4: Idealized simulation setup for the Mu3e tracker including long recurling tracks. Three tracks with momenta of 18 GeV/c, 30 GeV/c and 40 GeV/c and an dip angles of 15° are shown. The grey bands are generated from additional tracks with scattered direction angles according to the expected multiple scattering distribution at the previous layer. The arrows mark the half-circle propagation. The left part shows the xy-projection and the right part show the zr-projection.

Example trajectories for long, recurling tracks and the associated uncertainties due to multiple scattering are shown in Figure 10.4. The overall trajectory setup is now quite different from

all previous setups. The longest part of the particle trajectory is the free propagation in the magnetic field and the trajectory traverses the tracker only at the beginning and at the end.

The long propagation path entails that tracks with a sufficiently large transverse radius perform more than a half-circle turn in the magnetic field. This circular path means that, unlike for the ATLAS-like and the central Mu3e detector, multiple scattering effects influence the transverse and the longitudinal uncertainties differently. A half-circle track will traverse the same position when it returns, regardless of initial direction changes, and the offset uncertainties induced by multiple scattering vanish. In principle this is only exactly true for transverse tracks, but the effect can also be seen for the example trajectories in Figure 10.4. The grey bands that visualize the scattering uncertainties grow along the trajectory until a quarter turn, i. e. a propagation angle of $\pi/2$, is reached and decreases to become minimal for a propagation angle of π .

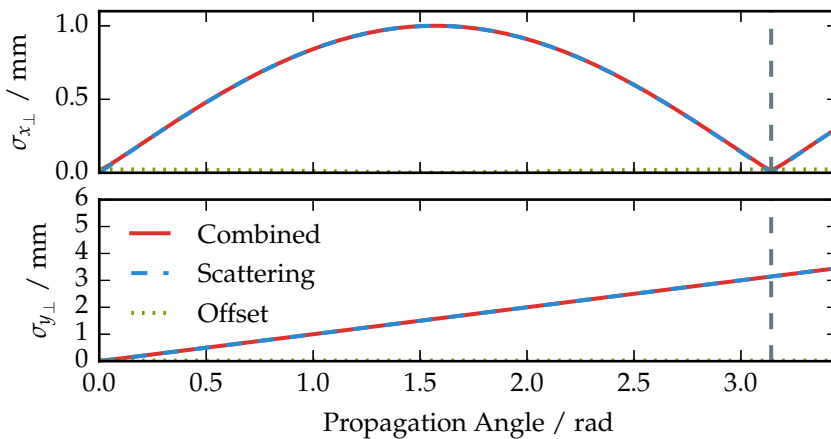


Figure 10.5: Propagated offset uncertainty along the two curvilinear offset directions as a function of the propagation angle. The uncertainties are shown for a 30 MeV/c track with vanishing dip angle $\lambda = 0^\circ$. The initial uncertainties are equivalent to the uncertainties after traversing a single Mu3e detector layer. The offset uncertainty (dotted green line) is around $30\ \mu\text{m}$ and therefore only barely visible.

The expected uncertainty along the trajectory path is shown in Figure 10.5 for a track with a vanishing dip angle. It is immediately clear that uncertainties are dominated by multiple scattering effects since the hit uncertainty contributions are barely

visible. The transverse offset uncertainty vanishes at a propagation angle of π . The longitudinal uncertainty shows no such behavior and increases linearly with the propagation angle.

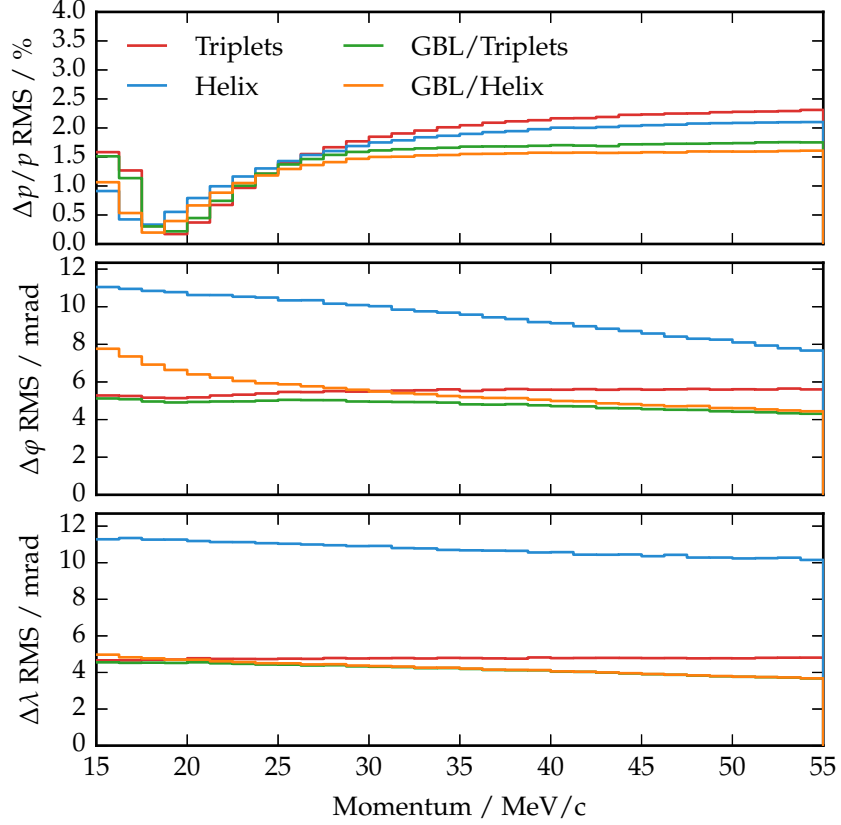


Figure 10.6: Momentum parameters resolution for the different track-fits over the simulated momentum range using long tracks with six hits and a fixed dip angle of $\lambda = 20^\circ$. The two general broken lines fit result in the same λ resolution; the green line is hidden.

This results in an unfamiliar behaviour of the resulting fit resolution as shown in Figure 10.6 for the different algorithms. Overall the momentum resolution is significantly improved compared to the previous case where only the outgoing trajectories in the central detector were considered as a result of the large propagation length. The worst-case momentum resolution of the general broken lines fit is 1.6% compared to the best resolution of 2.3% for short tracks.

All track fits show a similar general behaviour with respect to the momentum resolution. For high momentum above 30 GeV/c, the resolution is constant or almost constant. For

lower momenta, the resolution rapidly improves to reach a momentum resolution of 0.2 % around 18 GeV/c.

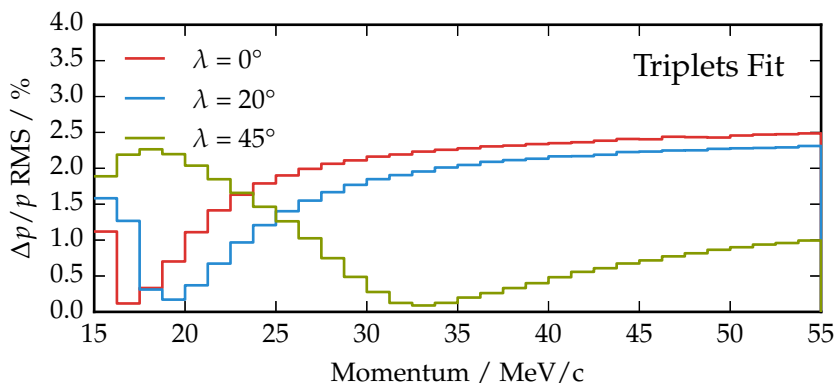


Figure 10.7: Relative momentum resolution for the triplets fit over the simulated momentum range for long tracks with six hits and different fixed dip angles.

The optimal resolution results from the previously described geometrical effect, where the projected track circle in the transverse plane is equivalent to a half-turn with a propagation angle of π . This corresponds to the case of lowest momentum tracks in Figure 10.4. At this point, scattering in the last layer has almost no influence on the expected propagated position in the transverse plane and the resolution is determined only by pixel resolution. This is of course dependent not only on the momentum but also on the dip angle λ . The optimal resolution point increases with the dip angle since the larger dip angle must be offset by a larger momentum to result in the same transverse radius. Figure 10.7, where the momentum resolution of the triplets fit is shown for different fixed values of the simulated λ angle. Since the Mu3e track directions are almost isotropic, the average resolution over the full phase space is greatly reduced.

While the momentum resolution is significantly changed, the resolution of the angular parameters is comparable to the previous section where only the tracks in the central detector were considered. The angular resolution of the triplets fit remains almost constant at 5 mrad over the momentum range, while the general broken lines fit can improve slightly for larger momenta. While the large free propagation path of the track allows a refined measurement of the track momentum, a global

parameter, the direction resolution is still determined by the local effects at the inner-most hit.

For the short tracks in the central detector, the choice of reference trajectory had no influence of the general broken lines result. This is no longer the case for the long tracks, where clear differences between the general broken lines fits are visible. With the single helix reference, the initial trajectory is a good approximation along the long free path and the absolute momentum estimate is sufficient. Using the helix fit as a reference results in a better momentum resolution. However, the single helix trajectory deviates further from the measured points at the inner layer. The initial direction estimate deviates and the linearized correction from the general broken lines fit can not compensate the initial difference. As a result, the angular resolution is better when using the triplets fit as reference.

For momenta below $18 \text{ MeV}/c$, i. e. where the tracks propagate less than a half-turn, the helix fit momentum resolution is slightly better than the triplets resolution. At these low momenta, the tracks have a very high incidence angle on the detector surfaces. The estimated multiple scattering variances are very sensitive to the track direction since small direction changes lead to changes of the effective path length in the scattering medium. This influences the triplets fit and not the helix fit since it only considers position uncertainties. The behaviour of the reference triplets also affects the subsequent general broken lines fit.

The main difficulty for the general broken lines fit is the linearized propagation along the large helix. To visualize the challenge, the propagated curvilinear offset along the helix trajectory is shown in Figure 10.8. This shows how changes of the direction and momentum at an initial position propagate along the reference trajectory. Already small changes lead to position changes of the order of 2 mm to 3 mm, large compared to the pixel size of $80 \mu\text{m}$. With these large changes, the initial assumption of small changes around a reference trajectory, are not necessarily satisfied. The linearized local trajectory around the reference is valid only for a very small region of possible parameter changes. This can be seen e.g. in the fact that the final general broken lines result depends on the reference trajectory. For larger momenta, the difference in momentum resolution between the two general broken line fits corresponds roughly

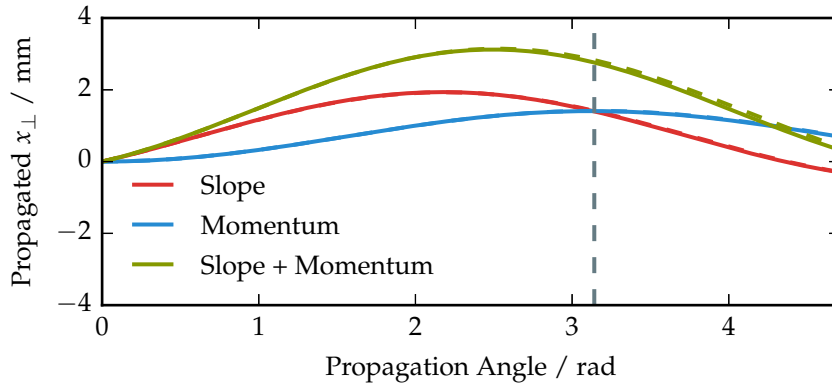


Figure 10.8: Propagated curvilinear offset x_{\perp} for a 30 MeV/c track with a dip angle of $\lambda = 45^{\circ}$. The initial curvilinear slope change is 10 mrad and the relative initial momentum change is 1%. The initial changes are propagated using the helix propagator (solid line) and the corresponding helix Jacobian (dashed line).

to the difference in resolution between the reference trajectories. If the linearization would be sufficient, the two separate fits should converge. However, in both cases the general broken lines fit is still able to achieve a modest improvement in resolution.

Possible fit biases are small compared to the resolution and are shown in Figure 10.9. The lambda bias for the helix fit is due to the separation into circle and linear fit. The circle fit in the transverse plane benefits from the half-turn effects but possible correlations with the longitudinal fit including the λ determination are ignored.

A correct description of the fit uncertainties requires a correct track model. As discussed previously for the resolution result, this is probably not the case when using the general broken lines fit to reconstruct the long tracks. This can also be seen when considering the momentum parameter pull widths shown in Figure 10.10. The track angles are well described by both the triplets fit and the general broken lines fit when using the triplets fit as a reference. The deviation of the general broken lines fit with helix reference at low momenta coincides with the lower resolution shown in Figure 10.6. Here, the helix reference is not a good linearization point at the inner-most hit position.

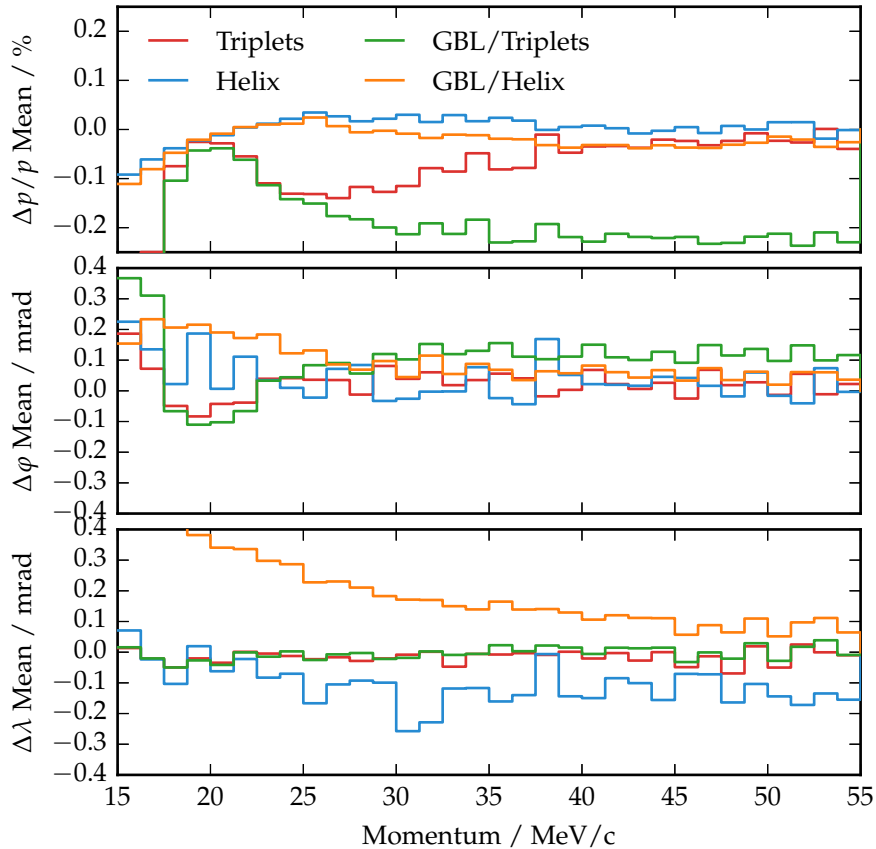


Figure 10.9: Fit bias for the momentum parameters and different trackfits over the simulated momentum range for long tracks with six hits. The dip angle is fixed at $\lambda = 20^\circ$.

Only the triplets fit gives a reasonable momentum pull width close to unity. It is not as good as for the short tracks shown in Figure 10.3. It should be noted that the triplets fit is also linearized. The half-circle configuration could be a situation where this ansatz has only a limited validity range. The general broken lines fit shows a pull width around two. This is consistent with a break down of the linearization, where the linearized local trajectory underestimates the parameter changes and consequently underestimates the fit uncertainty. All track fits variate at the half-turn configuration, where the largest non-linearities are expected. It is clear that this configuration with long recurring paths remains challenging for all evaluated algorithms.

Due to the large effects from multiple scattering, the position resolution is essentially determined by the hit resolution at the detector layer, i.e. the inner-most layer for this case. It is not

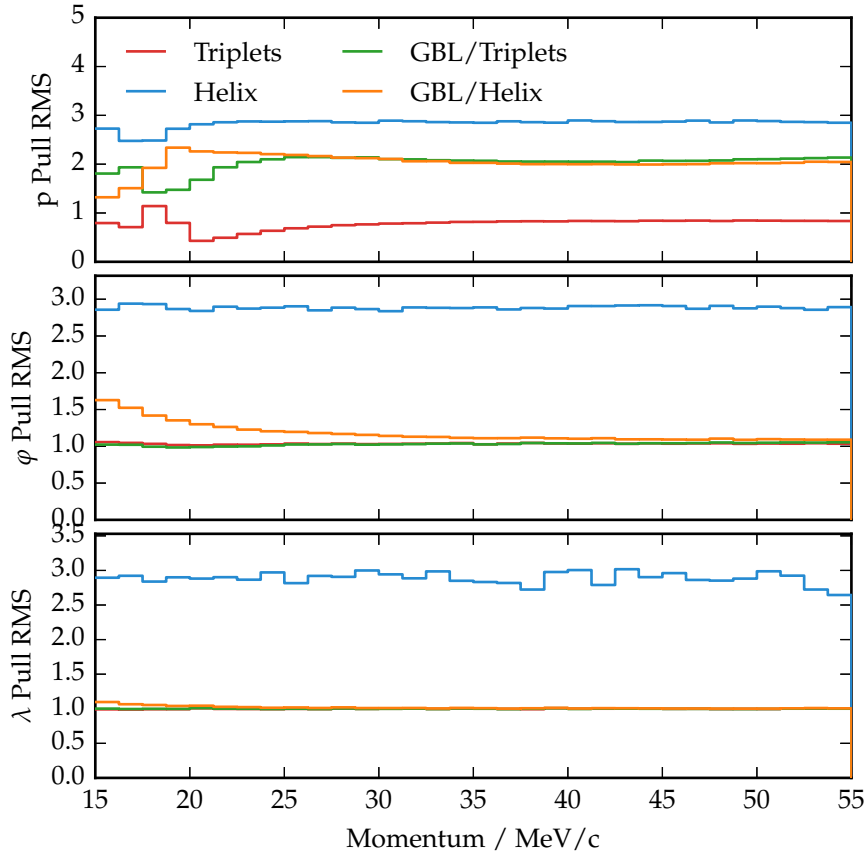


Figure 10.10: Width of the pull distributions for the momentum parameters using different trackfits as a function of the momentum for long tracks with six hits. The dip angle is fixed at $\lambda = 20^\circ$.

affected by the large propagation paths of the recurling tracks further along the trajectory. This can be seen in Figure 10.11 where the position resolution at the inner-most hit is shown for all algorithms. The triplets fit shows the expected constant resolution over the whole momentum range that is consistent with the pixel pitch $\sigma_{x_\perp} \approx 23 \mu\text{m} \approx 80/\sqrt{12} \mu\text{m}$. Corrections to the curvature or to the track directions play only a limited role for the inner-most position and consequently the general broken lines fit displays only very little improvement. Since only the local information is relevant, the general broken lines result is also independent of its reference trajectory. The helix position resolution is severely limited with an up to four times decrease compared to the triplets and general broken lines fit. The uncertainties are again well described by all algorithms except the

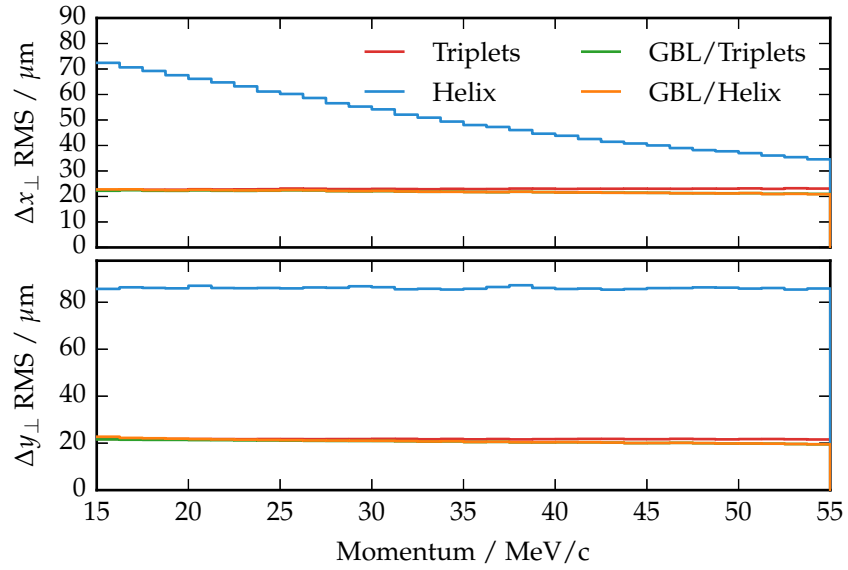


Figure 10.11: Position resolution for the different trackfits for long tracks with six hits and a fixed dip angle of $\lambda = 20^\circ$. The triplets and general broken lines resolutions are almost identical.

helix fit and the corresponding pull width plot can be found in Appendix C.

10.4 CONCLUSIONS

The Mu3e detector uses a distinct tracking setup that opens up previously unexplored challenges for track reconstruction. Large curvatures, dominant multiple scattering uncertainties and recurling tracks with long propagation paths are the problems that need to be solved.

I investigated three different fit algorithms, in order to determine their viability for track reconstruction with the Mu3e experiment.

The novel triplets fit works well, both for short and for long recurling tracks. While it is based on a simplified track model that assumes negligible position uncertainties, it provides a parameter resolution that is comparable or even on-par to the extended general broken lines fit. In addition, it provides a good error description even for the case of long, recurling tracks. It is excellently suited for the Mu3e experiment and is foreseen to be used for the fast online track reconstruction.

The single helix fit yields only mediocre resolution in the relevant regimes and is not a good option for multiple scattering dominated track fitting.

The general broken lines fit is an extended track fit that models both hit uncertainties and multiple scattering. It achieves the highest resolution for both short and long tracks and can improve the momentum resolution by up to 20% compared to the triplets fit. However, problems occur with the error description for recurlers, due to the large propagation length and possible non-linearities. While there are areas of possible improvements, the general broken lines fit is a good candidate for precise offline reconstruction.

Using long, recurling tracks allows for a significant enhancement in momentum resolution. Yet, the possible non-linearities due to the large propagation length can not be easily avoided and render a consistent error description challenging. Additional effort is required to fully understand this problem. It will be interesting to see if and how other advanced track fits, e. g. a Kalman filter, would perform at the same task.

SUMMARY, CONCLUSION, AND OUTLOOK

The Mu3e experiment is a precision experiment searching for the charged lepton flavour violating decay $\mu^+ \rightarrow e^+e^-e^+$. It is theoretically allowed in the Standard Model via neutrino mixing in loop diagrams, but it is suppressed far beyond any experimentally accessible branching ratios. Any measurement of the $\mu^+ \rightarrow e^+e^-e^+$ process is thus a clear indicator for new physics.

The Mu3e experiment aims for a sensitivity of better than 1 in 10^{16} decays. This requires a large number of decays of low energy muons to be reconstructed. In order to separate the expected signal and possible backgrounds, an excellent resolution with respect to momentum, vertex position, and timing is required. A novel detector technology, high voltage monolithic active pixel sensors (HV-MAPS), shall enable a low-mass tracker with high-rate capabilities. Besides, algorithms for fast online reconstruction to filter events of interest as well as precise offline analysis are essential for the success of the project.

In this work, I investigated the characteristics of small-scale prototype sensors — the first HV-CMOS chips with fast digital readout — in test beam measurements. In addition, I implemented three types of tracking algorithms, compared their performance and tested the suitability for the Mu3e tracker geometry.

11.1 PIXEL SENSOR PROTOTYPES

To reach the projected sensitivity, a high number of decay electrons need to be reconstructed. This in turn requires a high particle rate to acquire the necessary statistics in reasonable time. A highly segmented detector is needed to handle the expected occupancies. Silicon pixel sensors can provide the necessary position resolution and timing.

The low momentum of the decay electrons results in tracking uncertainties that are dominated by multiple scattering effects. Existing hybrid pixel sensors have a material budget that is too large for the Mu3e experiment. High voltage monolithic active

pixel sensors are a novel sensor technology that enables fast and thin tracking detectors.

This work reports on the first extensive test beam measurements with high voltage monolithic active pixel sensor prototypes. After the integration of the existing MuPix readout system into the EUDET telescope setup, data was taken at the DESY testbeam facilities. Postprocessing involved telescope track reconstruction, telescope alignment, and subsequent matching of reconstructed tracks to possible hits of the MuPix sensor. Measurement evaluation was successful despite an unwanted strixel feature of the MuPix4 prototype. The sensor showed very little clustering consistent with a thin active depletion zone and the large pixel pitch. The position resolution was consistent with the pixel pitch.

The pixel sensor efficiency depends on the applied bias voltage and threshold and efficiencies above 99% were reached. The sensor prototype responded to variations in threshold and bias voltage as expected. The efficiency plateau was not visible due to readout problems, as few noisy pixels limited lowering of the threshold. The few noisy pixels could not be reduced further with the given hardware setup at the early stage of sensor development. Unfortunately, the telescope trigger and readout scheme prevented corresponding noise measurements. However, several tests in the laboratory showed a sufficient signal-over-noise ratio.

This first in depth characterization of HV-MAPS prototypes using test beam data strongly suggests that they can provide the technology required for a successful Mu3e experiment. In the mean time, updated prototypes with modifications of the analog part (MuPix6) and a full integration of the digital readout including a fast serializer (MuPix7), became available. They have recently been subjected to intense beams and were combined with high-rate readout. The different analog and digital circuits of the MuPix chips can be configured and a large ongoing effort is to find the optimal tuning. The tuning effects the noise level, signal speed, or the overall power consumption. For the Mu3e experiment, a low power consumption is advantageous to allow cooling with gaseous helium to retain the minimal material budget. The next step for the Mu3e experiment is a full-scale sensor prototype. A sensor size of $13\text{ mm} \times 20\text{ mm}$

is planned that will be used to build a first working prototype of the whole detector.

Overall, HV-MAPS proved to be a promising new technology. The integrated construction, low material budget, and full digital readout are features that are of interest to many other experiments besides Mu3e. It is investigated as an upgrade option e.g. for the ATLAS experiment [67].

11.2 TRACK FITTING WITH MULTIPLE SCATTERING

Even with the novel thin pixel sensors discussed above, particle tracking for the Mu3e experiment is challenging. The low momentum electrons have strongly curved trajectories that are still dominated by multiple scattering. The Mu3e geometry allows for large propagation paths and can detect tracks that curl back in the magnetic field. At first, the track fitting seems similar to typical trajectory reconstruction at collider experiments. However, the dominating multiple scattering and large curvatures are usually not a priority for existing tools and algorithms that were developed mainly for tracking at high energies.

For successful tracking, a correct track model, i.e. the deterministic propagation and the corresponding uncertainty description, is vital. It is therefore necessary to evaluate which track model is optimal for a given detector configuration. Here, I investigated the performance of a novel type of track fit based on hit triplets with a focus on the Mu3e detector geometry. The algorithm breaks the particle trajectory into overlapping sets of hit triplets. It then fits each triplet assuming negligible position uncertainty and dominating multiple scattering by minimizing the scattering angle at the inner hit. In the end, triplets are combined into a global trajectory by a simple averaging of the fitted momentum.

This simple construction shows excellent performance for multiple scattering dominated tracking and is especially suitable for high curvature tracks. This includes both high precision and a correct description of the resulting parameter uncertainties. The new track fit also scales surprisingly well into a regime where hit uncertainties are dominating. In contrast, a single helix fit designed for low curvature tracks with dominating hit uncertainties does not perform as well when scaled down to the multiple scattering regime. The results show that the novel

triplets fit algorithm allows fast fits for the Mu3e experiment. Its superior tracking performance in the relevant regime makes it the method of choice for online reconstruction for the Mu3e experiment. Since the triplets are independent, the triplet fits can be performed in parallel. This can be used e. g. to perform initial track finding, by separately fitting multiple possible triplets and combining them at a later stage.

For offline, high precision reconstruction of particle trajectories, the advanced general broken lines fit can be used. I tested the viability of the algorithm and explored its application for Mu3e. The general broken lines fit allows improvement of the momentum resolution by up to 20%, especially for the high momentum tracks. Every increase in resolution translates into a higher background suppression and consequently to a higher sensitivity for the signal decay.

However, the long propagation paths of the recurling tracks in the Mu3e experiment are challenging for all algorithms, especially concerning the uncertainty of the reconstructed momenta. So far, tracks with long propagation paths and high curvature were not in the focus of algorithm development. This interesting finding will require further investigation.

Until now, the simulations intentionally assumed only Gaussian noise to describe multiple scattering. This is a reasonable assumption for the core scattering distribution and consistent with multiple scattering theory. As well, energy loss at the detector layers was not considered. This simplified simulation allowed the direct comparison of the different tracking algorithms. In the next step, a complete simulation of the Mu3e detector should be used.

I implemented both the different fit algorithms and the necessary tools in a comprehensive software package. It enables both additional tracking studies for the Mu3e experiment and for other applications of novel track fits e. g. in a collider setting.

One of the essential tasks for the successful reconstruction of tracks with a pixel detector is the correct alignment of the different sensors. For the Mu3e experiment, a track-based alignment strategy is foreseen. The general broken lines fit was initially designed as a track model for detector alignment and is also the candidate algorithm for Mu3e. Investigations to employ the general broken lines for track-based detector alignment in the

Mu3e experiment using the software developed in this thesis are currently underway.

11.3 CONCLUSION

The work presented in this thesis showed that the Mu3e tracking concept is feasible and that both the hardware and software prerequisites can be met.

The first working high voltage monolithic active pixel sensor prototype was subjected to test beam measurements. A detailed examination of its response to particles provides confidence that, despite the novelty of the sensor design, HV-MAPS can provide the necessary performance for high rate, high precision particle tracking. This marks the transition of HV-MAPS from a pixel sensor concept to a working technology and should also trigger interest for other possible applications. Mu3e will be the first physics experiment to use high voltage monolithic active pixel sensors.

To complement the new hardware compatible with multiple scattering dominated tracks, a novel, fast track fitting algorithm based on hit triplets was tested. The results showed that the triplets fit is suitable for online tracking for the Mu3e experiment. Offline refinement of track parameters for high precision measurements can be performed with the general broken lines fit as demonstrated in this work.

The research proposal for the Mu3e experiment was accepted in 2013 and a progress report for the initial phase I of the experiment is scheduled for submission to the research council of the Paul Scherrer Institute in February 2016. A first full-scale sensor prototype is expected to be produced in 2016. The availability of a first assembly of the central detector should coincide with the availability of the solenoid magnet. While the basic technology has been proven to work, there are still some challenges ahead. High rate read-out of the full detector and the subsequent processing with an online filter farm, as well as the detector alignment and calibration will be of importance.

Part III

APPENDIX

A

ANALYTIC TRACK PROPAGATION

The propagation of particle tracks in a magnetic field is one of the core components required for track reconstruction. Depending on the magnetic field configuration this may involve computationally expensive calculations, but for simple configurations fast analytic expressions can be derived.

In the following chapter, the basic equations for particle trajectories in a homogeneous magnetic field will be reviewed. The propagation of track parameters along the trajectories and to specific points of interest will be discussed.

A.1 EQUATIONS OF MOTION

A charged particle moving in a magnetic field is subject to the Lorentz force. In the absence of additional forces its equations of motion can be written as follows.¹

$$\mathbf{F} = q(\mathbf{v} \times \mathbf{B}) = \frac{d\mathbf{p}}{dt} \quad (\text{A.1})$$

The Lorentz force is perpendicular to the velocity and as a result the absolute momentum $p = \|\mathbf{p}\|$ with $\mathbf{p} = \gamma m \mathbf{v}$, m being the mass of the particle and γ being the relativistic Lorentz factor, is a conserved quantity.

Using the relation $ds/dt = v$ between path length, time, and velocity and the conservation of absolute momentum and absolute velocity, the equations of motion can be rewritten in terms of the integrated path length s along the particle curve.

$$\frac{d\mathbf{x}}{ds} = \hat{\mathbf{T}} \quad (\text{A.2})$$

$$\frac{d\hat{\mathbf{T}}}{ds} = \hat{\mathbf{T}} \times \frac{q}{pc} \mathbf{B}(\mathbf{x}) \quad (\text{A.3})$$

Here, the resulting six coupled differential equations are written as two sets of equations, one set for the position \mathbf{x} and one set for the normalized tangent vector $\hat{\mathbf{T}}$.

Solving these equations for arbitrary field configurations is usually performed using numerical integration techniques. The

¹ All equations are given in SI units.

various Runge-Kutta methods [1, 2] have been applied extensively in the high energy physics community for track propagation in inhomogeneous magnetic fields, e.g. in Bugge and Myrheim [16] or Lund et al. [47]. However, they are computationally expensive. For simple field configurations, fast analytical solutions can be found that are discussed in the following sections.

A.2 HELIX TRAJECTORY

A common magnet configuration in a particle physics experiment is a solenoid where the central inner field is reasonably well described by a homogeneous field, i.e. a magnetic field with constant direction and magnitude. For low-mass detectors, such as the Mu3e silicon tracker, energy losses of the particle along its path can be neglected and the particle momentum can be assumed to be a conserved quantity over the whole trajectory.

Without loss of generality the magnetic field can be set to $\mathbf{B} = B_z \hat{\mathbf{Z}}$, where $\hat{\mathbf{Z}}$ is the unit vector along the z-axis of the global right-handed Cartesian coordinate system. The equations of motion in Equation A.2 are then simplified to

$$\frac{d\mathbf{x}}{ds} = \hat{\mathbf{T}} \quad (\text{A.4})$$

$$\frac{d\hat{\mathbf{T}}}{ds} = K \hat{\mathbf{Z}} \times \hat{\mathbf{T}} \quad (\text{A.5})$$

with the global curvature parameter $K = -\frac{q}{pc} B_z$. The resulting particle trajectory is a helix, i.e. a circular motion in the plane transverse to the field direction and a linear drift along the field direction.

Instead of solving the equations explicitly for each coordinate the approach outlined in Strandlie and Wittek [38] will be followed and the solution $\mathbf{x}(s)$ and $\hat{\mathbf{T}}(s)$ will be defined in terms of a set of unit vectors with the initial position $\mathbf{x}(0) = \mathbf{x}_0$ and the initial tangent vector $\mathbf{T}(0) = \hat{\mathbf{T}}_0$ as the initial condition. The initial tangent is equivalent to the normalized initial particle momentum $\hat{\mathbf{T}}_0 = \mathbf{p}_0 / \|\mathbf{p}\|_0$.

The choice of unit vectors is strongly related to the choice of track parameters, e.g. the projections of the initial position onto the unit vectors are often used to define the spatial track parameters. Further calculations can be simplified if the chosen

set forms a basis, i.e. their pair-wise scalar product vanishes and their pair-wise vector product produces the third vector.

A.2.1 Magnetic System

The two known unit vectors of the equations of motion (A.4) are the magnetic field direction $\hat{\mathbf{Z}}$ and the initial tangent vector of the particle $\hat{\mathbf{T}}_0 = \mathbf{p}_0 / \|\mathbf{p}\|_0$. They are generally not orthogonal. An orthonormal basis that naturally describes the motion in the magnetic field can be constructed using these unit vectors by defining the two orthonormal unit vectors $\hat{\mathbf{U}}$ and $\hat{\mathbf{F}}_0$ as follows.

$$\hat{\mathbf{U}}_0 = \hat{\mathbf{Z}} \times \hat{\mathbf{T}}_0 / \|\hat{\mathbf{Z}} \times \hat{\mathbf{T}}_0\| \quad (\text{A.6})$$

$$\hat{\mathbf{F}}_0 = \hat{\mathbf{U}}_0 \times \hat{\mathbf{Z}} \quad (\text{A.7})$$

By construction, these two vectors together with the magnetic field direction $\hat{\mathbf{Z}}$ form the orthonormal basis set $\{\hat{\mathbf{F}}_0, \hat{\mathbf{U}}_0, \hat{\mathbf{Z}}\}$, i.e. they satisfy the following relations.

$$\hat{\mathbf{F}}_0 \times \hat{\mathbf{U}}_0 = \hat{\mathbf{Z}} \quad (\text{A.8})$$

$$\hat{\mathbf{U}}_0 \times \hat{\mathbf{Z}} = \hat{\mathbf{F}}_0 \quad (\text{A.9})$$

$$\hat{\mathbf{Z}} \times \hat{\mathbf{F}}_0 = \hat{\mathbf{U}}_0 \quad (\text{A.10})$$

The first two vectors $\hat{\mathbf{F}}_0$ and $\hat{\mathbf{U}}_0$ span the plane transverse to the field, i.e. the global x-y plane, and depend on the initial particle direction, as indicate by the subscript. $\hat{\mathbf{F}}_0$ is proportional to the projection of the initial tangent vector onto the transverse plane and allows the decomposition of the initial tangent into the transverse and longitudinal components.

$$\hat{\mathbf{T}}_0 = \cos \lambda \hat{\mathbf{F}}_0 + \sin \lambda \hat{\mathbf{Z}} \quad (\text{A.11})$$

The angle λ is the so-called dip angle that describes the relative strength of the transverse and longitudinal motion.

With the initial values \mathbf{x}_0 and $\hat{\mathbf{T}}_0$ for position and tangent and the unit vectors defined above, the expression for the helix trajectory is

$$K(\mathbf{x} - \mathbf{x}_0) = a\hat{\mathbf{F}}_0 \sin \tau + a\hat{\mathbf{U}}_0(1 - \cos \tau) + b\hat{\mathbf{Z}} \tau \quad (\text{A.12})$$

$$\hat{\mathbf{T}} = a\hat{\mathbf{F}}_0 \cos \tau + a\hat{\mathbf{U}}_0 \sin \tau + b\hat{\mathbf{Z}} \quad (\text{A.13})$$

where the previously defined curvature paramter K and the two scaling parameters $a = \cos \lambda$ and $b = \sin \lambda$ were used. Here, position and tangent are parametrized by the propagation angle $\tau = K \cdot s$ along the transverse circle.

A.2.2 Track System

Strandlie and Wittek [38] use a different, non-orthonormal set of unit vectors, namely the tangent vector $\hat{\mathbf{T}}_0$, the normalized magnetic field $\hat{\mathbf{H}} = \mathbf{B}/B_0$, and one additional unit vector $\hat{\mathbf{N}}_0 = \hat{\mathbf{H}} \times \hat{\mathbf{T}}_0 / \|\hat{\mathbf{H}} \times \hat{\mathbf{T}}_0\|$, to define the helix trajectory for an arbitrary field direction as follows.

$$Q(\mathbf{x} - \mathbf{x}_0) = \hat{\mathbf{T}}_0 \sin \theta + \alpha \hat{\mathbf{N}}_0 (1 - \cos \theta) + \gamma \hat{\mathbf{H}} (\theta - \sin \theta) \quad (\text{A.14})$$

$$\hat{\mathbf{T}} = \hat{\mathbf{T}}_0 \cos \theta + \alpha \hat{\mathbf{N}}_0 \sin \theta + \gamma \hat{\mathbf{H}} (1 - \cos \theta) \quad (\text{A.15})$$

Here, the curvature parameter is $Q = -\|\mathbf{B}\| \frac{q}{pc}$, the two scaling parameters $\alpha = \|\hat{\mathbf{H}} \times \hat{\mathbf{T}}_0\|$ and $\gamma = \hat{\mathbf{H}} \cdot \hat{\mathbf{T}}_0$ describe the relation between the transverse and the longitudinal motion¹, and a similar propagation angle $\theta = Q \cdot s$ marks the position along the transverse circle.

¹ Here: transverse to the field direction, not necessarily the z-axis

With this choice of unit vectors it is easier to identify the approximate behaviour of the trajectory and it is used in [38] to compute the transport Jacobian matrix along the trajectory. However, the fact that the vectors are not orthonormal results in more complicated propagation equations.

Converting between the two parametrizations can be easily accomplished by setting the magnetic field to $\mathbf{B} = B_z \hat{\mathbf{Z}}$. The initial track direction \mathbf{T}_0 is unchanged but the other two unit vectors can be replaced by $\hat{\mathbf{H}} = \text{sgn}(B_z) \hat{\mathbf{Z}}$ and $\hat{\mathbf{N}}_0 = \text{sgn}(B_z) \hat{\mathbf{U}}_0$ respectively. All other quantities can be redefined in terms of the new unit vectors and usually acquire an additional factor $\text{sgn}(B_z)$, i. e. $\alpha = a$, $\gamma = \text{sgn}(B_z)b$, the curvature $K = -B_z q/p = \text{sgn}(B_z)Q$, and the propagation angle $\tau = Ks = \text{sgn}(B_z)\theta$.

A.2.3 Useful Identities

With the helix solution (A.12) in the magnetic system some useful identities can be easily derived that are applied in the subsequent calculations.

The unit vectors, e. g. $\hat{\mathbf{F}}_0$ and $\hat{\mathbf{U}}_0$ for the magnetic coordinate system, are defined with respect to the initial tangent vector. The tangent vector changes along the trajectory and equivalent coordinate systems can be defined at every point along the tra-

jectory by calculating the unit vectors with respect to the propagated tangent.

$$\hat{\mathbf{U}} = \hat{\mathbf{Z}} \times \hat{\mathbf{T}} / \|\hat{\mathbf{Z}} \times \hat{\mathbf{T}}\| = \hat{\mathbf{U}}_0 \cos \tau - \hat{\mathbf{F}}_0 \sin \tau \quad (\text{A.16})$$

$$\hat{\mathbf{V}} = \hat{\mathbf{T}} \times \hat{\mathbf{U}} = -b\hat{\mathbf{F}}_0 \cos \tau - b\hat{\mathbf{U}}_0 \sin \tau + a\hat{\mathbf{Z}} \quad (\text{A.17})$$

$$\hat{\mathbf{F}} = \hat{\mathbf{U}} \times \hat{\mathbf{Z}} = \hat{\mathbf{F}}_0 \cos \tau + \hat{\mathbf{U}}_0 \sin \tau \quad (\text{A.18})$$

$$\hat{\mathbf{Z}} \times \hat{\mathbf{V}} = b\hat{\mathbf{F}}_0 \sin \tau - b\hat{\mathbf{U}}_0 \cos \tau \quad (\text{A.19})$$

The projection of the relative change in position along the propagated tangent is given by:

$$K(\mathbf{x} - \mathbf{x}_0) \cdot \hat{\mathbf{T}} = a^2 \sin \tau + b^2 \tau. \quad (\text{A.20})$$

A.3 PROPAGATION

What is usually needed are the track parameters at specific points of interest, e.g. at the point of closest approach to a reference position or at the intersection between the trajectory and a detector surface. The previous sections described the computation of track parameters at arbitrary positions along the particle trajectory. Since the track parameters are fully defined by their path length, propagating the track parameters to a specific point of interest is equivalent to calculating the corresponding path length.

An appropriate distance measure $d_s = d[\mathbf{x}(s)]$ can be defined for any point of interest, e.g. the distance to a possible vertex position, as a function of the track position. The path length of the point of interest is the one that minimizes the measure.

$$s_i = \arg \min_s d(s) \quad (\text{A.21})$$

Using the analytic trajectory expression Equation A.12 it can be directly calculated as the solution to the corresponding normal equations.

$$\left. \frac{\partial d}{\partial s} \right|_{s_i} = 0 \quad (\text{A.22})$$

For the intersection with a surface the intersection condition usually takes the form $d_s = 0$. Assuming a strictly positive distance measure this condition is equivalent to the minimization condition defined above.

It should be noted that it is usually easier to use a quadratic distance measure such as the squared norm of a distance vector instead of the norm itself, since the initial condition and the resulting normal equations do not involve square root terms.

A.3.1 Point of closest approach

For a given reference point \mathbf{r} , the squared distance

$$d^2(s) = (\mathbf{x}(s) - \mathbf{r})^2 = (\mathbf{x}(s) - \mathbf{r})^\top (\mathbf{x}(s) - \mathbf{r})$$

between the track position and the reference point is used as the distance measure. The propagation normal equations multiplied by the curvature K are then given by

$$\left. \frac{K}{2} \frac{\partial d^2}{\partial s} \right|_{s_i} = K \mathbf{T}_i \cdot (\mathbf{x}_i - \mathbf{r}) \quad (\text{A.23})$$

$$= K (\mathbf{x}_i - \mathbf{x}_0) \cdot \mathbf{T}_i + K (\mathbf{x}_0 - \mathbf{r}) \cdot \mathbf{T}_i \quad (\text{A.24})$$

$$= 0 \quad (\text{A.25})$$

Using the analytic trajectory expressions (A.12) the normal equation above can be rewritten as a trigonometric equation of the form

$$f_s \sin(\tau) + f_c \cos(\tau) + f_l \tau + f_k = 0$$

with the following coefficients

$$f_s = a K (\mathbf{x}_0 - \mathbf{r}) \cdot \hat{\mathbf{U}}_0 + a^2 \quad (\text{A.26})$$

$$f_c = a K (\mathbf{x}_0 - \mathbf{r}) \cdot \hat{\mathbf{F}}_0 \quad (\text{A.27})$$

$$f_l = b^2 \quad (\text{A.28})$$

$$f_k = b K (\mathbf{x}_0 - \mathbf{r}) \cdot \hat{\mathbf{Z}} \quad (\text{A.29})$$

This equation has no analytical solution but a fast approximate solution can be found by expanding the trigonometric functions in τ to a fixed order and solving the resulting polynomial equation directly. Details can be found in Section A.4.

A.3.2 Point of closest transverse approach

For the closest approach in the transverse plane, only the motion in the transverse plane needs to be considered, i. e. the distance measure is

$$d^2(s) = \left(\mathbf{x}(s)_{xy} - \mathbf{r}_{xy} \right)^2$$

The resulting normal equations are formally identical to the closest approach in three dimensions. All projections onto the magnetic field direction vanish and the normal equations take the simpler form

$$f_s \sin \tau + f_c \cos \tau = 0 \quad (\text{A.30})$$

with identical definitions of the f_s and f_c coefficients. The solution is discussed in Section A.4.

A.3.3 Planar surface

A plane can be defined by its normalized unit vector $\hat{\mathbf{N}}$ and an arbitrary anchor point \mathbf{a} on the surface. Every point \mathbf{y} on the plane then satisfies the following plane equation.

$$(\mathbf{y} - \mathbf{a}) \cdot \hat{\mathbf{N}} = 0 \quad (\text{A.31})$$

The plane equation can be used directly to find the path length s_i of the intersection. To simplify, the calculations are multiplied with the curvature parameter K and the dynamic part and the static parts are separated involving only the initial position \mathbf{x}_0 and the anchor point.

$$K(\mathbf{x}_i - \mathbf{x}_0) \cdot \hat{\mathbf{N}} + K(\mathbf{x}_0 - \mathbf{a}) \cdot \hat{\mathbf{N}} = 0 \quad (\text{A.32})$$

By inserting the analytic trajectory expression from Equation A.12, the plane equation can be rewritten as a trigonometric equation of the form

$$f_s \sin(\tau) + f_c \cos(\tau) + f_l \tau + f_k = 0 \quad (\text{A.33})$$

with the following coefficients

$$f_s = a \hat{\mathbf{F}}_0 \cdot \hat{\mathbf{N}} \quad (\text{A.34})$$

$$f_c = a \hat{\mathbf{U}}_0 \cdot \hat{\mathbf{N}} \quad (\text{A.35})$$

$$f_l = b \hat{\mathbf{Z}} \cdot \hat{\mathbf{N}} \quad (\text{A.36})$$

$$f_k = K(\mathbf{x}_0 - \mathbf{a}) \cdot \hat{\mathbf{N}} \quad (\text{A.37})$$

For a plane parallel to the magnetic field direction, i. e. $\hat{\mathbf{Z}} \perp \hat{\mathbf{N}}$, or for a transverse track with $b = 0$ the linear term vanishes and only the reduced equation $f_s \sin(\tau) + f_c \cos(\tau) + f_k = 0$ needs to be solved. For a plane orthogonal to the field direction, i. e. $\hat{\mathbf{F}}_0 \perp \hat{\mathbf{N}}$ and $\hat{\mathbf{U}}_0 \perp \hat{\mathbf{N}}$, f_s and f_c vanish and the equation reduces to the linear equation $f_l \tau + f_k = 0$. A detailed discussion of the solution can be found in Section A.4.

A.3.4 Cylindrical surface

For simplicity only cylindrical surfaces that are aligned with the magnetic field directions will be considered. Due to the symmetry along the cylinder axis only the transverse motion needs to be considered. In the transverse plane the cylinder is a circle defined by its center $\mathbf{c} = [c_x, c_y]$ and its radius r_c . The squared distance to the cylinder surface is given by

$$d^2(s) = \left(\mathbf{x}(s)_{xy} - \mathbf{c} \right)^2 - r_c^2 \quad (\text{A.38})$$

where only the particle position in the global xy -plane, i. e. the transverse plane of the magnetic field, are taken into account. The intersection of the track with the cylinder is given by $d^2(s) = 0$. Using $\mathbf{y} = K \left(\mathbf{x}(s)_{xy} - \mathbf{x}_{0,xy} \right)$ and $\mathbf{d} = K \left(\mathbf{x}_{0,xy} - \mathbf{c} \right)$, the intersection condition can be rewritten as

$$K^2 d^2(s) = (\mathbf{y} - \mathbf{d})^2 - r_c^2 \quad (\text{A.39})$$

$$= \mathbf{y}^2 - 2\mathbf{y} \cdot \mathbf{d} + \mathbf{d}^2 - r_c^2 = 0 \quad (\text{A.40})$$

The different terms of the condition can be easily derived by inserting the analytic trajectory Equation A.12 into \mathbf{y} to yield the following expressions.

$$\mathbf{y}^2 = 2a^2(1 - \cos \tau) \quad (\text{A.41})$$

$$\mathbf{y} \cdot \mathbf{d} = a(\widehat{\mathbf{F}}_0 \cdot \mathbf{d}) \sin \tau - a(\widehat{\mathbf{U}}_0 \cdot \mathbf{d})(1 - \cos \tau) \quad (\text{A.42})$$

Inserting these expressions back into the intersection condition Equation A.39 allow it to be rewritten as a trigonometric equation of the form

$$f_s \sin \tau + f_c \cos \tau + f_k = 0 \quad (\text{A.43})$$

with the following coefficients.

$$f_s = -2a(\widehat{\mathbf{F}}_0 \cdot \mathbf{d}) \quad (\text{A.44})$$

$$f_c = -2a(\widehat{\mathbf{U}}_0 \cdot \mathbf{d}) - 2a^2 \quad (\text{A.45})$$

$$f_k = 2a(\widehat{\mathbf{U}}_0 \cdot \mathbf{d}) + 2a^2 + \mathbf{d}^2 - r_c^2 = d^2 - r_c^2 - f_c \quad (\text{A.46})$$

The solution to the trigonometric equation is discussed in Section A.4.

A.3.5 Line

A line can be defined by a normalized direction vector $\hat{\mathbf{N}}$ and one arbitrary reference position \mathbf{a} on the line. All positions on the line can then be calculated as follows.

$$\mathbf{l} = \mathbf{a} + t \cdot \hat{\mathbf{N}} \quad t \in \mathbb{R} \quad (\text{A.47})$$

For any given position \mathbf{y} the closest point on the line \mathbf{l}_y can be calculated by projecting the distance to the reference vector onto the normal vector to calculate t and use equation A.47 to calculate the closest point.

$$\mathbf{l}_y = \mathbf{a} + \left((\mathbf{y} - \mathbf{a}) \cdot \hat{\mathbf{N}} \right) \hat{\mathbf{N}} \quad (\text{A.48})$$

The distance to line is then given by the distance to the closest point.

$$d[\mathbf{y}] = \left\| (\mathbf{y} - \mathbf{a}) - \left((\mathbf{y} - \mathbf{a}) \cdot \hat{\mathbf{N}} \right) \hat{\mathbf{N}} \right\| \quad (\text{A.49})$$

To calculate the point of closest approach to the line on the helix the squared distance to the closest point $d_s^2 = d[\mathbf{x}(s)]^2$ is used as the distance measure. The resulting normal equations are given by

$$\begin{aligned} \frac{1}{2} \frac{dd_s^2}{ds} \Big|_{s_i} &= \left((\mathbf{x}_i - \mathbf{a}) - \left((\mathbf{x}_i - \mathbf{a}) \cdot \hat{\mathbf{N}} \right) \hat{\mathbf{N}} \right) \left(\hat{\mathbf{T}}_i - \left(\hat{\mathbf{T}}_i \cdot \hat{\mathbf{N}} \right) \hat{\mathbf{N}} \right) \\ &= (\mathbf{x}_i - \mathbf{a}) \cdot \hat{\mathbf{T}}_i - \left((\mathbf{x}_i - \mathbf{a}) \cdot \hat{\mathbf{N}} \right) \left(\hat{\mathbf{T}}_i \cdot \hat{\mathbf{N}} \right) \\ &= 0 \end{aligned} \quad (\text{A.50})$$

With shortcuts for the initial scaled distance $\mathbf{d} = K(\mathbf{x}_0 - \mathbf{a})$ and the scaled helix position $\mathbf{y}_i = K(\mathbf{x}_i - \mathbf{x}_0)$ relative to the initial position the normal equations can be rewritten as follows

$$\begin{aligned} \frac{K}{2} \frac{dd_s^2}{ds} \Big|_{s_i} &= (\mathbf{y}_i \cdot \hat{\mathbf{T}}_i) + (\mathbf{d} \cdot \hat{\mathbf{T}}_i) \\ &\quad - (\mathbf{y}_i \cdot \hat{\mathbf{N}}) (\hat{\mathbf{T}}_i \cdot \hat{\mathbf{N}}) - (\mathbf{d} \cdot \hat{\mathbf{N}}) (\hat{\mathbf{T}}_i \cdot \hat{\mathbf{N}}) \\ &= 0 \end{aligned} \quad (\text{A.51})$$

It should be noted that the reference point on the line can be chosen freely. As a result it can always be chosen such that the initial distance vector is orthogonal to the normal vector by using the closest point to the initial helix position on the line

as the reference point, i. e. $\mathbf{a}' = \mathbf{a} + \left((\mathbf{x}_0 - \mathbf{a}) \cdot \widehat{\mathbf{N}} \right) \widehat{\mathbf{N}}$. Using the updated initial scaled distance vector

$$\mathbf{d}' = K \left((\mathbf{x}_0 - \mathbf{a}) - \left((\mathbf{x}_0 - \mathbf{a}) \cdot \widehat{\mathbf{N}} \right) \widehat{\mathbf{N}} \right) \quad (\text{A.52})$$

the identity $\mathbf{d}' \cdot \widehat{\mathbf{N}} = 0$ can be applied to derive the final normal equation for the closest approach.

$$\mathbf{y}_i \cdot \widehat{\mathbf{T}}_i + \mathbf{d}' \cdot \widehat{\mathbf{T}}_i - (\mathbf{y}_i \cdot \widehat{\mathbf{N}})(\widehat{\mathbf{T}}_i \cdot \widehat{\mathbf{N}}) = 0 \quad (\text{A.53})$$

Inserting the helix trajectory equation A.12 yields the following explicit expressions for the different terms

$$\mathbf{y}_i \cdot \widehat{\mathbf{T}}_i = a^2 \sin \tau + b^2 \tau \quad (\text{A.54})$$

$$\mathbf{d}' \cdot \widehat{\mathbf{T}}_i = a d_F \cos \tau + a d_U \sin \tau + b d_Z \quad (\text{A.55})$$

$$\mathbf{y}_i \cdot \widehat{\mathbf{N}} = a n_F \sin \tau + a n_U (1 - \cos \tau) + b n_Z \tau \quad (\text{A.56})$$

$$\widehat{\mathbf{T}}_i \cdot \widehat{\mathbf{N}} = a n_F \cos \tau + a n_U \sin \tau + b n_Z \quad (\text{A.57})$$

where the following shortcuts for the projections of the line normal vector and the initial scale distance vector onto the unit vectors of the helix system have been used.

$$\begin{aligned} d_F &= \mathbf{d}' \cdot \widehat{\mathbf{F}}_0 \\ d_U &= \mathbf{d}' \cdot \widehat{\mathbf{U}}_0 \\ d_Z &= \mathbf{d}' \cdot \widehat{\mathbf{Z}} \\ n_F &= \widehat{\mathbf{N}} \cdot \widehat{\mathbf{F}}_0 \\ n_U &= \widehat{\mathbf{N}} \cdot \widehat{\mathbf{U}}_0 \\ n_Z &= \widehat{\mathbf{N}} \cdot \widehat{\mathbf{Z}} \end{aligned} \quad (\text{A.58})$$

The additional condition $n_C^2 + n_U^2 + n_Z^2 = 1$ holds for the projections of the line normal vector due to the normalization of $\widehat{\mathbf{N}}$ and the basis property of the helix unit vector.

To solve the normal equations A.53 the product $(\mathbf{y}_1 \cdot \widehat{\mathbf{N}})(\widehat{\mathbf{T}}_i \cdot \widehat{\mathbf{N}})$ needs to be computed. For the general case of an arbitrarily oriented line this results in a transcendental equation involving combinations of trigonometric functions that has no analytic solution. For the time being, only the special case of a line parallel to the z-axis will be considered, i. e. $\widehat{\mathbf{N}} = \widehat{\mathbf{Z}}$. The projections of the normal vector onto the helix unit vectors follow as $n_C = n_U = 0$ and $n_Z = 1$. This yields a simplified normal equation of the of the form

$$f_s \sin \tau + f_c \cos \tau + f_l \tau + f_k = 0 \quad (\text{A.59})$$

with the following parameters.

$$f_s = a d_U - a^2 \quad (\text{A.60})$$

$$f_c = a d_F \quad (\text{A.61})$$

$$f_l = 2 b^2 \quad (\text{A.62})$$

$$f_k = b d_z \quad (\text{A.63})$$

The solution of this equation is discussed in Section A.4.

A.4 SOLUTIONS OF THE PROPAGATION EQUATIONS

The solution to the different propagation equations defined above can often be rewritten as a trigonometric equation of the following form.

$$f_s \sin \tau + f_c \cos \tau + f_l \tau + f_k = 0 \quad (\text{A.64})$$

In general, this transcendental equation has no closed-form solution, but analytic solutions can be found for some special cases. For the general case, approximate solutions can be derived.

A.4.1 Transverse Case

For a vanishing linear coefficient $f_l = 0$ only the following reduced equation needs to be solved.

$$f_s \sin \tau + f_c \cos \tau + f_k = 0 \quad (\text{A.65})$$

This transcendental equation has a closed-form solution that is given by

$$\tau = \arcsin \left(-\frac{f_k}{c} \right) - \tau_0 \quad (\text{A.66})$$

with $c = \sqrt{f_s^2 + f_c^2}$ and $\tau_0 = \text{atan2}(f_c, f_s)$. Please note that due to the sin periodicity the arcsin function can take two different values in the $-\pi$ to π range. Therefore, two solutions, $\tau_1 = \tau$ and $\tau_2 = \pi - \tau$, exists. Which one of these is the correct solution depends on the specific propagation configuration.

A.4.2 *Forward Case*

For vanishing sin and cos coefficients, e. g. when propagating to a forward plane, Equation A.64 reduces to a linear equation with the following solution.

$$\tau = -\frac{f_k}{f_l} \quad (\text{A.67})$$

A.4.3 *General Case*

In the general case of non-zero coefficients components, this transcendental equation has no closed-form solution. However, the function is smooth and relatively well-behaved. An approximate solution can be easily derived by expanding the trigonometric function in τ up to a fixed order and solving the resulting polynomial directly.

Algebraic expressions for the roots of quadratic, cubic, and quartic polynomials exist and can be found in the mathematical literature. The trigonometric function in Equation A.64 is therefore expanded to the fourth order as follows

$$\sin \tau = \tau - \frac{1}{6} \tau^3 + \mathcal{O}(\tau^5) \quad (\text{A.68})$$

$$\cos \tau = 1 - \frac{1}{2} \tau^2 + \frac{1}{24} \tau^4 + \mathcal{O}(\tau^4) \quad (\text{A.69})$$

and substitute $\tau = Ks$ to convert the initial trigonometric equation as a function of the propagation angle τ into a fourth order polynomial of the path length s

$$f_0 + f_1 s + f_2 s^2 + f_3 s^3 + f_4 s^4 = 0 \quad (\text{A.70})$$

with coefficients

$$f_0 = f_k + f_c \quad (\text{A.71})$$

$$f_1 = (f_l + f_s) K \quad (\text{A.72})$$

$$f_2 = -\frac{1}{2} f_c K^2 \quad (\text{A.73})$$

$$f_3 = -\frac{1}{6} f_s K^3 \quad (\text{A.74})$$

$$f_4 = \frac{1}{24} f_c K^4 \quad (\text{A.75})$$

¹ This is usually the case for particle trackers but is not necessarily true for the long recurling tracks in the Mu3e experiment.

This expansion is valid for small values of $\tau = Ks = s/R$.¹ This is satisfied if the path length s is small compared to the three-dimensional radius R of the circle. For very short path lengths

s or very low curvature, i. e. high momenta $K \sim 1/R \sim 1/p$, the fourth order expansion might be unnecessary and a lower order polynomial could be sufficient.

The polynomial usually has multiple roots. Some correspond to the approximate roots of the initial trigonometric equations and some are the result of the approximation. Which one of the possible roots correspond to the physical solution depends again on the specific propagation configuration.

If the approximate solution is insufficient and additional accuracy is required, the solution has to be calculated numerically. Due to the simplicity of the original equation, Newton's method, discussed e. g. in [23], can be used to optimize one of the approximate solutions in an iterative algorithm.

A.4.4 Conversion from propagation angle to path length

So far, the initial equation A.64 and all its solutions have been given in terms of the propagation angle $\tau = Ks$. However, the physical solution should be written in terms of the path length.

The path length always increases along the the direction of the track, whereas the propagation angle τ either increases or decreases depending on the curvature sign. In addition, for a given solution of τ , additional solutions $\tau \pm 2\pi$ exists.¹ These are usually approximate solutions but they become exact for $f_l = 0$. This means that a small τ could correspond to a large path length $s = (\tau + 2\pi)/K$ and vice versa.

Therefore, the conversion from angle to path length needs to take into account the expected direction and the curvature sign. E. g. for a propagation along the track direction the τ solutions need to be shifted such that the calculated path length $s = \tau/K$ is positive.

¹ Or $\pm n \cdot 2\pi$ with $n \in \mathbb{N}$ for multiple helix turns.

THE WATSON TRACKING LIBRARY

Watson is a C++11 library that provides basic functionality required for track reconstruction in a particle physics experiment based on the Eigen linear algebra package [84]. It was designed for modern compilers with a focus on simplicity and tries to have minimal external dependencies. It was developed for the Mu3e experiment but is general enough to be suitable for other experiments.

B.1 MOTIVATION AND PRIOR ART

The Mu3e experiment has very specific requirements when it comes to particle tracking and track reconstruction. Only a single detector technology, thin silicon pixel sensors, is used in the tracker and the detector geometry is relatively simple compared to other existing detectors, e. g. CMS or ATLAS. The magnetic field is intentionally designed to be homogeneous over a very large part of the detector volume to allow the usage of fast analytic propagation and reconstruction algorithms, but the low momentum of the decay particles results in trajectories with large curvatures and highly non-linear behaviour.

The detector uses a tracker with only four detector layers.¹ The pixel sensor single hit resolution combined with their small thickness means that measured hits can be directly translated into three-dimensional space points. No additional calculations, e. g. combining stereo layers for silicon strip sensors, are needed.

Almost all other particle physics experiments have to solve similar problems and have usually at least one track reconstruction software package. However, their situation is usually not identical and as a result most existing tracking software tends to be specific for a given experiment. The ATLAS and CMS experiments at CERN both have well established reconstruction packages [42, 83] and the CMS collaboration has published their offline analysis software on GitHub [83] since 2013.

¹ A maximum of eight hits per particle track when taking into account recurlers.

The tracker geometry and the material description for both experiments is larger and more complicated than the Mu3e tracker. The tracking packages are also embedded in a much larger reconstruction framework that includes calorimetry, particle identification, and so on. Those features are not required for the Mu3e experiment. In addition, their main focus are usually high momentum tracks. Low momentum tracks with large curvature are only a corner case for their track reconstruction challenges.

Another option is the GenFit package, an experiment-independent track fitting toolkit [53, 74]. It was originally designed for the PANDA experiment at GSI/FAIR but is also used at the FOPI experiment and at the Belle-II experiment. It is a full track reconstruction framework that provides multiple track fitting algorithms. It supports complex detector geometries, different detector technologies and inhomogeneous magnetic fields.

The available packages tend to provide too much functionality. Having to support this usually requires compromises in other areas, e.g. speed or usability. As a new experiment we can start with a blank slate. No legacy systems exist that would need to be supported. We can therefore choose to develop our own reconstruction package that optimally fits our special needs.

B.2 FUNCTIONALITY

The following functionality is implemented in *watson*. This includes e.g. the helical track propagation discussed in Appendix A.

GEOMETRY Geometric surfaces, e.g. planes and cylinders, and related operations, i.e. conversion between local and global coordinates, distances to and closest points on the surface. Helical and polynomial space curves.

DETECTORS AND MATERIAL Handling of measurement uncertainties and required projections; effects from material interaction, e.g. multiple scattering.

TRACK PARAMETERS Different track state parametrizations, i.e. global parameters in the global Cartesian coordinate system, local parameters on a given plane or surface,

parameters at the closest approach to a given point. Conversion between the different parametrizations including uncertainty propagation.

TRACK PROPAGATION Linear and helical propagation of track parameters either freely in space or to given points of interest, e.g. to the intersection with a surface. The implementation uses the direct propagation calculations described in Appendix A.

TRACK FITTING Single helix fit, triplets fit, and general broken lines fit and required functionality. The latter fit exists in two version, once as a wrapper to the original implementation by Claus Kleinwort [87] and once as a custom implementation based on the Eigen library.

VERTEX FITTING Fast multiple scattering vertex fit.

ERROR PROPAGATION Propagation Jacobians along helical trajectories and between different reference surfaces and points of closest approach. Propagation between different systems, e.g. local track system and measurement system.

B.3 ADDITIONAL FEATURES

B.3.1 *ROOT Compatibility*

In contrast to most existing software packages in the high energy physics community, *watson* is not based on ROOT. All geometry and linear algebra calculations use the Eigen library instead. To be able to integrate *watson* into other high energy physics packages necessitates additional means to provide ROOT compatibility. A separate header-only library *eigen_root* is provided that enables easy integration with ROOT and other ROOT-based packages. It uses the plugin mechanism of the Eigen library to extend the Eigen vector and matrix types with additional functionality.

Fixed-size Eigen vectors and vector expressions with 2, 3, or 4 coordinates are extended with additional accessor methods that mimic the interfaces of the corresponding geometric ROOT `GenVector` and `CLHep` types. E.g. `.x()`, `.y()`, and `.phi()` can

be used to access the respective coordinates. Extended constructors and assignment operators allow the creation of fixed-size Eigen vectors from GenVector types. With these additions fixed-size Eigen vectors and geometric GenVector and CLHep types coordinate types can seamlessly interchanged.

Compatibility with the ROOT linear algebra types TMatrix / TVector and SMatrix / SVector is made available via additional conversion functions and overloaded assignment operators. ROOT types can be created from Eigen types by calling one of the `.toTMatrix()`, `.toTVector()`, `.toSMatrix()`, and `.SVector()` methods that are implemented by *eigen_root*. Constructing Eigen types from ROOT types can be achieved by directly assigning a ROOT type to an Eigen type or by calling on of the overloaded constructors.

With the additional *eigen_root* compatibility layer the *watson* library can take full advantage of the Eigen library while granting interoperability with other ROOT based packages.

B.3.2 *Python Wrapper*

A python wrapper exists that provides most of the functionality of the main C++ library. It is intended to allow fast prototyping and for testing purposes.

B.3.3 *Operating Systems*

Watson is not tied to specific versions of any operating system. It was initially developed on Linux based systems and should work with any recent Linux distribution, e.g. OpenSuse 13.1 or higher, Fedora 22 or higher. It was also tested to work on MacOS X 10.8 or higher.

TRACK FITTING SUPPORTING FIGURES

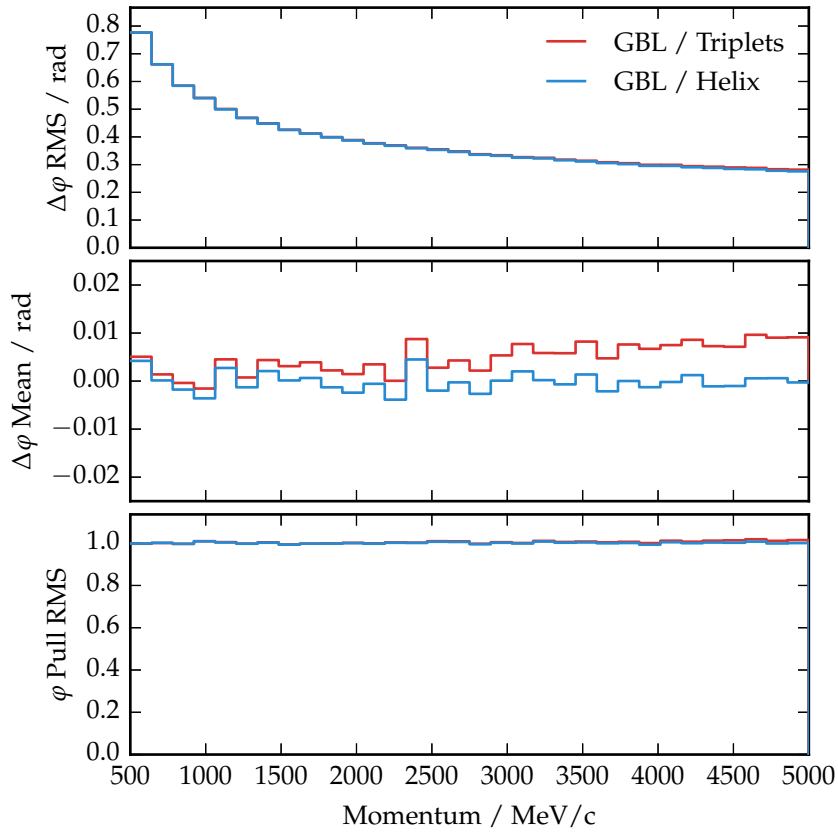


Figure C.1: Azimuth angle ϕ resolution, bias, and pull for the general broken lines fit using either the helix fit or the triplets fit with counter term and hit uncertainties as a reference trajectory. The ATLAS-like geometry described in Chapter 9 and tracks with a fixed dip angle of $\lambda = 20^\circ$ are used.

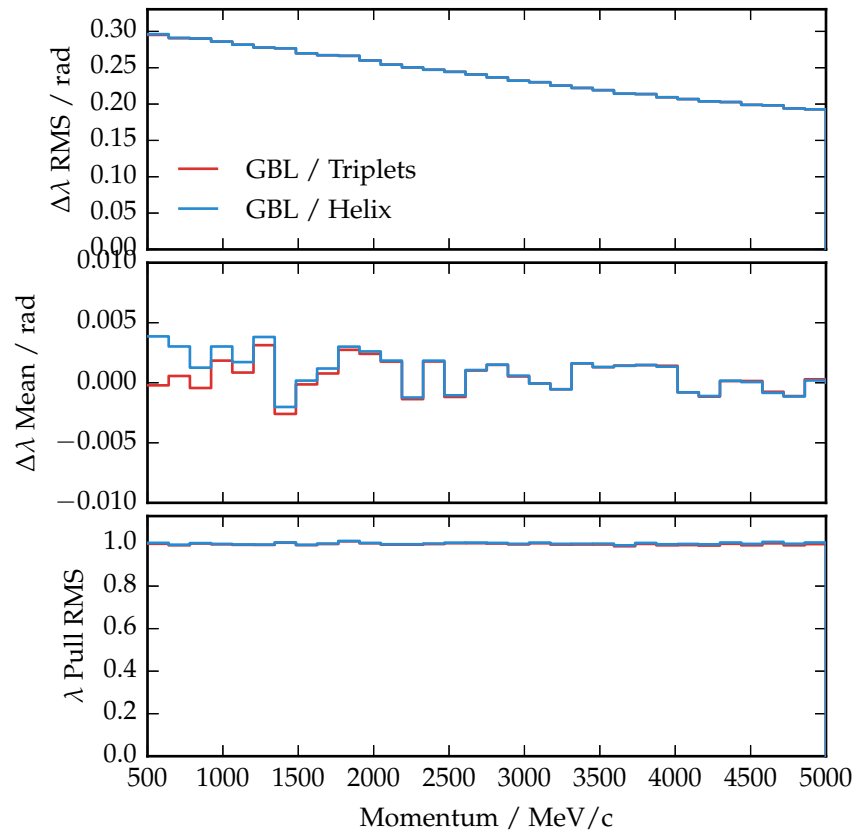


Figure C.2: Dip angle λ resolution, bias, and pull for the general broken lines fit using either the helix fit or the triplets fit with counter term and hit uncertainties as a reference trajectory. The ATLAS-like geometry described in Chapter 9 and tracks with a fixed dip angle of $\lambda = 20^\circ$ are used.

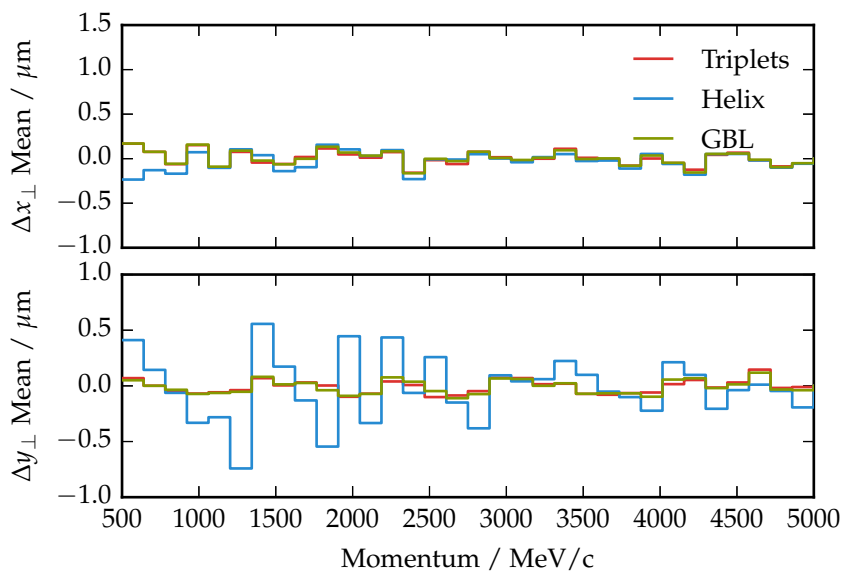


Figure C.3: Position fit bias at the inner-most hit for the ATLAS-like geometry described in Chapter 9 with different trackfits. Tracks with a fixed dip angle of $\lambda = 20^\circ$ are used.

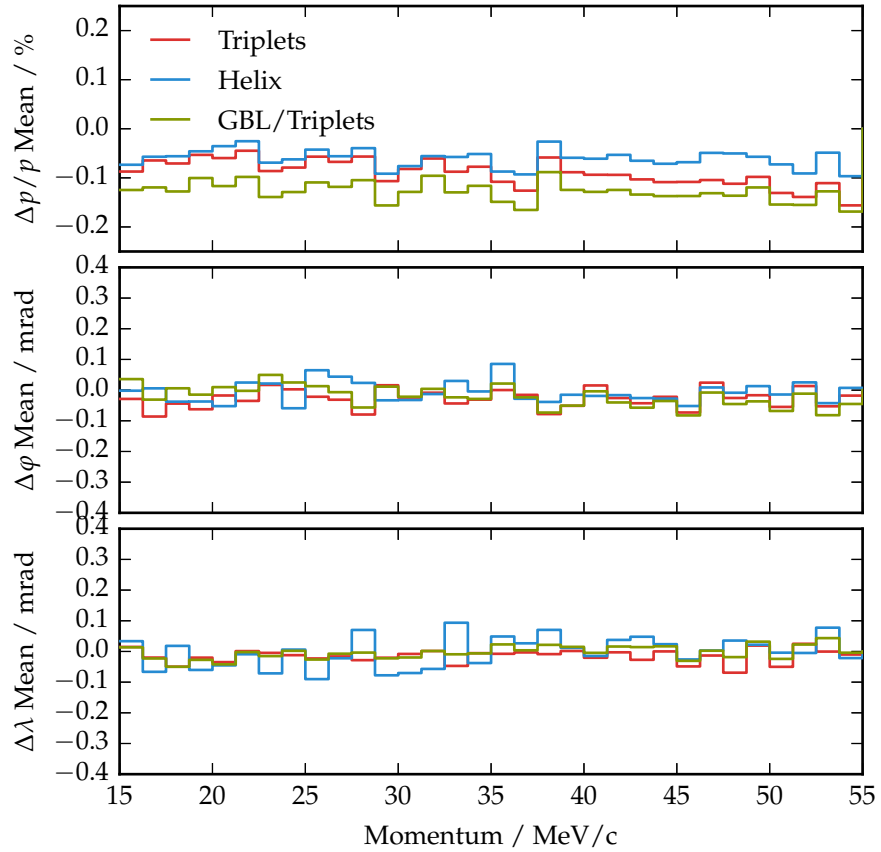


Figure C.4: Momentum parameters fit bias for the Mu3e geometry described in Chapter 10 with different trackfits. Short tracks with four hits and a fixed dip angle $\lambda = 20^\circ$ are used.

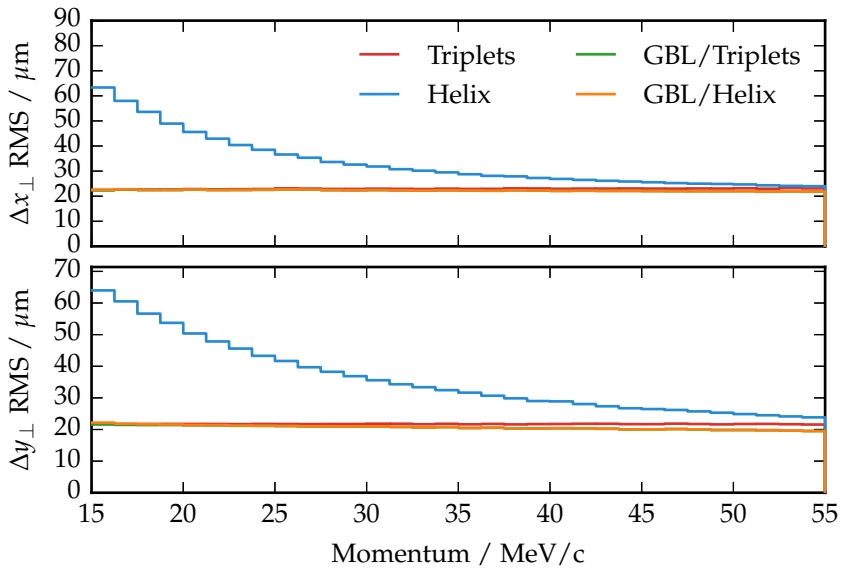


Figure C.5: Position resolution at the inner-most hit for the Mu3e geometry described in Chapter 10 with different trackfits. Short tracks with four hits and a fixed dip angle $\lambda = 20^\circ$ are used.

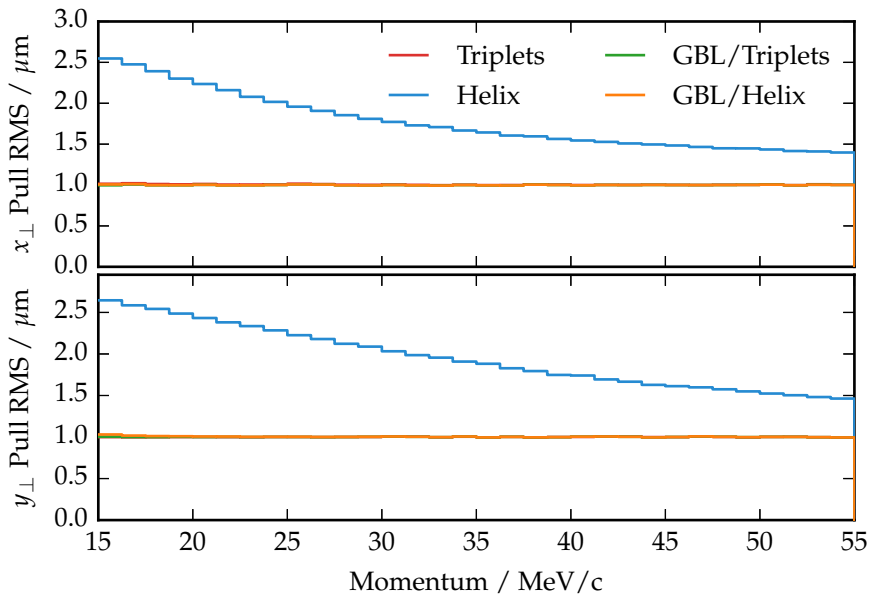


Figure C.6: Position pull distribution widths at the inner-most hit for the Mu3e geometry described in Chapter 10 with different trackfits. Short tracks with four hits and a fixed dip angle $\lambda = 20^\circ$ are used.

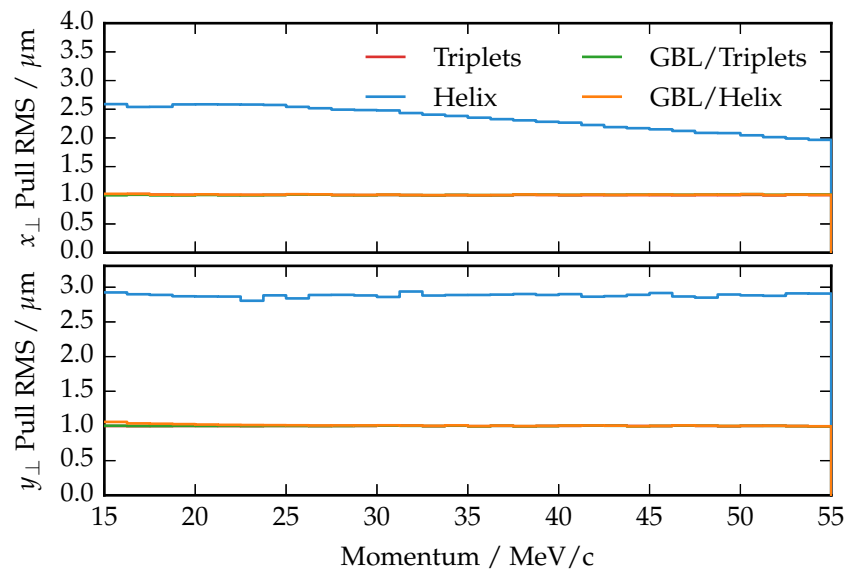


Figure C.7: Position pull distribution widths at the inner-most hit for the Mu3e geometry described in Chapter 10 with different track-fits. Long, recurling tracks with six hits and a fixed dip angle $\lambda = 20^\circ$ are used.

PUBLICATIONS

Some of the ideas, results, and figures in this theses have appeared previously or are expected to appear in the following publications and conference contributions.

- N. Berger et al. "A tracker for the Mu3e experiment based on high-voltage monolithic active pixel sensors". In: *Nuclear Instruments and Methods in Physics Research Section A: Accelerators, Spectrometers, Detectors and Associated Equipment*. Vienna Conference on Instrumentation 2013 732 (Dec. 21, 2013), pp. 61–65. DOI: 10.1016/j.nima.2013.05.035.
- N. Berger et al. "Multiple Coulomb Scattering in Thin Silicon". In: *Journal of Instrumentation* 9.07 (July 4, 2014), P07007. DOI: 10.1088/1748-0221/9/07/P07007. arXiv: 1405.2759.
- M. Kiehn. "The Mu3e Experiment - Introduction and Current Status". In: *Proceedings of Science*. 16th International Workshop on Neutrino Factories and Future Neutrino Beam Facilities. Glasgow, 2014.
- H. Augustin et al. "The MuPix high voltage monolithic active pixel sensor for the Mu3e experiment". In: *Journal of Instrumentation* 10.03 (Mar. 25, 2015), pp. C03044–C03044. DOI: 10.1088/1748-0221/10/03/C03044.
- N. Berger et al. "A New Three-Dimensional Track Fit with Multiple Scattering". In preparation. 2016.

REFERENCES

- [1] C. D. T. Runge. "Über die numerische Auflösung von Differentialgleichungen". In: *Mathematische Annalen* 46.2 (June 1895), pp. 167–178. DOI: 10.1007/BF01446807 (cit. on pp. 60, 128).
- [2] M. W. Kutta. "Beitrag zur näherungsweise Integration totaler Differentialgleichungen". In: *Zeitschrift für Mathematik und Physik* 46 (1901), pp. 435–453 (cit. on pp. 60, 128).
- [3] E. Noether. "Invariante Variationsprobleme". In: *Nachr. D. König. Gesellsch. D. Wiss. Zu Göttingen Math-phys. Klasse*.1918 (1918), pp. 235–257 (cit. on p. 5).
- [4] G. Wentzel. "Zur Theorie der Streuung von β -Strahlen". In: *Annalen der Physik* 374.21 (Jan. 1, 1922), pp. 335–368. DOI: 10.1002/andp.19223742103 (cit. on p. 65).
- [5] S. Goudsmit and J. L. Saunderson. "Multiple Scattering of Electrons". In: *Physical Review* 57.6 (Mar. 15, 1940), pp. 552–552. DOI: 10.1103/PhysRev.57.552.2 (cit. on p. 65).
- [6] S. Goudsmit and J. L. Saunderson. "Multiple Scattering of Electrons. II". In: *Physical Review* 58.1 (July 1, 1940), pp. 36–42. DOI: 10.1103/PhysRev.58.36 (cit. on p. 65).
- [7] G. Molière. "Theory of the scattering of fast charged particles. 2. Repeated and multiple scattering". In: *Z.Naturforsch.* A3 (1948), pp. 78–97 (cit. on p. 65).
- [8] H. A. Bethe. "Molière's Theory of Multiple Scattering". In: *Physical Review* 89.6 (Mar. 15, 1953), pp. 1256–1266. DOI: 10.1103/PhysRev.89.1256 (cit. on p. 65).
- [9] B. Pontecorvo. "Mesonium and anti-mesonium". In: *Sov. Phys. JETP* 6 (1957). [*Zh. Eksp. Teor. Fiz.*33,549(1957)], p. 429 (cit. on pp. 1, 6).
- [10] B. Pontecorvo. "Inverse beta processes and nonconservation of lepton charge". In: *Sov. Phys. JETP* 7 (1958). [*Zh. Eksp. Teor. Fiz.*34,247(1957)], pp. 172–173 (cit. on pp. 1, 6).

- [11] R. E. Kalman. “A New Approach to Linear Filtering and Prediction Problems”. In: *Journal of Basic Engineering* 82.1 (1960), p. 35. DOI: 10.1115/1.3662552 (cit. on p. 84).
- [12] Z. Maki, M. Nakagawa, and S. Sakata. “Remarks on the Unified Model of Elementary Particles”. In: *Progress of Theoretical Physics* 28.5 (Jan. 11, 1962), pp. 870–880. DOI: 10.1143/PTP.28.870 (cit. on pp. 1, 6).
- [13] N. Cabibbo. “Unitary Symmetry and Leptonic Decays”. In: *Physical Review Letters* 10.12 (June 15, 1963), pp. 531–533. DOI: 10.1103/PhysRevLett.10.531 (cit. on p. 1).
- [14] M. Kobayashi and T. Maskawa. “CP-Violation in the Renormalizable Theory of Weak Interaction”. In: *Progress of Theoretical Physics* 49 (Feb. 1, 1973), pp. 652–657. DOI: 10.1143/PTP.49.652 (cit. on p. 1).
- [15] V. L. Highland. “Some practical remarks on multiple scattering”. In: *Nuclear Instruments and Methods* 129.2 (Nov. 15, 1975), pp. 497–499. DOI: 10.1016/0029-554X(75)90743-0 (cit. on p. 66).
- [16] L. Bugge and J. Myrheim. “Tracking and track fitting”. In: *Nuclear Instruments and Methods* 179.2 (Jan. 15, 1981), pp. 365–381. DOI: 10.1016/0029-554X(81)90063-X (cit. on pp. 60, 128).
- [17] P. Billoir, R. Frühwirth, and M. Regler. “Track element merging strategy and vertex fitting in complex modular detectors”. In: *Nuclear Instruments and Methods in Physics Research Section A: Accelerators, Spectrometers, Detectors and Associated Equipment* 241.1 (Nov. 15, 1985), pp. 115–131. DOI: 10.1016/0168-9002(85)90523-6 (cit. on p. 84).
- [18] R. Frühwirth. “Application of Kalman filtering to track and vertex fitting”. In: *Nuclear Instruments and Methods in Physics Research Section A: Accelerators, Spectrometers, Detectors and Associated Equipment* 262.2–3 (Dec. 15, 1987), pp. 444–450. DOI: 10.1016/0168-9002(87)90887-4 (cit. on p. 84).
- [19] U. Bellgardt et al. “Search for the decay $\mu^+ \rightarrow e^+e^+e^-$ ”. In: *Nuclear Physics B* 299.1 (Mar. 28, 1988), pp. 1–6. DOI: 10.1016/0550-3213(88)90462-2 (cit. on pp. 2, 6, 9, 16).

- [20] M. Hansroul, H. Jeremie, and D. Savard. “Fast circle fit with the conformal mapping method”. In: *Nuclear Instruments and Methods in Physics Research Section A: Accelerators, Spectrometers, Detectors and Associated Equipment* 270.2 (July 15, 1988), pp. 498–501. DOI: 10.1016/0168-9002(88)90722-X (cit. on p. 73).
- [21] P. Billoir and S. Qian. “Simultaneous pattern recognition and track fitting by the Kalman filtering method”. In: *Nuclear Instruments and Methods in Physics Research Section A: Accelerators, Spectrometers, Detectors and Associated Equipment* 294.1–2 (Sept. 1, 1990), pp. 219–228. DOI: 10.1016/0168-9002(90)91835-Y (cit. on p. 84).
- [22] V. Karimäki. “Effective circle fitting for particle trajectories”. In: *Nuclear Instruments and Methods in Physics Research Section A: Accelerators, Spectrometers, Detectors and Associated Equipment* 305.1 (July 10, 1991), pp. 187–191. DOI: 10.1016/0168-9002(91)90533-V (cit. on p. 71).
- [23] W. H. Press, ed. *Numerical recipes in C: the art of scientific computing*. 2nd ed. Cambridge University Press, 1992 (cit. on pp. 73, 139).
- [24] Super-Kamiokande Collaboration, Y. Fukuda, et al. “Evidence for oscillation of atmospheric neutrinos”. In: *Physical Review Letters* 81.8 (Aug. 24, 1998), pp. 1562–1567. DOI: 10.1103/PhysRevLett.81.1562. arXiv: hep-ex/9807003 (cit. on pp. 1, 5).
- [25] N. Wermes and G. Hallewel. *ATLAS pixel detector: Technical Design Report*. Technical Design Report ATLAS. Geneva: CERN, 1998 (cit. on p. 27).
- [26] Y. Kuno and Y. Okada. “Muon Decay and Physics Beyond the Standard Model”. In: *Reviews of Modern Physics* 73.1 (Jan. 12, 2001), pp. 151–202. DOI: 10.1103/RevModPhys.73.151. arXiv: hep-ph/9909265 (cit. on p. 2).
- [27] SNO Collaboration. “Measurement of the rate of $\nu_e + d \rightarrow p + p + e^-$ interactions produced by 8B solar neutrinos at the Sudbury Neutrino Observatory”. In: *Physical Review Letters* 87.7 (July 25, 2001). DOI: 10.1103/PhysRevLett.87.071301. arXiv: nucl-ex/0106015 (cit. on pp. 1, 5).

- [28] V. Blobel and C. Kleinwort. “A New Method for the High-Precision Alignment of Track Detectors”. In: (Aug. 16, 2002). arXiv: hep-ex/0208021 (cit. on p. 41).
- [29] R. Frühwirth, A. Strandlie, and W. Waltenberger. “Helix fitting by an extended Riemann fit”. In: *Nuclear Instruments and Methods in Physics Research Section A: Accelerators, Spectrometers, Detectors and Associated Equipment* 490.1–2 (Sept. 1, 2002), pp. 366–378. DOI: 10.1016/S0168-9002(02)00911-7 (cit. on p. 73).
- [30] A. Strandlie, J. Wroldsen, and R. Frühwirth. “Treatment of multiple scattering with the generalized Riemann sphere track fit”. In: *Nuclear Instruments and Methods in Physics Research Section A: Accelerators, Spectrometers, Detectors and Associated Equipment* 488.1–2 (Aug. 1, 2002), pp. 332–341. DOI: 10.1016/S0168-9002(02)00465-5 (cit. on p. 73).
- [31] G. Cowan. *Statistical data analysis: [with applications from particle physics]*. Repr. Oxford science publications. Oxford: Clarendon Press, 2004. XIV, 197 S. (Cit. on pp. 69, 71).
- [32] W. Demtröder. *Elektrizität und Optik: mit 17 Tabellen, zahlreichen durchgerechneten Beispielen und 143 Übungsaufgaben mit ausführlichen Lösungen*. 3., überarb. u. erw. Aufl. Vol. 2. Experimentalphysik. Berlin ; Heidelberg [u.a.]: Springer, 2004. XIX, 482 S. (Cit. on p. 60).
- [33] N. Chernov and C. Lesort. “Least Squares Fitting of Circles”. In: *Journal of Mathematical Imaging and Vision* 23 (2005), pp. 239–252 (cit. on p. 73).
- [34] W. H. Bertl et al. “A Search for muon to electron conversion in muonic gold”. In: C47 (2006). collaboration = {SINDRUM II Collaboration}, pp. 337–346. DOI: 10.1140/epjc/s2006-02582-x (cit. on p. 6).
- [35] V. Blobel. “A new fast track-fit algorithm based on broken lines”. In: *Nuclear Instruments and Methods in Physics Research Section A: Accelerators, Spectrometers, Detectors and Associated Equipment*. TIME 2005 — Proceedings of the 1st Workshop on Tracking in High Multiplicity Environments 566.1 (Oct. 1, 2006), pp. 14–17. DOI: 10.1016/j.nima.2006.05.156 (cit. on pp. 41, 80, 83).

- [36] T. Haas. “A pixel telescope for detector R&D for an international linear collider”. In: *Nucl.Instrum.Meth.* A569 (2006), pp. 53–56. DOI: 10.1016/j.nima.2006.09.011 (cit. on p. 37).
- [37] T. Prokscha et al. “The new high-intensity surface muon beam $\mu E4$ for the generation of low-energy muons at PSI”. In: *Physica B: Condensed Matter*. Vol. 374–375. Proceedings of the Tenth International Conference on Muon Spin Rotation, Relaxation and Resonance. Mar. 31, 2006, pp. 460–463. DOI: 10.1016/j.physb.2005.11.132 (cit. on p. 15).
- [38] A. Strandlie and W. Wittek. “Derivation of Jacobians for the propagation of covariance matrices of track parameters in homogeneous magnetic fields”. In: *Nuclear Instruments and Methods in Physics Research Section A: Accelerators, Spectrometers, Detectors and Associated Equipment* 566.2 (Oct. 15, 2006), pp. 687–698. DOI: 10.1016/j.nima.2006.07.032 (cit. on pp. 62–64, 128, 130).
- [39] T. Behnke et al. *Test Beams at DESY*. EUNET-Memo-2007-11. July 17, 2007 (cit. on p. 36).
- [40] S. Hunklinger. *Festkörperphysik*. Oldenbourg Verlag, 2007. 614 pp. (cit. on pp. 25, 26).
- [41] I. Perić. “A novel monolithic pixelated particle detector implemented in high-voltage CMOS technology”. In: *Nuclear Instruments and Methods in Physics Research Section A: Accelerators, Spectrometers, Detectors and Associated Equipment*. Vol. 582. VERTEX 2006 Proceedings of the 15th International Workshop on Vertex Detectors. Dec. 1, 2007, pp. 876–885. DOI: 10.1016/j.nima.2007.07.115 (cit. on pp. 19, 28, 29).
- [42] A. Salzburger. *The ATLAS Track Extrapolation Package*. CERN Document Server. June 14, 2007. URL: <https://cds.cern.ch/record/1038100> (visited on 09/15/2015) (cit. on p. 141).
- [43] I.-M. Gregor. “EUNET-Pixel Telescope”. In: *Proceedings of Science*. VERTEX2008. 2008 (cit. on p. 37).
- [44] J. Baudot et al. “First test results of MIMOSA-26, a fast CMOS sensor with integrated zero suppression and digitized output”. In: *IEEE Nucl.Sci.Symp.Conf.Rec.*

- 2009 (2009), pp. 1169–1173. DOI: 10.1109/NSSMIC.2009.5402399 (cit. on p. 37).
- [45] A. de Gouvêa. “(Charged) Lepton Flavor Violation”. In: *Nuclear Physics B - Proceedings Supplements*. Proceedings of the Neutrino Oscillation Workshop 188 (Mar. 2009), pp. 303–308. DOI: 10.1016/j.nuclphysbps.2009.02.071 (cit. on pp. 7, 8).
- [46] R. M. Djilkibaev and R. V. Konoplich. “Rare Muon Decay $\mu^+ \rightarrow e^+e^-e^+\nu_e\bar{\nu}_\mu$ ”. In: *Phys.Rev.* D79 (2009), p. 073004. DOI: 10.1103/PhysRevD.79.073004 (cit. on p. 12).
- [47] Lund et al. “Track parameter propagation through the application of a new adaptive Runge-Kutta-Nyström method in the ATLAS experiment”. In: *Journal of Instrumentation* 4.04 (Apr. 1, 2009), P04001–P04001. DOI: 10.1088/1748-0221/4/04/P04001 (cit. on pp. 60, 128).
- [48] Lund et al. “Transport of covariance matrices in the inhomogeneous magnetic field of the ATLAS experiment by the application of a semi-analytical method”. In: *Journal of Instrumentation* 4.04 (Apr. 24, 2009), P04016–P04016. DOI: 10.1088/1748-0221/4/04/P04016 (cit. on p. 60).
- [49] P. Roloff. “The EUDET high resolution pixel telescope”. In: *Nucl.Instrum.Meth.* A604 (2009), pp. 265–268. DOI: 10.1016/j.nima.2009.01.069 (cit. on p. 37).
- [50] M. Valentan, M. Regler, and R. Frühwirth. “Generalization of the Gluckstern formulas II: Multiple scattering and non-zero dip angles”. In: *Nuclear Instruments and Methods in Physics Research Section A: Accelerators, Spectrometers, Detectors and Associated Equipment* 606.3 (July 21, 2009), pp. 728–742. DOI: 10.1016/j.nima.2009.05.024 (cit. on p. 66).
- [51] M. Capeans et al. *ATLAS Insertable B-Layer Technical Design Report*. CERN Document Server. Sept. 15, 2010. URL: <https://cds.cern.ch/record/1291633> (visited on 12/21/2015) (cit. on p. 87).
- [52] I.-M. Gregor. *EUDET Pixel Telescope Copies*. EUDET-Memo-2010-33. Dec. 18, 2010 (cit. on p. 37).

- [53] C. Höppner et al. “A novel generic framework for track fitting in complex detector systems”. In: *Nuclear Instruments and Methods in Physics Research Section A: Accelerators, Spectrometers, Detectors and Associated Equipment* 620.2–3 (Aug. 21, 2010), pp. 518–525. DOI: 10.1016/j.nima.2010.03.136 (cit. on p. 142).
- [54] I. Rubinskiy. *EUTelescope — Offline track reconstruction and DUT analysis software*. EUDET-Memo-2010-12. Dec. 1, 2010 (cit. on pp. 40, 41).
- [55] M. Seidel et al. “Production of a 1.3 MW proton beam at PSI”. In: *Proceedings of IPAC’10, Kyoto, Japan*. 2010 (cit. on p. 15).
- [56] V. Blobel, C. Kleinwort, and F. Meier. “Fast alignment of a complex tracking detector using advanced track models”. In: *Computer Physics Communications*. Computer Physics Communications Special Edition for Conference on Computational Physics Trondheim, Norway, June 23–26, 2010 182.9 (Sept. 2011), pp. 1760–1763. DOI: 10.1016/j.cpc.2011.03.017 (cit. on pp. 80, 83, 84).
- [57] I. Perić, C. Kreidl, and P. Fischer. “Particle pixel detectors in high-voltage CMOS technology—New achievements”. In: *Nuclear Instruments and Methods in Physics Research Section A: Accelerators, Spectrometers, Detectors and Associated Equipment*. International Workshop on Semiconductor Pixel Detectors for Particles and Imaging 2010 650.1 (Sept. 11, 2011), pp. 158–162. DOI: 10.1016/j.nima.2010.11.090 (cit. on pp. 19, 29).
- [58] H. Augustin. “Charakterisierung von HV-MAPS”. Bachelor Thesis. Heidelberg University, 2012 (cit. on pp. 34, 35, 55).
- [59] C. Kleinwort. “General broken lines as advanced track fitting method”. In: *Nuclear Instruments and Methods in Physics Research Section A: Accelerators, Spectrometers, Detectors and Associated Equipment* 673 (May 1, 2012), pp. 107–110. DOI: 10.1016/j.nima.2012.01.024 (cit. on pp. 41, 80, 84).
- [60] A.-K. Perrevoort. “Characterisation of High Voltage Monolithic Active Pixel Sensors for the Mu3e Experi-

- ment". Master Thesis. Heidelberg University, 2012 (cit. on pp. 32, 34, 35, 55).
- [61] A. Schöning et al. *Letter of Intent for an Experiment to Search for the Decay $\mu \rightarrow eee$* . Submitted to the PSI Research Council. Jan. 2012 (cit. on p. 2).
- [62] J. Adam et al. "New Constraint on the Existence of the $\mu^+ \rightarrow e^+ \gamma$ Decay". In: *Physical Review Letters* 110.20 (May 13, 2013), p. 201801. DOI: 10.1103/PhysRevLett.110.201801 (cit. on pp. 6, 15).
- [63] A. M. Baldini et al. "MEG Upgrade Proposal". In: (Jan. 30, 2013). arXiv: 1301.7225 (cit. on p. 8).
- [64] A. Blondel et al. *Research Proposal for an Experiment to Search for the Decay $\mu \rightarrow eee$* . Submitted to the PSI Research Council. Jan. 25, 2013. arXiv: 1301.6113 (cit. on pp. 2, 8, 9).
- [65] F. V. Böhmer et al. "Simulation of space-charge effects in an ungated GEM-based TPC". In: *Nuclear Instruments and Methods in Physics Research Section A: Accelerators, Spectrometers, Detectors and Associated Equipment* 719 (Aug. 11, 2013), pp. 101–108. DOI: 10.1016/j.nima.2013.04.020 (cit. on p. 19).
- [66] A. de Gouvêa and P. Vogel. "Lepton Flavor and Number Conservation, and Physics Beyond the Standard Model". In: *Progress in Particle and Nuclear Physics*. Fundamental Symmetries in the Era of the LHC 71 (July 2013), pp. 75–92. DOI: 10.1016/j.pnpnp.2013.03.006. arXiv: 1303.4097 (cit. on pp. 2, 6, 7).
- [67] I. Perić et al. "High-voltage pixel detectors in commercial CMOS technologies for ATLAS, CLIC and Mu3e experiments". In: *Nuclear Instruments and Methods in Physics Research Section A: Accelerators, Spectrometers, Detectors and Associated Equipment*. PIXEL 2012 731 (Dec. 11, 2013), pp. 131–136. DOI: 10.1016/j.nima.2013.05.006 (cit. on pp. 19, 28, 29, 48, 121).
- [68] H. Augustin. "Characterization of a Novel HV-MAPS Sensor with Two Amplification Stages and First Examination of Thinned MuPix Sensors". Master Thesis. Heidelberg University, 2014 (cit. on pp. 34, 35).

- [69] L. Bartoszek et al. *Muze Technical Design Report*. 2014 (cit. on p. 8).
- [70] N. Berger et al. "Multiple Coulomb Scattering in Thin Silicon". In: *Journal of Instrumentation* 9.07 (July 4, 2014), P07007. DOI: 10.1088/1748-0221/9/07/P07007. arXiv: 1405.2759 (cit. on p. 66).
- [71] Comet Collaboration. *Comet Phase-1 Technical Design Report*. J-PARC, 2014 (cit. on p. 8).
- [72] L. Huth. "Development of a Tracking Telescope for Low Momentum Particles and High Rates consisting of HV-MAPS". Master Thesis. Heidelberg University, 2014 (cit. on pp. 34, 55).
- [73] K. A. Olive et al. "Review of Particle Physics". In: *Chin.Phys.* C38 (2014), p. 090001. DOI: 10.1088/1674-1137/38/9/090001, \%.002010.1088/1674-1137/38/9/090001 (cit. on pp. 1, 11, 15, 17, 27, 65-67).
- [74] J. Rauch and T. Schlüter. "GENFIT - a Generic Track-Fitting Toolkit". In: (Oct. 14, 2014). arXiv: 1410.3698 (cit. on p. 142).
- [75] A. Schöning. "A broken helix trackfit with multiple scattering". Personal Note. 2014 (cit. on pp. 73, 74, 79, 91).
- [76] F. Berg et al. "Target Studies for Surface Muon Production". Nov. 4, 2015 (cit. on p. 15).
- [77] Daya Bay Collaboration et al. "New Measurement of Antineutrino Oscillation with the Full Detector Configuration at Daya Bay". In: *Physical Review Letters* 115.11 (Sept. 11, 2015), p. 111802. DOI: 10.1103/PhysRevLett.115.111802 (cit. on p. 5).
- [78] H. P. Eckert. "The Mu3e Tile Detector". PhD Thesis. Heidelberg University, May 2015 (cit. on p. 17).
- [79] I. Perić et al. "Overview of HVCMOS pixel sensors". In: *Journal of Instrumentation* 10.05 (2015), p. C05021. DOI: 10.1088/1748-0221/10/05/C05021 (cit. on p. 30).
- [80] N. Berger et al. "A New Three-Dimensional Track Fit with Multiple Scattering". In preparation. 2016 (cit. on pp. 73, 91).

- [81] Mu3e Collaboration. *The Phase I Mu3e Experiment*. Progress report to be submitted to the PSI Research Council. Feb. 2016 (cit. on pp. 9, 34).
- [82] R. Brun, F. Rademakers, et al. *ROOT — an object oriented data analysis framework*. URL: <http://root.cern.ch> (cit. on p. 51).
- [83] CMS Collaboration. *CMS Offline Software*. URL: <https://github.com/cms-sw> (cit. on p. 141).
- [84] *Eigen: a C++ linear algebra library*. URL: <http://eigen.tuxfamily.org> (cit. on p. 141).
- [85] *EUDAQ: a generic data acquisition framework*. URL: <https://eudaq.github.io/> (cit. on p. 37).
- [86] *EUTelescope: a generic pixel telescope data analysis framework*. URL: <http://eutelescope.web.cern.ch/> (cit. on p. 40).
- [87] C. Kleinwort. *General Broken Lines Library*. URL: <https://www.wiki.terascale.de/index.php/GeneralBrokenLines> (cit. on p. 143).
- [88] Linear Collider Collaboration. *ILC Soft — Common Software Packages for the International Linear Collider*. URL: <http://ilcsoft.desy.de> (cit. on p. 40).
- [89] *The 2015 Nobel Prize in Physics - Press Release*. URL: http://www.nobelprize.org/nobel_prizes/physics/laureates/2015/press.html (visited on 12/18/2015) (cit. on p. 1).

DANKSAGUNG

An dieser Stelle möchte ich mich für die Unterstützung bedanken, die ich bei der Durchführung dieser Doktorarbeit erhalten habe.

Bei meinem Doktorvater André Schöning, der mich erst auf das Mu3e Experiment aufmerksam gemacht hat und mich bei der Durchführung dieser Arbeit betreut hat.

Bei Stephanie Hansmann-Menzemer, für die Bereitschaft als Zweitgutachterin zur Verfügung zu stehen.

Bei Niklaus Berger, dem besonderer Dank gilt für den intensiven Austausch der entscheidend zum Erfolg dieser Arbeit beigetragen hat.

Bei den Mitgliedern und Ehemaligen der Mu3e Arbeitsgruppe, für die angenehme Arbeitsatmosphäre in Heidelberg und besonders auf den Teststrahl Kampagnen. Insbesondere bei Heiko Augustin, Lennart Huth und Ann-Kathrin Perrevoort, für die intensive Zusammenarbeit seit Beginn meiner Arbeit.

Bei den Korrekturlesern Heiko Augustin, Niklaus Berger, Kristin Grußmayer, Lennart Huth und Frank Meier.

Bei den Mitgliedern der Arbeitsgruppe Herten für die kurzweiligen Kaffeepausen.

Bei der ganzen Familie Grußmayer.

Bei meiner Familie für die andauernde Unterstützung.

Zuletzt möchte ich mich besonders bei Kristin Grußmayer bedanken. Ohne Ihre Unterstützung wäre diese Arbeit einfach nicht möglich gewesen.

COLOPHON

This document was typeset in \LaTeX using the KOMA-Script classes and the typographical look-and-feel `classicthesis` developed by André Miede. The body text is set in 12 pt with the Palatino typeface.